Integrating Drones and Wireless Power Transfer into Beyond 5G Networks

Xiaohui Zhou

August 2019

A thesis submitted for the degree of
Doctor of Philosophy

Australian National University

Research School of Electrical, Energy and Materials Engineering
College of Engineering and Computer Science
The Australian National University

Declaration

The contents of this thesis are the results of original research and have not been submitted for a higher degree to any other university or institution.

The work in this thesis has been published or has been submitted for publication as journal papers or conference proceedings.

The research work presented in this thesis has been performed jointly with Assoc. Prof. Salman Durrani (The Australian National University), Dr. Jing Guo (The Australian National University), Prof. Halim Yanikomeroglu (Carleton University, Canada) and Assoc. Prof. Marco Di Renzo (Université Paris-Saclay, France). The substantial majority of this work was my own.

Xiaohui Zhou
Research School of Electrical, Energy and Materials Engineering,
College of Engineering and Computer Science,
The Australian National University,
Canberra, ACT 2601,
AUSTRALIA

Acknowledgments

This work would not have been possible without the help of a number of people.

First and foremost, I would like to express my deepest gratitude to my primary supervisor, Assoc. Prof. Salman Durrani, for his continuous support and encouragement throughout my entire PhD study. He has always made himself available for discussion, provided me a lot of sound advice and insights on research problems and paper writing. I am also very grateful to Dr. Jing Guo for sharing her knowledge and providing numerous advices, particularly in the area of stochastic geometry, which inspired much of the work in this thesis. I would also like to thank Assoc. Prof. Xiangyun Zhou and Dr. Nan Yang for being on my supervisory panel and providing me invaluable suggestions to improve my academic skills. I would also like to acknowledge scholarship and grant supports from the Australian National University.

It has been my great pleasure to work in such a friendly and supportive environment. Special thanks to Dr. Shihao Yan, Dr. Wen Zhang, Dr. Prasanga Samarasinghe, Assoc. Prof. Parastoo Sadeghi, Prof. Rodney A. Kennedy and Prof. Thushara D. Abhayapala. I also would like to thank all my colleagues and friends at ANU, especially Dr. Mingchao Yu, Dr. Biao He, Dr. Wanchun Liu, Dr. Yirui Cong, Dr. Shama Islam, Dr. Yifei Huang, Dr. Noman Akbar, Dr. Jihui Zhang, Dr. Hanchi Chen, Dr. Alice Bates, Dr. Ni Ding, Dr. Zohair Abu Shaban, Simin Xu, Yiran Wang, Chunhui Li, Abbas Koohian, Sahar Idrees, Rabbia Saleem, Nilupuli Senadhira, Khurram Shahzad, Sheeraz Alvi, Xiaolun Jia, Usama Elahi, Nicole Sawyer and Yonggang Hu. You all wonderful people have made my research life delightful. I am also grateful to Yuting Fang. Thank you for making our office full of joy and encouragement.

I would like to express my heartfelt appreciation to my parents for their unconditional love and support. Thank my parents for providing me the opportunity to study in Australia since 2008. Without them, I would not be able to achieve what I have achieved now. Last, but certainly not least, I would like to thank my partner Kelvin for his understanding and encouragement which helped me achieve so much during the last few years.

Abstract

As fifth generation (5G) standards have been established and 5G commercial products are just around the corner, both academia and industry have started to look at requirements for beyond 5G networks. Network flexibility and long battery life are among the key requirements for beyond 5G wireless communication systems. These critical requirements, which have not been sufficiently addressed in the previous generations, are the focus of this thesis.

The first half of this thesis explores two important use cases of drones to provide flexible communication networks. First, the performance of a cellular network with underlay drone cell for temporary events inside a stadium is studied. Using stochastic geometry, a general analytical framework is proposed to analyze the uplink and the downlink coverage probabilities for both the aerial and the terrestrial systems. Our results show that for urban environment and dense urban environment, the drone is best deployed at a low height (e.g., 200 m or lower), regardless of the distance between the center of the stadium and the terrestrial base station. However, for suburban environment and high-rise urban environment, the best drone altitude varies. Second, the performance of emergency information dissemination in public safety scenarios using drone is studied. A drone-assisted multihop multicast device-to-device (D2D) network is considered, where an emergency alert message broadcasted by a drone at the first time slot is multicasted by the D2D users that have successfully received the message through multihop. The impact of different system parameters on the link and the network performance is investigated. Our results demonstrate that a higher drone altitude provides better link and network coverage probabilities and lower mean local delay. Under practical setups, the cell edge user located 2 km from the ground projection of the drone has a link coverage probability around 90% after 5 time slots and a mean local delay of 2.32 time slots with a drone height as low as 200 m.

The second half of this thesis investigates wireless power transfer networks. Specifically, the use of power beacons in a millimeter wave wireless ad hoc network is considered, where transmitters adopt the harvest-then-transmit protocol. First, the characteristic of the aggregate received power from power beacons is analyzed and the

lognormal distribution is found to provide the best complementary cumulative distribution function approximation compared to other distributions considered in the literature. Then, a tractable model with discrete transmit power for each transmitter is proposed to compute the channel coverage probability and the total coverage probability. Our results show that our model provides a good accuracy and reveal the impact of different system parameters on the total coverage probability. Our results also illustrate that under practical setups, for power beacon transmit power of 50 dBm and transmitters with maximum transmit power between $20 - 40$ dBm, which are safe for human exposure, the total coverage probability is around 90%. Thus, it is feasible and safe to power transmitters in a millimeter wave ad hoc network using power beacons.

List of Publications

The work in this thesis has been published or under preparation for publication as journal and conference papers. These papers are:

Journal papers:

J1. **X. Zhou**, J. Guo, S. Durrani, and M. D. Renzo, "Power Beacon-Assisted Millimeter Wave Ad Hoc Networks," *IEEE Trans. Commun.*, vol. 66, no. 2, pp. 830–844, Feb. 2018.

J2. **X. Zhou**, S. Durrani, J. Guo, and H. Yanikomeroglu, "Underlay Drone Cell for Temporary Events: Impact of Drone Height and Aerial Channel Environments," *IEEE Internet Things J.*, vol. 6, no. 2, pp. 1704–1718, Apr. 2019.

J3. **X. Zhou**, S. Durrani, and J. Guo, "Drone-initiated D2D-aided Multihop Multicast Networks for Emergency Information Dissemination," submitted to *IEEE Access*, under major revision.

Conference paper:

C1. **X. Zhou**, S. Durrani, and J. Guo, "Characterization of Aggregate Received Power from Power Beacons in Millimeter Wave Ad Hoc Networks," in *Proc. IEEE ICC*, May. 2017.

The following papers are also produced during my PhD study but not explicitly used in this thesis.

Journal paper:

J4. **X. Zhou**, J. Guo, S. Durrani, and I. Krikidis, "Performance of Maximum Ratio Transmission in Ad Hoc Networks with SWIPT," *IEEE Wireless Commun. Lett.*, vol. 4, no. 5, pp. 529–532, Oct. 2015.

Conference paper:

C2. **X. Zhou**, J. Guo, S. Durrani, and H. Yanikomeroglu, "Uplink Coverage Performance of an Underlay Drone Cell for Temporary Events," in *Proc. IEEE ICC Workshops*, May. 2018. (invited paper)

List of Abbreviations

ABS	Aerial base station
AsD	Aerial base station-supported device
AWGN	Additive white Gaussian noise
CCDF	Complementary cumulative distribution function
CDF	Cumulative distribution function
CSI	Channel state information
DUE	Drone user equipment
D2D	Device-to-device
IoT	Internet of Things
i.u.d	Independently and uniformly distributed
LOS	Line-of-sight
MGF	Moment generating function
MIMO	Multiple input multiple output
mmWave	Millimeter wave
NLOS	Non-line-of-sight
OUT	Outage
PB	Power beacon
PDF	Probability density function
PMF	Probability mass function
PPP	Poisson point process
RF	Radio-frequency
RX	Receiver
SINR	Signal-to-interference-plus-noise ratio
SNR	Signal-to-noise ratio
SWIPT	Simultaneous wireless information and power transfer
TBS	Terrestrial base station
TsUE	Terrestrial base station-supported user equipment
TX	Transmitter
WPT	Wireless power transfer

List of Notations

α	Path-loss exponent
γ	SINR or SNR threshold
γ_{PT}	Power circuit activation threshold
ζ	Power conversion efficiency
η	Additional attenuation factor for aerial link
λ	Node density
ρ	Uplink RX sensitivity
σ^2	Variance of AWGN
τ	Time switching parameter
ϕ	Set of nodes
h	Drone height
j	Imaginary number $\sqrt{-1}$
m	Nakagami-m fading parameter
P	Transmit or received power
$P^{\max}$	Maximum power
$\mathbb{P}_{\mathrm{cov}}$	Coverage probability
$\mathbb{P}_{\mathrm{out}}$	Outage probability
$\mathbb{P}_{\mathrm{s}}$	Success probability
p_{L}	LOS probability
p_{N}	NLOS probability
R	Radius of disk
$\mathcal{S}$	Network region
$\lvert\mathcal{S}\rvert$	Area of network region
$\Gamma(x)$	Complete Gamma function
$\gamma(x,y)$	Lower incomplete Gamma function
$\kappa_X(n)$	nth cumulant of a random variable X
$\mathbb{E}_X[\cdot]$	Expectation operator with respect to X
$F_X(\cdot)$	CDF of a random variable X
$f_X(\cdot)$	PDF of a random variable X

$\mathcal{L}_X(s)$	Laplace transform of the distribution of a random variable X
$\mathcal{M}_X(s)$	MGF of the distribution of a random variable X
$PL(\cdot)$	Path-loss function
$\Pr(\cdot)$	Probability measure
$\Pr(\cdot\|\cdot)$	Conditional probability measure
$\mathrm{Re}[\cdot]$	Real part of a complex number
$\mathrm{Im}[\cdot]$	Imaginary part of a complex number
$x_{(n)}$	Rising factorial
${}_2F_1(a,b;c;z)$	Gaussian hypergeometric function
$\|\cdot\|$	Euclidean norm
$\setminus$	Set exclusion operator

Contents

List of Figures

List of Tables

Chapter 1

Introduction

1.1 Motivation

The growth and adoption of wireless communications has proven to be hugely successful over the past four decades. It has been reported by Cisco that the number of mobile devices worldwide is 7.4 billion in 2014 and is predicted to increase to 11.5 billion in 2019 [3]. The first introduction of cellular communications took place in the 1980s, where the first generation (1G) of mobile terminals used analogue signals to connect to the network. Since then, a new generation of mobile communication system with higher capacities and better coverage has been introduced every decade. Evolving from 1G to the second generation Global System for Mobile Communications (GSM), the third generation Universal Mobile Telecommunication System (UTMS) and the fourth generation (4G) long-term evolution (LTE), the analog communication system has transitioned to digital one and the core services have moved from voice calling and short messaging service (SMS) to voice over Internet Protocol (VoIP) and data service [4].

The introduction of the next generation of wireless communication network, i.e., the fifth generation (5G) network is on its way with major commercial deployments expected to start in 2020 globally. The 5G communication system promises to handle markedly higher mobile data traffic with significantly faster bit rates and notably lower latency than current 4G network [4, 5]. To achieve these network requirements, the three building-block technologies forming the backbone of 5G communication system, named as the big 3 in [6], are densification (e.g., small cells and heterogeneous networks), massive multiple input multiple output (MIMO) and millimeter wave (mmWave). Besides the big 3, the development of 5G network also provides opportunities for many other emerging technologies, such as full duplex communication, cognitive radio network, device-to-device (D2D) communication, vehicle-to-

vehicle (V2V) communication, machine-to-machine (M2M) communication, an advanced range of Internet of Things (IoT) communications, software defined network, network function virtualization and network slicing [4, 5, 6].

It is important and timely to consider the research for the future of wireless communication network, a future that goes beyond 5G network. Beyond 5G, there are even more opportunities and even bigger challenges ahead. Beyond 5G networks will not only take 5G networks into faster speed with lower latency, but are also expected to be able to operate on diverse spectrum types and bands. A major transformation in the beyond 5G era is software-based design, which will address the requirements for high cost efficiency, high reliability and high security [7]. The continued growth in the number of dynamic connected network devices inevitably increases the need for massive connectivity and flexibility for beyond 5G communication systems. Flexible wireless communication networks are expected to be effortlessly designed, configured, managed and maintained to meet the various requirements of service quality and spectrum bandwidth for fundamentally new applications, e.g., industrial automation and smart cities, which will transform our everyday lives and business and change how people engage with the environment. Moreover, the demand for communication devices with long battery life grows gradually in beyond 5G networks [4].

The evolution and development of wireless communication networks stimulates the growth of many exciting new technologies and introduces innovating applications for existing technologies. This thesis focuses on drone communications and wireless power transfer (WPT) which are two emerging technologies for beyond 5G networks. Some key technical aspects, significant research challenges, critical open problems and detailed motivation for these two technologies are discussed in the following subsections.

1.1.1 Drone Communication Networks

Drones have been proposed as an enabling technology to fulfill the flexibility requirement in beyond 5G networks because of their high mobility. They can be easily and flexibly deployed and rapidly and dynamically reconfigured to provide on-demand wireless communication to terrestrial users. Drones avoid the need for highly constrained and expensive infrastructures as terrestrial base stations (TBSs) do. Due to the unique features of drones, a number of prospective use cases for the deployment of drones in wireless communication systems have been identified in [8, 9, 10]. These

include imminent scenarios, such as providing service to rural areas that are out of coverage of cellular networks, recovering the service for malfunctioning terrestrial infrastructures damaged or even destroyed by natural disasters and offloading cellular data traffic in cases of radio access network congestion and/or core network congestion. The use of drones is proposed in vehicular ad hoc networks (VANETs) to serve users with high mobility. Drones can also be deployed to provide additional resources for temporary blind spots and for temporary events (e.g., concerts and sports events inside stadiums). In the application for smart agriculture, drones can reduce energy consumption of wireless sensors for sending information by moving towards them. Furthermore, drones can be deployed to provide robust service between first responders and victims for search and rescue operations. In public safety situations (e.g., bushfire and flood), drones can support terrestrial networks for rapid information dissemination by broadcasting emergency messages to ground devices. Drones are also proposed as an effective caching solution, since they can dynamically cache the popular contents and track the mobility pattern of mobile users. In addition, city aerial delivery services can be realized using drone user equipments (DUEs) that are connected to cellular networks.

In most of the scenarios described above, drones operate under one or more of the communication models shown in Figure 1.1. Similar to the conventional terrestrial communications, these four models are [11]:

(a) Downlink, where the drone acts as an aerial base station (ABS) and sends independent information to multiple ground nodes;

(b) Uplink, where the drone acts as an ABS and collect independent information from multiple ground terminals;

(c) Relaying, where drone is deployed to provide wireless connectivity between two distant nodes without reliable direct communication link;

(d) Broadcasting, where drone transmits common information to all ground devices.

In this thesis, we focus on the use of drones as ABSs to provide additional coverage for temporary events, such as concerts or sports events. Such temporary events are happening more frequently in cities all over the world with very high number of users gathering. A large number of IoT devices are expected to be deployed in a stadium to help the event operators to provide superior experience to event participants

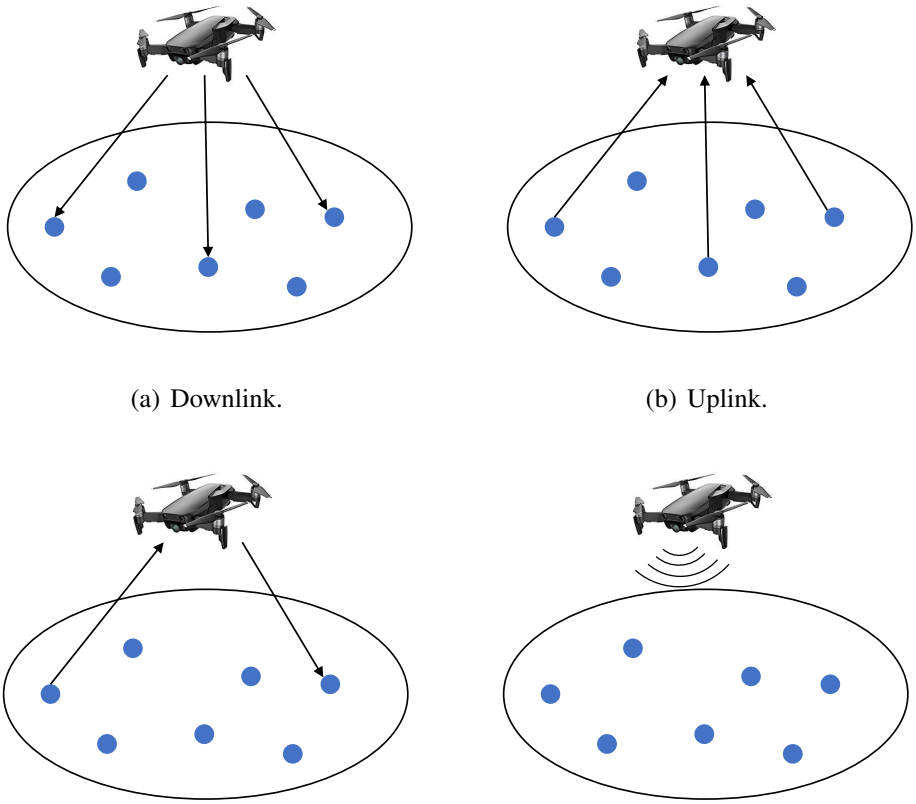

(a) Downlink. (b) Uplink.

(c) Relaying. (d) Broadcasting.

Figure 1.1: Drone communication models.

efficiently and effectively. Note that network users inside a stadium are not limited to smartphones, but can also be security cameras, noise and temperature sensors inside the stadium and performance monitoring devices on the sports players. For example, security cameras being used to monitor all corners of the venue and keep the crowd safe. Sensors being used to provide up-to-date information on queues for merchandise stalls. Temperature sensors being used to monitor and control the air conditioning system. Therefore, effective and reliable wireless connectivity, high data rates and ultra low latency are required. It is not possible to rely solely on the conventional wireless networks (e.g., cellular system) to support all these network devices. The high data rates and the numerous number of connected network nodes would quickly and constantly overload base stations and put pressure on network resources. Therefore, assessing the usefulness of ABSs to provide downlink and uplink coverage for temporary events is an important open problem in the literature which has great practical

importance as well.

Natural and human-instigated disasters, such as bushfires and floods, strike countries such as Australia every year. They cause loss of life, injury, property damage and economic disruption. In unexpected public safety situations, fast, flexible and reliable emergency communication systems will not only provide ubiquitous connectivity, but can also minimize and even prevent the loss for the affected community. However, the existing terrestrial communication infrastructures can be partially or completely damaged during the disasters. Moreover, wireless network coverage may not reach all locations where mobile terminals are located, such as rural areas and forests. In this regard, drones can be used to fulfill the vital need of public safety communications by broadcasting common emergency information to a large number of ground nodes. Furthermore, D2D communications is an effective technique for network coverage improvement in terrestrial communication systems by enabling direct communications between nearby mobile terminals [12]. Therefore, efficient and rapid emergency information dissemination can be achieved in public safety scenarios by exploiting both D2D communications and drone mobility. The investigation of drone-assisted D2D networks for the rapid spread of emergency messages in public safety scenarios is a timely and significant open problem in the literature which is addressed in this thesis.

1.1.2 Wireless Power Transfer Networks

Due to the proliferation of mobile devices with powerful processing capabilities such as smart phones, tablets, and personal digital assistants, the demand for long battery life is increasing significantly [13]. WPT is an emerging and promising next generation technology to maximise the lifetime of energy constrained wireless communication networks in comparison with other possible techniques. Ongoing studies have focused on converting energy embedded in the ambient environment to the DC electrical power in a process known as energy harvesting. Compared to energy harvesting from ambient energy sources, e.g., solar power, wind energy, thermal energy, kinetic energy from human walking or ambient man-made radio-frequency (RF) electromagnetic wave, which may change rapidly with time, location and weather conditions, WPT leveraging the property that wireless signal carries both information and energy has a significant advantage of being always available and controllable [13]. There are currently two main approaches to WPT: (i) simultaneous wireless information and power transfer (SWIPT) and (ii) power beacon (PB) based approach.

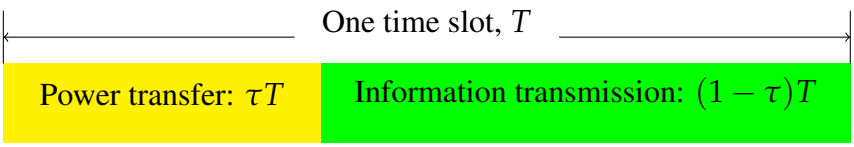

Figure 1.2: Illustration of the harvest-then-transmit TX architecture.

In SWIPT network, the receiver (RX) extracts the information and energy simultaneously from the same wireless signal transmitted by RF signal transmitters (TXs). The two common SWIPT practical RX architectures adopted in the literature are time switching and power splitting. For the time switching RX architecture, the receiving antenna is periodically switched between the information decoding RX and the energy harvesting RX, which have time slots with different lengths [14]. In this way, the SWIPT RX is able to detect information for a certain time, and harvesting energy in the rest of the time. For the power splitting RX architecture, the power of the received signal at the antenna is split into two separate streams with different magnitudes by a passive power splitter, one is used for energy harvesting and the other is used for information decoding [14]. Besides the two architectures mentioned above, there are other SWIPT RX architectures proposed in the literature, such as antenna switching RX architecture and integrated information decoding/energy harvesting RX architecture [15].

While SWIPT has been the subject of intense research in the academic community [13, 14, 16, 17], industry has preferred to adopt the PB approach. In this approach, low cost PBs, which do not require backhaul links, are deployed to provide dedicated power transfer in wireless networks. For example, the Cota Tile is a PB designed to wirelessly charge devices like smartphones in a home environment and was showcased at the 2017 Consumer Electronics Show (CES) [18].

For PB based WPT networks, time is divided into slots and let T denote one time slot. Each TX adopts the harvest-then-transmit architecture to perform power transfer and information transmission, as shown in Figure 1.2. Specifically, each time slot T is divided into two parts with ratio $\tau \in (0,1)$: in the first τT seconds TXs harvest energy from the RF signal transmitted by randomly deployed PBs. In the remaining $(1-\tau)T$ seconds, TXs use all the harvested energy to transmit information to their desired RXs.

There are two key challenges in the application of PBs to wider networks. The first challenge is the lack of tractable models for analysis and design of such networks.

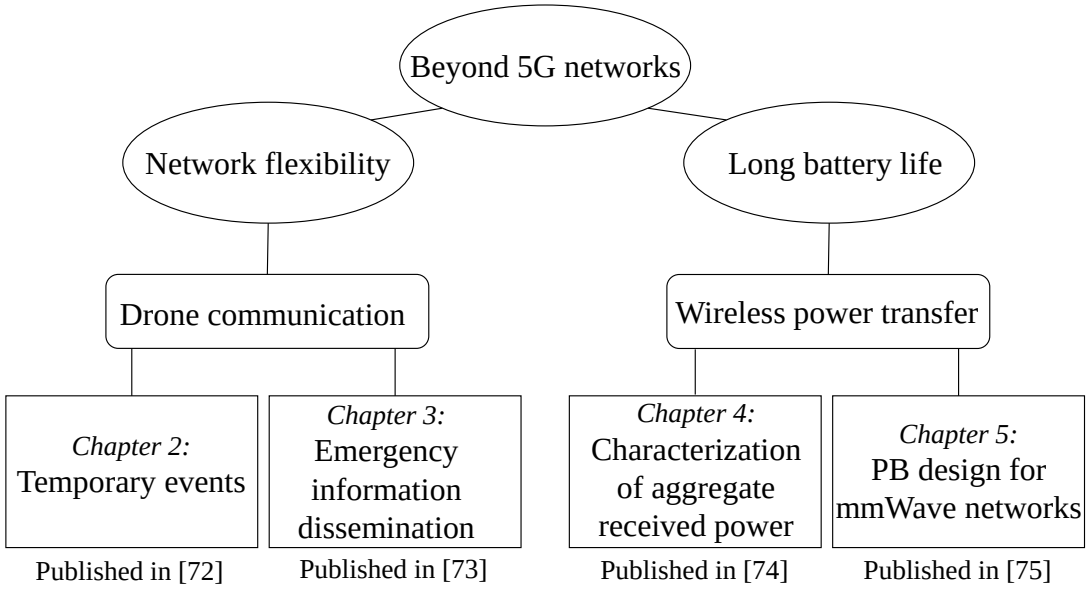

Figure 1.3: Overview of the thesis.

Although large-scale Monte Carlo simulations can be used in this regard, exhaustive simulation of every possible scenario of interest will be extremely time-consuming and onerous. The insights and relationships of different system parameters drawn are restricted by the possibility and repeatability of the simulations. Hence, it is important to explore tractable, efficient and accurate analytical models for PB-assisted communications in wireless networks. The second challenge is the use of practical models for WPT, which capture realistic aspects of WPT. For instance, practical state-of-art RF energy harvesting circuits have power sensitivity requirement and WPT RXs can only harvest power if the incident received power is greater than the power circuit activation threshold (typically around -20 dBm [13]). Similarly, WPT TXs have to adhere to maximum transmit power constraints due to safety considerations. Therefore, it is important to adopt a realistic and practical model for WPT process in analyzing the performance of PB-assisted wireless communication networks.

This thesis aims to tackle the research challenges identified above and applies stochastic geometry to model, analyze and design the integration of drone and PB based WPT techniques into beyond 5G networks in Chapters 2 – 5. Figure 1.3 shows an overview of the thesis. In the remainder of this chapter, we first discuss the relevant existing studies in the literature on drone communication networks and WPT networks. Finally, the scope and contributions of the thesis are summarized in Section 1.3.

1.2 Literature Review

This section describes the state of the art work that is relevant to this thesis and is divided into two parts. Section 1.2.1 summarizes the recent work on drone communication networks. Next, Section 1.2.2 presents an overview of current studies on WPT networks.

1.2.1 Drone Communication Networks

Depending on the use of drones as base stations or as aerial users, the integration of drones into cellular networks can be categorized into two main paradigms [11]: (i) drone-assisted wireless communications and (ii) cellular-connected drones. For both paradigms, an essential requirement is accurate drone channel model. The work in [19] presented a comprehensive overview of existing research related to aerial (also known as air-to-ground) channel measurements, including large and small-scale fading channel models. Models for path-loss exponents and shadowing for the aerial radio channel between drones and cellular networks were presented in [20, 21] based on field measurements. Using the general geometrical statistics of various environments provided by the International Telecommunication Union (ITU-R), the authors proposed location and environment dependent path-loss model for low altitude platforms in [1, 22].

In this thesis, our focus is on drone-assisted wireless networks. The investigation of these networks has drawn attention in the literature from different perspectives, such as drone deployment and optimization of trajectories [1, 23, 24, 25, 26, 27, 28, 29] and performance analysis of drone enable cellular systems [30, 31, 32, 33, 34, 35]. Optimal drone trajectory was designed for a drone base station in cellular network in [23] and for a drone enabled relaying network in [24]. An analytical model for finding optimal placement of a drone was provided in [25] to maximize the number of covered users and optimal height and antenna beamwidth was found in [26] for throughput optimization. Optimal density of the underlay drones was investigated in [27] and optimal placement for multiple drones in a large-scale network was studied in [28]. The work in [29] studied the joint user scheduling and drone trajectory optimization for maximizing the minimum average rate of ground users. In [1], the authors derived the optimal altitude enabling a single drone to achieve a maximum coverage radius on the ground. [30] investigated the uplink performance of a drone cell in the presence of a Poisson field of ground interferers. The downlink performance of a single static

drone and a single mobile drone with underlay D2D users was studied in [31], while [32] analyzed the downlink coverage of a finite network formed by multiple drones. The downlink coverage probability of a network with multiple directional beamforming drones was investigated in [33]. The downlink coverage performance of multiple drones in an urban environment was studied in [34]. The downlink coverage and rate in a Poisson field of drone base stations was investigated in [35]. In particular, we focus on the works related to temporary events and information dissemination.

Temporary events:

Recently, there are some works investigating the application of drone in temporary events from different aspects. Specifically, the Aerial Base Stations with Opportunistic Links for Unexpected and Temporary Events (ABSOLUTE) project in Europe aims to provide reliable network coverage through a combination of aerial, terrestrial and satellite links for unexpected and temporary events [36]. A heuristically accelerated reinforcement learning based framework was proposed in [37] for dynamic spectrum sharing in a temporary event scenario. In [38], the authors constructed a non-cooperative game and studied the equilibrium beaconing durations in terms of energy efficiency of the competing drones for temporary events. A proactive drone cell deployment scheme was investigated in [39] to cope with flash crowd traffic in different scenarios, including stadiums. A limited feedback scheme for non-orthogonal multiple access was designed for mmWave drone to provide coverage over a stadium in [40].

The above literature review motivates the performance analysis of drone in a temporary event scenario using stochastic geometry. In particular, this thesis studies the performance of cellular network with underlay drone cell dedicated to provide coverage for IoT devices inside a stadium for a temporary event.

Information dissemination:

Furthermore, we are interested in utilizing drone for information dissemination. By exploiting both D2D communications and the drone mobility, the authors presented an idea to use D2D communications to help drone to achieve efficient information dissemination to a large number of ground nodes in [8]. An energy efficient data dissemination approach based on the fire fly optimization algorithm was proposed in [41] for wireless sensor networks by the use of multiple drones. Optimal transmission strategy for data dissemination was investigated in [42] to maximize the network throughput

of a cooperative drone assisted VANETs while guarantee the delay constraint. In [43], the authors studied the data dissemination problem in VANETs with the assistance of drones as relay nodes. The recursive least squares algorithm and the maximum vehicle coverage algorithm were proposed to maximize the system throughput and minimize the transmission delay.

There are also some previous works on multicast transmission without the assistance from drone [44, 45, 46, 47, 48]. For example, the time and the average energy consumption of serving a content request via D2D unicast and multicast content delivery were investigated in [44]. In [45], the joint optimization of power control and channel allocations was studied to maximize the aggregate rate of a cellular network with unicast cellular users and underlay multicast D2D users. In [46], the authors analyzed the coverage probability, the mean number of covered RXs and the throughput of a multicast D2D network with and without the help from overlay cellular networks and explored how to improve the network performance by optimizing the multicast rate and the number of retransmission times. The average multicast rate and the outage rate of small-scale two-hop D2D multicast networks were studied in [47]. In [48], the authors investigated the multicast transmission capacity of single-hop and multihop multicast ad hoc networks. For the multihop scheme, each multicast cluster was considered to tessellate into smaller multicast regions of equal area. A packet was assumed to deliver slot by slot from one region to the next until all the tessellated regions have been visited by the packet.

The above mentioned works motivate the investigation of drone-assisted multihop multicast D2D network, where an emergency alert message broadcasted by a drone at the first time slot is multicasted by the D2D users that have successfully received the message through multihop. To the best of our knowledge, this scenario and its study have not yet been presented in the literature to date.

1.2.2 Wireless Power Transfer Networks

Establishing fully sustainable communication networks has attracted significant research interest very recently. Although, periodic battery replacement or recharging can avoid the need for the energy harvesting process, it suffers from a high cost and can be inconvenient or dangerous (e.g., in a toxic environment), or highly undesirable (e.g., sensors inside human body) [14]. Therefore, WPT which can prolong the lifetime of low-power devices in the network, is currently in the spotlight as a key

enabling technology in future wireless communication networks [13, 49, 50].

In WPT systems, the aggregate received power (which determines the harvested power) plays a key role in the system performance. For instance, (i) in SWIPT systems, a common assumption is that the energy constrained node has a large battery to store the received power and, therefore, it transmits with a constant transmit power which is proportional to the aggregate received power [51, 52], (ii) in PB systems, the complementary cumulative distribution function (CCDF) of the aggregate received power plays a key role in determining the power outage probability [53, 54, 55], and (iii) in low power applications, statistical information such as the mean and variance of the aggregate received power can potentially be used to develop efficient sleep and transmission protocols [13, 56]. Thus, it is crucial to accurately characterize the aggregate received power. In this regard, the moment generating function (MGF) of the aggregate received power, which opens the door for application of powerful toolsets from stochastic geometry, has been numerically evaluated in microwave cellular and D2D networks with ambient RF energy harvesting [57, 58], mmWave SWIPT systems [59, 60] and microwave PB systems [54].

To the best of our knowledge, a closed-form expression for the MGF of the aggregate received power in mmWave PB systems, incorporating the key propagation characteristics of mmWave transmission, is not available in the literature.

Microwave (below 6 GHz) systems:

Recently, the investigation of PBs has drawn attention in the literature from different aspects. *For point-to-point or point-to-multipoint communication systems*, the resource allocation for PB-assisted system was considered in [61, 62], where the authors mainly aimed at finding the optimum time ratio for power transfer and information transmission. In [63], the authors studied the PB-assisted network in the context of physical layer security, where an energy constrained source is powered by a dedicated PB. For *large scale networks*, some papers have characterized the performance of PB-assisted communications using stochastic geometry, which is a powerful mathematical tool to provide tractable analysis by incorporating the randomness of users. Specifically, the feasibility of PB deployment in a cellular network, under the outage constraint at the base station, was investigated in [53], where cellular users are charged by PBs for uplink transmission. By considering that the secondary TX is charged by the primary user in a cognitive network, the authors derived the spatial throughput for the secondary network in [64]. Adaptively directional PBs were proposed for sensor

network in [65] and the authors found the optimal charging radius for different sensing tasks. In [66], three WPT schemes were proposed to select the PB for charging in a D2D-aided cognitive cellular network. The authors in [54] formulated the total outage probability in a PB-assisted ad hoc network by including the energy harvesting sensitivity into the analysis. Note that all the aforementioned works considered the conventional microwave frequency band, i.e., below 6 GHz.

MmWave systems:

MmWave communication, which aims to use the spectrum band typically around 30 GHz, is emerging as a key technology for the 5G systems [67]. Considerable advancements have already been made in the understanding, modeling and analysis of mmWave communication using stochastic geometry [68, 69, 70, 71]. From the prior work, we can summarize two distinctive features of mmWave communication: (i) owing to the smaller wavelength, mmWave allows a large number of antenna arrays with directional beamforming to be equipped at the TX and RX; (ii) since the mmWave propagation is susceptible to blockage, it causes the large difference for path-loss and fading characteristics between line-of-sight (LOS) and non-line-of-sight (NLOS) environment.

MmWave communication can be beneficial for WPT since both technologies inherently operate over short distances and the narrow beams in mmWave communication can focus the transmit power. Very recently, some papers have used stochastic geometry to analyse mmWave SWIPT networks [59, 60].

To the best of our knowledge, the study of a PB-assisted mmWave network using stochastic geometry, taking into account realistic and practical WPT and mmWave characteristics such as building blockages, beamforming, power circuit activation threshold, maximum harvested power and maximum transmit power, is not available in the literature.

1.3 Thesis Overview and Contributions

The main focus of this thesis is to investigate two critical requirements for beyond 5G networks, which are network flexibility and long battery life. In this regard, we focus on the modeling, analysis and design of the integration of drone and WPT techniques into wireless communication networks using stochastic geometry. In the first half of

the thesis, we explore the use of drones to provide flexible communication networks for temporary events and emergency information dissemination. The second half of the thesis looks into the use of PBs in a mmWave wireless ad hoc network. The specific contributions of each chapter are detailed below:

Chapter 2 - Underlay Drone Cell for Temporary Events: Impact of Drone Height and Aerial Channel Environments

Chapter 2 considers a drone system coexisting with a single-cell cellular network, where an ABS is designated to provide service to IoT devices (namely the ABS-supported devices (AsDs), such as smartphones, security cameras, noise and temperature sensors and performance monitoring devices) inside a stadium for a temporary event (e.g., a concert or a sporting event). Since the ABS shares the same spectrum resources (i.e., in an underlay fashion) with the TBS, the concurrent transmission of both systems can cause interference to each other and impact the network performance. In Chapter 2, we consider a general aerial channel model and study both uplink and downlink network performance. The novel contributions of the chapter are summarized as follows:

- Leveraging tools from stochastic geometry, we develop a general analytical framework to analyze the uplink coverage probability of the TBS and the ABS and the downlink coverage probability of the TBS-supported user equipment (TsUE) and the AsD. The proposed framework is able to accommodate any aerial channel model.

- Our proposed framework depends on the Laplace transforms of the interference power distribution at the TBS, the ABS, the TsUE and the AsD. We derive the key factors that determining the Laplace transforms of the interference power distribution, the distribution function of the three-dimensional distance between the ABS and an independently and uniformly distributed (i.u.d.) AsD and the distribution function of the three-dimensional distance between the ABS and an i.u.d. TsUE. Note that such distance distributions take into account the hole effects (i.e., the TsUE are prohibited from the ABS serving region and the AsD are contained in the ABS serving region).

- Our results show that for urban environment and dense urban environment the ABS is best deployed at a low height (e.g., 200 m or lower), regardless of the

distance between the center of the stadium and the TBS. However, for suburban environment and high-rise urban environment, the best ABS deployment height depends on the distance between the center of the stadium and the TBS and the task of the system (i.e., prioritize the terrestrial link or the aerial link, prioritize the uplink or the downlink communication).

The results of this chapter have appeared in the following publication [72]:

J2. X. Zhou, S. Durrani, J. Guo, and H. Yanikomeroglu, "Underlay Drone Cell for Temporary Events: Impact of Drone Height and Aerial Channel Environments," *IEEE Internet Things J.*, vol. 6, no. 2, pp. 1704–1718, Apr. 2019.

Chapter 3 - Drone-assisted Multihop Multicast Device-to-Device Networks for Emergency Information Dissemination

Chapter 3 explores the use of drone for emergency information dissemination in public safety scenarios. We consider a drone-assisted multihop multicast D2D network where a drone is deployed to broadcast an emergency alert message to all terrestrial D2D users at the first time slot. After that, the drone leaves and the D2D users that have successfully received the message become the active TXs for the next time slots to multicast the emergency alert message through multihop. Using stochastic geometry, we investigate the link coverage probability and the mean local delay for a D2D user and the network coverage probability. The main contributions of the chapter are as follows:

- We propose a general analytical framework to compute the link coverage probability and the mean local delay for a D2D user in terms of the link success probability, the network outage probability and the Laplace transform of the aggregate received signal power. The framework is able to accommodate any aerial channel model.

- For tractable analysis of the network performance, we propose an approximation for the link success probability. Using this approximated link success probability, we derive the network success probability and the network coverage probability. The simulation results verify the accuracy of the approximation.

- Based on our proposed models, we analyze the effect of the different system parameters (i.e., height and transmit power of the drone and density and sensitivity radius of the D2D users) on the link coverage probability and the mean local delay of a D2D user and the network coverage probability.

The results of this chapter are under preparation for journal paper submission [73]:

J3. **X. Zhou**, S. Durrani, and J. Guo, "Drone-initiated D2D-aided Multihop Multicast Networks for Emergency Information Dissemination," submitted to *IEEE Access*, under major revision.

Chapter 4 - Characterization of Aggregate Received Power from Power Beacons in Millimeter Wave Ad Hoc Networks

In Chapter 4, we consider a mmWave wireless ad hoc network where PBs are deployed. Using stochastic geometry, we characterize the aggregate received power at a reference RX. The aggregate received power plays a key part in determining the overall system performance, which is discussed in Chapter 5. The novel contributions of the chapter are:

- We derive the closed-form expressions for the MGF and the nth cumulant of the aggregate received power at the reference RX, taking a mmWave three-state propagation model and multi-slope path-loss model into account. The MGF allows the CCDF of the aggregate received power from PBs to be numerically evaluated.

- We test the accuracy of well known closed-form distributions to model the aggregate received power. Our results show that the lognormal distribution provides the best CCDF approximation, compared to other distributions commonly considered in the literature.

- We investigate the feasibility of PBs to power users in a mmWave ad hoc network. Our results show that under practical setups, for PB deployment density between $10 - 100$ per km^2, the required PB transmit power to achieve an average harvested power of 15 dBm is between $1.5 - 40$ W, which is practical and safe for human exposure.

The results of this chapter have appeared in the following publication [74]:

C1. **X. Zhou**, S. Durrani, and J. Guo, "Characterization of Aggregate Received Power from Power Beacons in Millimeter Wave Ad Hoc Networks," in *Proc. IEEE ICC*, May. 2017.

Chapter 5 - Power Beacon-Assisted Millimeter Wave Ad Hoc Networks

In Chapter 5, we consider a PB-assisted wireless ad hoc network under mmWave transmission where TXs adopt the harvest-then-transmit protocol, i.e., they harvest energy from the aggregate RF signal transmitted by PBs and then use the harvested energy to transmit the information to their desired RXs. Both the power transfer and information transmission phases are carried out using antenna beamforming under the mmWave channel environment, which is subjected to building blockages. Using tools from stochastic geometry, we develop a tractable analytical framework to investigate the power coverage probability, the channel coverage probability and the total coverage probability at a reference RX taking a mmWave three-state propagation model and multi-slope bounded path-loss model into account. In the proposed framework, the power coverage probability is efficiently and accurately computed by numerical inversion using the closed-form expression for the Laplace transform of the aggregate received power at the typical TX. The novel contributions of this chapter are summarized as follows:

- We adopt a realistic model of wirelessly powered TXs by taking into consideration (i) the power circuit activation threshold, which accounts for the minimum aggregate received power required to activate the energy harvesting circuit, (ii) the allowed maximum harvested power, which accounts for the saturation of the energy harvesting circuit and (iii) the maximum transmit power, which accounts for the safety regulation and the electrical rating of the antenna circuit.

- For tractable analysis of the channel coverage probability and the total coverage probability, we propose to discretize the transmit power of each TX into a finite number of discrete power levels in the log scale. Using this approximation, we derive the channel coverage probability and the total coverage probability at the typical RX. Comparison with simulation results shows that the model, with only 10 discrete levels for the transmit power of TXs, has good accuracy in the range of $5\% - 10\%$.

- Based on our proposed model, we investigate the impact of varying important system parameters (e.g., PB transmit power, PB density, allowed maximum harvested power, directional beamforming parameters etc.) on the network performance.

- We investigate the feasibility of using PBs to power up TXs while providing an acceptable performance for information transmission towards RXs in mmWave ad hoc network. Our results show that under practical setups, for PB transmit power of 50 dBm and TXs with a maximum transmit power between $20 - 40$ dBm, which are safe for human exposure, the total coverage probability is around 90%.

The results of this chapter have appeared in the following publication [75]:

J1. X. Zhou, J. Guo, S. Durrani, and M. D. Renzo, "Power Beacon-Assisted Millimeter Wave Ad Hoc Networks," *IEEE Trans. Commun.*, vol. 66, no. 2, pp. 830–844, Feb. 2018.

Chapter 2

Underlay Drone Cell for Temporary Events: Impact of Drone Height and Aerial Channel Environments

Providing seamless connection to a large number of IoT devices is one of the biggest challenges for beyond 5G networks. Using a drone as an ABS to provide coverage to IoT devices or mobile terminals on ground is envisaged as a promising solution for beyond 5G networks. In this chapter, we consider a communication network with an underlay ABS to provide coverage for a temporary event, such as a sporting event or a concert in a stadium. Using stochastic geometry, we propose a general analytical framework to compute the uplink and downlink coverage probabilities for both the aerial and the terrestrial cellular system. Our framework is valid for any aerial channel model for which the probabilistic functions of LOS and NLOS links are specified. The accuracy of the analytical results is verified by Monte Carlo simulations considering two commonly adopted aerial channel models. Our results show the non-trivial impact of the different aerial channel environments (i.e., suburban, urban, dense urban and high-rise urban) on the uplink and downlink coverage probabilities and provide design guidelines for best ABS deployment height.

The chapter is organized as follows: Section 2.1 describes the system model and assumptions. Section 2.2 focuses on the uplink coverage probability at the TBS and the ABS. Section 2.3 details the analysis of the downlink coverage probability at the TsUE and the AsD. Section 2.4 presents the results and the effect of the system parameters on the network performance. Finally, the chapter is summarized in Section 2.5.

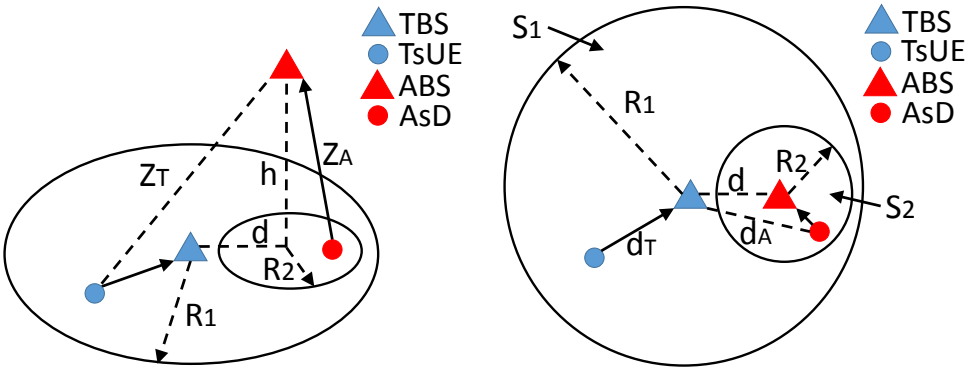

(a) Three-dimensional view. (b) Projection on the ground.

Figure 2.1: Illustration of the underlay drone cell system model.

2.1 System Model

A two-cell communication network comprised of a TBS and an ABS is considered, where the network region $\mathcal{S}_1$ is a disk with radius R_1, i.e., $|\mathcal{S}_1| = \pi R_1^2$ and a TBS is located at the center. We assume that there is a temporary event held inside a stadium within the network region and a large number of IoT devices are active inside the stadium. The stadium's building area $\mathcal{S}_2$ is modeled as a disk with radius R_2 and its center is at a distance d from the TBS. A drone is placed as an ABS[1] to provide additional resources for the event. The ABS is assumed to be deployed at a height of h above the center of the stadium, as shown in Figure 2.1. The TsUEs served by the TBS are uniformly distributed over the network region excluding the stadium, i.e., $\mathcal{S}_1 \setminus \mathcal{S}_2$. At the same time, the AsDs[2] are independently uniformly deployed on the ground inside the stadium $\mathcal{S}_2$. For tractability, we assume that all AsDs are connected to the ABS only. In this chapter, we focus our analysis on one terrestrial cell and its underlay drone cell without inter terrestrial cell interference. This is based on the assumption that the terrestrial adjacent cells use different frequencies, while the TBS and the underlay ABS share the same spectrum resource. Hence, the interference from far away cells becomes negligible and can be ignored [39, 76]. Note that the single terrestrial cell model is commonly used in literature for underlay network analysis [77, 78].

[1]Current drone regulations prohibit a drone from flying over stadiums or sports events. This is expected to change in the future.

[2]The analysis in this chapter focuses on single channel use, so an assumption on the number of TsUEs or AsDs is not required.

2.1.1 Channel Model

There are two types of communication links in the considered system model: aerial links and terrestrial links. The link between the TsUE and the TBS and the link between the AsD and the TBS are terrestrial links. The link between the TsUE and the ABS and the link between the AsD and the ABS are aerial links.

Terrestrial links: A general power-law path-loss model is considered for terrestrial links, in which the signal power decays at a rate $\ell^{-\alpha_{\mathrm{T}}}$ with the propagation distance ℓ and α_{T} is the path-loss exponent. Furthermore, we assume the terrestrial links experience small-scale Rayleigh fading and additive white Gaussian noise (AWGN) with variance σ^2.

Aerial links: The channel characteristics of the aerial links (or known as air-to-ground links) are significantly different from the terrestrial links. Depending on altitude and type of the drone, elevation angle and type of propagation environment, the aerial links can be either LOS or NLOS with different probabilities of occurrence p_{L} and p_{N} [22].

The path-loss of the NLOS link is higher than LOS one, because of the shadowing effect and the reflection of signals from obstacles. Following [31], the path-loss of the aerial link is modeled as

$$PL_a(z) = \begin{cases} \eta_{\mathrm{L}} z^{-\alpha_{\mathrm{L}}}, & \text{LOS} \\ \eta_{\mathrm{N}} z^{-\alpha_{\mathrm{N}}}, & \text{NLOS} \end{cases}, \tag{2.1}$$

where z is the three-dimensional propagation distance between the TsUE and the ABS and between the AsD and the ABS, α_{L} and α_{N} is the path-loss exponent of LOS aerial link and NLOS aerial link respectively, η_{L} and η_{N} is the additional attenuation factor for LOS aerial link and NLOS aerial link respectively and $\eta_{\mathrm{L}} > \eta_{\mathrm{N}}$.

Most previous works using aerial channel model ignore the impact of small-scale fading [25, 31]. However, small-scale fading characteristics are measured and reported in the literature recently for various aerial propagation environments [19]. In this chapter, the small-scale fading of the aerial link is modeled as Nakagami-m fading, which is a flexible model that mimics various fading environments. For example, Nakagami-m fading is equivalent to Rayleigh fading when m equals to 1 and Nakagami-m fading can also closely approximate Rician fading by matching the m values. The fading parameter for the LOS aerial link and NLOS aerial link is denoted by m_{L} and m_{N} respectively. The difference between including and ignoring the small-scale fading

will be discussed in the result section. The aerial links also experience AWGN with variance σ^2.

2.1.2 Uplink Network Model

For uplink, we assume that orthogonal multiple access technique is employed [79]. Hence, there is no interference among TsUEs (or AsDs). However, both the TBS and the ABS share the same spectrum resource, i.e., in an underlay fashion. We assume that the number of the TsUEs and the AsDs are sufficiently high. That is to say, there will always be one TsUE and one AsD to be served per each channel at the same time. Therefore, interference exists between TsUEs and AsDs. In this chapter, we focus our analysis on one uplink channel since other channels share the same interference statistics.

For reliable and successful uplink communication, the TsUE controls its transmit power such that the average signal received at the TBS is equal to the RX sensitivity ρ_{T}. Power control is deployed at the AsD as well. Perfect channel state information (CSI) knowledge is assumed at TsUE and AsD. We also set a maximum transmit power constraint at the AsD, to avoid the transmit power for AsD going to very large when the ABS is placed at a high altitude. In other words, the AsD compensates for the path-loss to keep the average signal power at the ABS equal to the RX sensitivity ρ_{A} if the transmit power required for the path-loss inversion is less than $P_{\mathrm{AsD}}^{\max}$. Otherwise, the AsD tries to establish an uplink connection with the ABS by transmitting with a power of $P_{\mathrm{AsD}}^{\max}$. Therefore, the instantaneous transmit power for the AsD, P_{AsD}, depends on the propagation distance between the AsD and the ABS and can be shown as:

$$P_{\mathrm{AsD}}=\begin{cases} \left.\begin{array}{ll} P_{\mathrm{AsD}}^{\max}, & \text{cond.1L} \;||\; \left(\text{cond.2L} \;\&\; \mathcal{Z}_A > \left(\dfrac{P_{\mathrm{AsD}}^{\max}\eta_{\mathrm{L}}}{\rho_{\mathrm{A}}}\right)^{\frac{1}{\alpha_{\mathrm{L}}}}\right) \\ \dfrac{\rho_{\mathrm{A}}}{\eta_{\mathrm{L}}}\mathcal{Z}_A^{\alpha_{\mathrm{L}}}, & \text{cond.3L} \;||\; \left(\text{cond.2L} \;\&\; \mathcal{Z}_A < \left(\dfrac{P_{\mathrm{AsD}}^{\max}\eta_{\mathrm{L}}}{\rho_{\mathrm{A}}}\right)^{\frac{1}{\alpha_{\mathrm{L}}}}\right) \end{array}\right\}\text{LOS} \\ \left.\begin{array}{ll} P_{\mathrm{AsD}}^{\max}, & \text{cond.1N} \;||\; \left(\text{cond.2N} \;\&\; \mathcal{Z}_A > \left(\dfrac{P_{\mathrm{AsD}}^{\max}\eta_{\mathrm{N}}}{\rho_{\mathrm{A}}}\right)^{\frac{1}{\alpha_{\mathrm{N}}}}\right) \\ \dfrac{\rho_{\mathrm{A}}}{\eta_{\mathrm{N}}}\mathcal{Z}_A^{\alpha_{\mathrm{N}}}, & \text{cond.3N} \;||\; \left(\text{cond.2N} \;\&\; \mathcal{Z}_A < \left(\dfrac{P_{\mathrm{AsD}}^{\max}\eta_{\mathrm{N}}}{\rho_{\mathrm{A}}}\right)^{\frac{1}{\alpha_{\mathrm{N}}}}\right) \end{array}\right\}\text{NLOS} \end{cases}, \quad (2.2)$$

where $\mathcal{Z}_A$ is the Euclidean distance between the AsD and the ABS and the conditions

are:

$$\text{cond.1k} : h \geqslant \left(\frac{P_{\text{AsD}}^{\max}\eta_{\text{k}}}{\rho_{\text{A}}}\right)^{\frac{1}{\alpha_{\text{k}}}}, \tag{2.3}$$

$$\text{cond.2k} : \sqrt{\left(\frac{P_{\text{AsD}}^{\max}\eta_{\text{k}}}{\rho_{\text{A}}}\right)^{\frac{2}{\alpha_{\text{k}}}} - R_2^2} < h < \left(\frac{P_{\text{AsD}}^{\max}\eta_{\text{k}}}{\rho_{\text{A}}}\right)^{\frac{1}{\alpha_{\text{k}}}}, \tag{2.4}$$

$$\text{cond.3k} : h \leqslant \sqrt{\left(\frac{P_{\text{AsD}}^{\max}\eta_{\text{k}}}{\rho_{\text{A}}}\right)^{\frac{2}{\alpha_{\text{k}}}} - R_2^2}, \tag{2.5}$$

where k (in η_{k} and α_{k}) is L for LOS case or N for NLOS case. These conditions come from the fact that AsD will transmit with its maximum power regardless of where it is located inside the stadium, if the ABS is placed at a high enough altitude. On the other hand, the AsD will always be under full channel inversion if the altitude of the ABS is low.

SINR: For the considered setup, the instantaneous uplink signal-to-interference-plus-noise ratio (SINR) at the TBS is given as

$$\mathsf{SINR}_{\text{T}}^{u} = \frac{P_{\text{TsUE}} H_T^u d_T^{-\alpha_{\text{T}}}}{P_{\text{AsD}} H_A^u d_A^{-\alpha_{\text{T}}} + \sigma^2} = \frac{\rho_{\text{T}} H_T^u}{P_{\text{AsD}} H_A^u d_A^{-\alpha_{\text{T}}} + \sigma^2}, \tag{2.6}$$

where $P_{\text{TsUE}} = \rho_{\text{T}} d_T^{\alpha_{\text{T}}}$ is the TsUE transmit power. H_T^u and H_A^u are the uplink fading power gain between the TsUE and the TBS and between the AsD and the TBS, respectively, which follow exponential distribution. d_T and d_A are the Euclidean distance between the TsUE and the TBS and between the AsD and the TBS, respectively. The transmit power of the AsD P_{AsD} is given in (2.2).

The instantaneous uplink SINR at the ABS is given as

$$\mathsf{SINR}_{\text{A}}^{u} = \frac{P_{\text{AsD}} G_A^u PL_a(\mathcal{Z}_A)}{P_{\text{TsUE}} G_T^u PL_a(\mathcal{Z}_T) + \sigma^2}, \tag{2.7}$$

where G_A^u and G_T^u are the uplink fading power gain between the AsD and the ABS and between the TsUE and the ABS, respectively, which follow Gamma distribution. $\mathcal{Z}_A$ and $\mathcal{Z}_T$ are the Euclidean distance between the AsD and the ABS and between the TsUE and the ABS, respectively.

2.1.3 Downlink Network Model

Different from uplink transmission, the TBS and ABS are assumed to transmit at a constant power P_{TBS} and P_{ABS} respectively.

SINR: For the considered setup, the instantaneous downlink SINR at the TsUE is given as

$$\mathsf{SINR}_{\text{T}}^{d} = \frac{P_{\text{TBS}} H_T^d d_T^{-\alpha_{\text{T}}}}{P_{\text{ABS}} G_T^d PL_a(\mathcal{Z}_T) + \sigma^2}, \tag{2.8}$$

where H_T^d is the downlink fading power gain between the TsUE and the TBS, which follows exponential distribution and G_T^d is the downlink fading power gain between the TsUE and the ABS, which follows Gamma distribution.

The instantaneous downlink SINR at the AsD is given as

$$\mathsf{SINR}_{\text{A}}^{d} = \frac{P_{\text{ABS}} G_A^d PL_a(\mathcal{Z}_A)}{P_{\text{TBS}} H_A^d d_A^{-\alpha_{\text{T}}} + \sigma^2}, \tag{2.9}$$

where G_A^d is the downlink fading power gain between the AsD and the ABS, which follows Gamma distribution and H_A^d is the downlink fading power gain between the AsD and the TBS, which follows exponential distribution.

2.2 Uplink Coverage Probability

In this section, we propose the analytical framework to compute the uplink performance by adopting coverage probability as the performance metric. The uplink coverage probability is formally defined as

$$\mathbb{P}_{\text{cov}}^{u,b} \triangleq \Pr(\mathsf{SINR}_b^u > \gamma_b^u), \tag{2.10}$$

where superscript b is T for TBS and A for ABS, and γ_b^u is the uplink SINR threshold. $\mathsf{SINR}_{\text{T}}^u$ and $\mathsf{SINR}_{\text{A}}^u$ can be found in (2.6) and (2.7), respectively. The results for the uplink coverage probability of the TBS and the ABS are presented in the next two subsections.

2.2.1 TBS Uplink Coverage Probability

First we present two lemmas, which are used in deriving the coverage probability of the TBS in Theorem 1.

Lemma 1 *The Laplace transform of the interference power distribution at the TBS is*

$$\mathcal{L}_{I_{\mathrm{T}}^{u}}(s)=\begin{cases}\int_{h}^{\sqrt{h^2+R_2^2}}\int_{0}^{2\pi}\mathcal{L}_{I_{\mathrm{T}}^{u}}(s,P_{\mathrm{AsD}}^{\max}|\theta,z)\frac{1}{2\pi}f_{\mathcal{Z}_A}(z)\mathrm{d}\theta\mathrm{d}z, & \text{cond.1L}\\ \\ \int_{h}^{(\frac{P_{\mathrm{AsD}}^{\max}\eta_{\mathrm{L}}}{\rho_{\mathrm{A}}})^{\frac{1}{\alpha_{\mathrm{L}}}}}\int_{0}^{2\pi}p_{\mathrm{L}}\mathcal{L}_{I_{\mathrm{T}}^{u}}(s,\frac{\rho_{\mathrm{A}}}{\eta_{\mathrm{L}}}z^{\alpha_{\mathrm{L}}}|\theta,z)\frac{1}{2\pi}f_{\mathcal{Z}_A}(z)\mathrm{d}\theta\mathrm{d}z\\ +\int_{(\frac{P_{\mathrm{AsD}}^{\max}\eta_{\mathrm{L}}}{\rho_{\mathrm{A}}})^{\frac{1}{\alpha_{\mathrm{L}}}}}^{\sqrt{h^2+R_2^2}}\int_{0}^{2\pi}p_{\mathrm{L}}\mathcal{L}_{I_{\mathrm{T}}^{u}}(s,P_{\mathrm{AsD}}^{\max}|\theta,z)\frac{1}{2\pi}f_{\mathcal{Z}_A}(z)\mathrm{d}\theta\mathrm{d}z\\ +\int_{h}^{\sqrt{h^2+R_2^2}}\int_{0}^{2\pi}p_{\mathrm{N}}\mathcal{L}_{I_{\mathrm{T}}^{u}}(s,P_{\mathrm{AsD}}^{\max}|\theta,z)\frac{1}{2\pi}f_{\mathcal{Z}_A}(z)\mathrm{d}\theta\mathrm{d}z, & \text{cond.4 || cond.8}\\ \\ \int_{h}^{(\frac{P_{\mathrm{AsD}}^{\max}\eta_{\mathrm{L}}}{\rho_{\mathrm{A}}})^{\frac{1}{\alpha_{\mathrm{L}}}}}\int_{0}^{2\pi}p_{\mathrm{L}}\mathcal{L}_{I_{\mathrm{T}}^{u}}(s,\frac{\rho_{\mathrm{A}}}{\eta_{\mathrm{L}}}z^{\alpha_{\mathrm{L}}}|\theta,z)\frac{1}{2\pi}f_{\mathcal{Z}_A}(z)\mathrm{d}\theta\mathrm{d}z\\ +\int_{(\frac{P_{\mathrm{AsD}}^{\max}\eta_{\mathrm{L}}}{\rho_{\mathrm{A}}})^{\frac{1}{\alpha_{\mathrm{L}}}}}^{\sqrt{h^2+R_2^2}}\int_{0}^{2\pi}p_{\mathrm{L}}\mathcal{L}_{I_{\mathrm{T}}^{u}}(s,P_{\mathrm{AsD}}^{\max}|\theta,z)\frac{1}{2\pi}f_{\mathcal{Z}_A}(z)\mathrm{d}\theta\mathrm{d}z\\ +\int_{h}^{(\frac{P_{\mathrm{AsD}}^{\max}\eta_{\mathrm{N}}}{\rho_{\mathrm{A}}})^{\frac{1}{\alpha_{\mathrm{N}}}}}\int_{0}^{2\pi}p_{\mathrm{N}}\mathcal{L}_{I_{\mathrm{T}}^{u}}(s,\frac{\rho_{\mathrm{A}}}{\eta_{\mathrm{N}}}z^{\alpha_{\mathrm{N}}}|\theta,z)\frac{1}{2\pi}f_{\mathcal{Z}_A}(z)\mathrm{d}\theta\mathrm{d}z\\ +\int_{(\frac{P_{\mathrm{AsD}}^{\max}\eta_{\mathrm{N}}}{\rho_{\mathrm{A}}})^{\frac{1}{\alpha_{\mathrm{N}}}}}^{\sqrt{h^2+R_2^2}}\int_{0}^{2\pi}p_{\mathrm{N}}\mathcal{L}_{I_{\mathrm{T}}^{u}}(s,P_{\mathrm{AsD}}^{\max}|\theta,z)\frac{1}{2\pi}f_{\mathcal{Z}_A}(z)\mathrm{d}\theta\mathrm{d}z, & \text{cond.5}\\ \\ \int_{h}^{\sqrt{h^2+R_2^2}}\int_{0}^{2\pi}p_{\mathrm{L}}\mathcal{L}_{I_{\mathrm{T}}^{u}}(s,\frac{\rho_{\mathrm{A}}}{\eta_{\mathrm{L}}}z^{\alpha_{\mathrm{L}}}|\theta,z)\frac{1}{2\pi}f_{\mathcal{Z}_A}(z)\mathrm{d}\theta\mathrm{d}z\\ +\int_{h}^{\sqrt{h^2+R_2^2}}\int_{0}^{2\pi}p_{\mathrm{N}}\mathcal{L}_{I_{\mathrm{T}}^{u}}(s,P_{\mathrm{AsD}}^{\max}|\theta,z)\frac{1}{2\pi}f_{\mathcal{Z}_A}(z)\mathrm{d}\theta\mathrm{d}z, & \text{cond.6}\\ \\ \int_{h}^{\sqrt{h^2+R_2^2}}\int_{0}^{2\pi}p_{\mathrm{L}}\mathcal{L}_{I_{\mathrm{T}}^{u}}(s,\frac{\rho_{\mathrm{A}}}{\eta_{\mathrm{L}}}z^{\alpha_{\mathrm{L}}}|\theta,z)\frac{1}{2\pi}f_{\mathcal{Z}_A}(z)\mathrm{d}\theta\mathrm{d}z\\ +\int_{h}^{(\frac{P_{\mathrm{AsD}}^{\max}\eta_{\mathrm{N}}}{\rho_{\mathrm{A}}})^{\frac{1}{\alpha_{\mathrm{N}}}}}\int_{0}^{2\pi}p_{\mathrm{N}}\mathcal{L}_{I_{\mathrm{T}}^{u}}(s,\frac{\rho_{\mathrm{A}}}{\eta_{\mathrm{N}}}z^{\alpha_{\mathrm{N}}}|\theta,z)\frac{1}{2\pi}f_{\mathcal{Z}_A}(z)\mathrm{d}\theta\mathrm{d}z\\ +\int_{(\frac{P_{\mathrm{AsD}}^{\max}\eta_{\mathrm{N}}}{\rho_{\mathrm{A}}})^{\frac{1}{\alpha_{\mathrm{N}}}}}^{\sqrt{h^2+R_2^2}}\int_{0}^{2\pi}p_{\mathrm{N}}\mathcal{L}_{I_{\mathrm{T}}^{u}}(s,P_{\mathrm{AsD}}^{\max}|\theta,z)\frac{1}{2\pi}f_{\mathcal{Z}_A}(z)\mathrm{d}\theta\mathrm{d}z, & \text{cond.7 || cond.9}\\ \\ \int_{h}^{\sqrt{h^2+R_2^2}}\int_{0}^{2\pi}p_{\mathrm{L}}\mathcal{L}_{I_{\mathrm{T}}^{u}}(s,\frac{\rho_{\mathrm{A}}}{\eta_{\mathrm{L}}}z^{\alpha_{\mathrm{L}}}|\theta,z)\frac{1}{2\pi}f_{\mathcal{Z}_A}(z)\mathrm{d}\theta\mathrm{d}z\\ +\int_{h}^{\sqrt{h^2+R_2^2}}\int_{0}^{2\pi}p_{\mathrm{N}}\mathcal{L}_{I_{\mathrm{T}}^{u}}(s,\frac{\rho_{\mathrm{A}}}{\eta_{\mathrm{N}}}z^{\alpha_{\mathrm{N}}}|\theta,z)\frac{1}{2\pi}f_{\mathcal{Z}_A}(z)\mathrm{d}\theta\mathrm{d}z, & \text{cond.3N}\end{cases}, \quad (2.11)$$

where

$$\mathcal{L}_{I_{\mathrm{T}}^{u}}(s,p|\theta,z)=\frac{1}{1+\frac{sp}{\left(z^2-h^2+d^2-2\sqrt{z^2-h^2}d\cos(\theta)\right)^{\frac{\alpha_{\mathrm{T}}}{2}}}}, \tag{2.12}$$

conds.1k *and* 3k *is given in* (2.3) *and* (2.5) *respectively and the other conditions are given below:*

$$\text{cond.4}: \sqrt{\left(\frac{P_{\mathrm{AsD}}^{\max}\eta_{\mathrm{L}}}{\rho_{\mathrm{A}}}\right)^{\frac{2}{\alpha_{\mathrm{L}}}}-R_2^2}<\left(\frac{P_{\mathrm{AsD}}^{\max}\eta_{\mathrm{N}}}{\rho_{\mathrm{A}}}\right)^{\frac{1}{\alpha_{\mathrm{N}}}}<h<\left(\frac{P_{\mathrm{AsD}}^{\max}\eta_{\mathrm{L}}}{\rho_{\mathrm{A}}}\right)^{\frac{1}{\alpha_{\mathrm{L}}}}, \tag{2.13}$$

$$\text{cond.5}: \sqrt{\left(\frac{P_{\mathrm{AsD}}^{\max}\eta_{\mathrm{L}}}{\rho_{\mathrm{A}}}\right)^{\frac{2}{\alpha_{\mathrm{L}}}}-R_2^2}<h\leqslant\left(\frac{P_{\mathrm{AsD}}^{\max}\eta_{\mathrm{N}}}{\rho_{\mathrm{A}}}\right)^{\frac{1}{\alpha_{\mathrm{N}}}}, \tag{2.14}$$

$$\text{cond.6}: \left(\frac{P_{\mathrm{AsD}}^{\max}\eta_{\mathrm{N}}}{\rho_{\mathrm{A}}}\right)^{\frac{1}{\alpha_{\mathrm{N}}}}\leqslant h<\sqrt{\left(\frac{P_{\mathrm{AsD}}^{\max}\eta_{\mathrm{L}}}{\rho_{\mathrm{A}}}\right)^{\frac{2}{\alpha_{\mathrm{L}}}}-R_2^2}, \tag{2.15}$$

$$\text{cond.7}: \sqrt{\left(\frac{P_{\mathrm{AsD}}^{\max}\eta_{\mathrm{N}}}{\rho_{\mathrm{A}}}\right)^{\frac{2}{\alpha_{\mathrm{N}}}}-R_2^2}<h\leqslant\sqrt{\left(\frac{P_{\mathrm{AsD}}^{\max}\eta_{\mathrm{L}}}{\rho_{\mathrm{A}}}\right)^{\frac{2}{\alpha_{\mathrm{L}}}}-R_2^2}<\left(\frac{P_{\mathrm{AsD}}^{\max}\eta_{\mathrm{N}}}{\rho_{\mathrm{A}}}\right)^{\frac{1}{\alpha_{\mathrm{N}}}}, \tag{2.16}$$

$$\text{cond.8}: \left(\frac{P_{\mathrm{AsD}}^{\max}\eta_{\mathrm{N}}}{\rho_{\mathrm{A}}}\right)^{\frac{1}{\alpha_{\mathrm{N}}}}<\sqrt{\left(\frac{P_{\mathrm{AsD}}^{\max}\eta_{\mathrm{L}}}{\rho_{\mathrm{A}}}\right)^{\frac{2}{\alpha_{\mathrm{L}}}}-R_2^2}\leqslant h<\left(\frac{P_{\mathrm{AsD}}^{\max}\eta_{\mathrm{L}}}{\rho_{\mathrm{A}}}\right)^{\frac{1}{\alpha_{\mathrm{L}}}}, \tag{2.17}$$

$$\text{cond.9}: \sqrt{\left(\frac{P_{\mathrm{AsD}}^{\max}\eta_{\mathrm{N}}}{\rho_{\mathrm{A}}}\right)^{\frac{2}{\alpha_{\mathrm{N}}}}-R_2^2}<h<\left(\frac{P_{\mathrm{AsD}}^{\max}\eta_{\mathrm{N}}}{\rho_{\mathrm{A}}}\right)^{\frac{1}{\alpha_{\mathrm{N}}}}<\sqrt{\left(\frac{P_{\mathrm{AsD}}^{\max}\eta_{\mathrm{L}}}{\rho_{\mathrm{A}}}\right)^{\frac{2}{\alpha_{\mathrm{L}}}}-R_2^2}. \tag{2.18}$$

These conditions come from the fact that as the height of the ABS increases, the AsD is first under full channel inversion and then reaches its maximum power constraint. Depending on whether $\left(\frac{P_{\mathrm{AsD}}^{max}\eta_{\mathrm{N}}}{\rho_{\mathrm{A}}}\right)^{\frac{1}{\alpha_{\mathrm{N}}}}$ *is greater or smaller than* $\sqrt{\left(\frac{P_{\mathrm{AsD}}^{max}\eta_{\mathrm{L}}}{\rho_{\mathrm{A}}}\right)^{\frac{2}{\alpha_{\mathrm{L}}}}-R_2^2}$*, we can further specify conds. 1N, 2L, 2N and 3L as the conditions above.*

Proof: See Appendix A.1. ■

From Lemma 1, we can see that the transmit power of the AsD P_{AsD} and the distance between the AsD and the TBS d_A are related to the distance between the AsD and the ABS $\mathcal{Z}_A$. This important distance distribution is presented in the following lemma.

Lemma 2 *The probability density function (PDF) of the distance $\mathcal{Z}_A$ between the ABS at height h above the center of $\mathcal{S}_2$ and an i.u.d. AsD inside $\mathcal{S}_2$ is*

$$f_{\mathcal{Z}_A}(z) = \frac{2z}{R_2^2}, \quad h \leqslant z \leqslant \sqrt{R_2^2 + h^2}. \tag{2.19}$$

Proof: See Appendix A.2. ■

Theorem 1 *Based on the system model in Section 2.1, the uplink coverage probability of the TBS is*

$$\mathbb{P}_{\text{cov}}^{u,\text{T}} = \exp\left(-\frac{\gamma_{\text{T}}^u}{\rho_{\text{T}}}\sigma^2\right) \mathcal{L}_{I_{\text{T}}^u}(s), \tag{2.20}$$

where $I_{\text{T}}^u = P_{AsD} H_A^u d_A^{-\alpha_{\text{T}}}$, $s = \frac{\gamma_{\text{T}}^u}{\rho_{\text{T}}}$, and $\mathcal{L}_{I_{\text{T}}^u}(s)$ is given by Lemma 1.

Proof: From (2.6) and (2.10), we can have

$$\begin{aligned}
\mathbb{P}_{\text{cov}}^{u,\text{T}} &= \Pr(\mathsf{SINR}_{\text{T}}^u > \gamma_{\text{T}}^u) = \Pr\left(\frac{\rho_{\text{T}} H_T^u}{P_{\text{AsD}} H_A^u d_A^{-\alpha_{\text{T}}} + \sigma^2} > \gamma_{\text{T}}^u\right) \\
&= \Pr\left(H_T^u > \frac{\gamma_{\text{T}}^u}{\rho_{\text{T}}}(P_{\text{AsD}} H_A^u d_A^{-\alpha_{\text{T}}} + \sigma^2)\right) \\
&= \exp\left(-\frac{\gamma_{\text{T}}^u}{\rho_{\text{T}}}(P_{\text{AsD}} H_A^u d_A^{-\alpha_{\text{T}}} + \sigma^2)\right) \qquad (2.21a) \\
&= \exp\left(-\frac{\gamma_{\text{T}}^u}{\rho_{\text{T}}}\sigma^2\right) \exp\left(-\frac{\gamma_{\text{T}}^u}{\rho_{\text{T}}} P_{\text{AsD}} H_A^u d_A^{-\alpha_{\text{T}}}\right), \qquad (2.21b)
\end{aligned}$$

where (2.21a) follows from the fact that the link between the TsUE and the TBS experiences Rayleigh fading with a PDF of $f_{H_T^u}(h) = \exp(-h)$. Letting $I_{\text{T}}^u = P_{\text{AsD}} H_A^u d_A^{-\alpha_{\text{T}}}$ and $s = \frac{\gamma_{\text{T}}^u}{\rho_{\text{T}}}$ in (2.21b), we can arrive at Theorem 1. ■

Substituting (2.11) and (2.19) into (2.20), we can obtain the uplink coverage probability of the TBS.

2.2.2 ABS Uplink Coverage Probability

We begin by presenting three lemmas, which will then be used to compute the uplink coverage probability of the ABS in Theorem 2.

Lemma 3 *The Laplace transform of the interference power distribution at the ABS is*

$$\mathcal{L}_{I_{\mathrm{A}}^{u}}(s)=\int_{\sqrt{R_2^2+h^2}}^{\sqrt{(R_1-d)^2+h^2}}\int_0^{2\pi}\mathcal{L}_{I_{\mathrm{A}}^{u}}(s|\omega,z)f_{\Omega}(\omega|z)f_{\mathcal{Z}_T}(z)\mathrm{d}\omega\mathrm{d}z + \int_{\sqrt{(R_1-d)^2+h^2}}^{\sqrt{(R_1+d)^2+h^2}}\int_{-\widehat{\omega}}^{\widehat{\omega}}\mathcal{L}_{I_{\mathrm{A}}^{u}}(s|\omega,z)f_{\Omega}(\omega|z)f_{\mathcal{Z}_T}(z)\mathrm{d}\omega\mathrm{d}z, \tag{2.22}$$

where

$$\mathcal{L}_{I_{\mathrm{A}}^{u}}(s|\omega,z)=p_{\mathrm{L}}m_{\mathrm{L}}^{m_{\mathrm{L}}}\left(m_{\mathrm{L}}+s\rho_{\mathrm{T}}z^{-\alpha_{\mathrm{L}}}\eta_{\mathrm{L}}\left(z^2-h^2+d^2-2\sqrt{z^2-h^2}d\cos(\omega)\right)^{\frac{\alpha_{\mathrm{L}}}{2}}\right)^{-m_{\mathrm{L}}} + p_{\mathrm{N}}m_{\mathrm{N}}^{m_{\mathrm{N}}}\left(m_{\mathrm{N}}+s\rho_{\mathrm{T}}z^{-\alpha_{\mathrm{N}}}\eta_{\mathrm{N}}\left(z^2-h^2+d^2-2\sqrt{z^2-h^2}d\cos(\omega)\right)^{\frac{\alpha_{\mathrm{N}}}{2}}\right)^{-m_{\mathrm{N}}}, \tag{2.23}$$

and $\widehat{\omega}=\operatorname{arcsec}\left(\frac{2d\sqrt{z^2-h^2}}{d^2+z^2-h^2-R_1^2}\right)$.

Proof: See Appendix A.3. ■

The PDF of the distance between the TsUE and the ABS $f_{\mathcal{Z}_T}(z)$, and the conditional PDF of the angle, $f_{\Omega}(\omega|z)$, between the ground projection of $\mathcal{Z}_T$ and d_T are given in Lemma 4 and Lemma 5, respectively.

Lemma 4 *The PDF of the distance $\mathcal{Z}_T$ between the ABS at height h above the center of $\mathcal{S}_2$ and an i.u.d. TsUE inside $\mathcal{S}_1 \setminus \mathcal{S}_2$ is*

$$f_{\mathcal{Z}_T}(z)=\begin{cases}\frac{2z}{R_1^2-R_2^2}, & \sqrt{R_2^2+h^2}\leqslant z\leqslant\sqrt{(R_1-d)^2+h^2}\\ \frac{2z\widehat{\omega}}{\pi(R_1^2-R_2^2)}, & \sqrt{(R_1-d)^2+h^2}<z\leqslant\sqrt{(R_1+d)^2+h^2}\end{cases}. \tag{2.24}$$

Proof: See Appendix A.4. ■

Lemma 5 *The PDF of the angle, $f_{\Omega}(\omega|z)$, between the ground projection of $\mathcal{Z}_T$ and d_T conditioned on $\mathcal{Z}_T$ is*

$$f_{\Omega}(\omega|z)=\begin{cases}\frac{1}{2\pi}, & \sqrt{R_2^2+h^2}\leqslant z\leqslant\sqrt{(R_1-d)^2+h^2}\\ \frac{1}{2\widehat{\omega}}, & \sqrt{(R_1-d)^2+h^2}<z\leqslant\sqrt{(R_1+d)^2+h^2}\end{cases}. \tag{2.25}$$

Proof: This lemma can be proved by using cosine rule and simple trigonometry. ■

Theorem 2 *Based on the system model in Section 2.1, the uplink coverage probability of the ABS is given as*

$$\mathbb{P}_{\text{cov}}^{u,\text{A}} = \begin{cases} \int_h^{\sqrt{h^2+R_2^2}} \mathbb{P}_{\text{cov}}^{u,\text{L}}\left(P_{\text{AsD}}^{max}|z\right) f_{\mathcal{Z}_A}(z)\text{d}z \\ + \int_h^{\sqrt{h^2+R_2^2}} \mathbb{P}_{\text{cov}}^{u,\text{N}}\left(P_{\text{AsD}}^{max}|z\right) f_{\mathcal{Z}_A}(z)\text{d}z, & \text{cond.1L} \\ \\ \int_h^{\left(\frac{P_{\text{AsD}}^{max}\eta_{\text{L}}}{\rho_{\text{A}}}\right)^{\frac{1}{\alpha_{\text{L}}}}} \mathbb{P}_{\text{cov}}^{u,\text{L}}\left(\frac{\rho_{\text{A}}}{\eta_{\text{L}}} z^{\alpha_{\text{L}}}|z\right) f_{\mathcal{Z}_A}(z)\text{d}z \\ + \int_{\left(\frac{P_{\text{AsD}}^{max}}{\rho_{\text{A}}}\right)^{\frac{1}{\alpha_{\text{L}}}}}^{\sqrt{h^2+R_2^2}} \mathbb{P}_{\text{cov}}^{u,\text{L}}\left(P_{\text{AsD}}^{max}|z\right) f_{\mathcal{Z}_A}(z)\text{d}z \\ + \int_h^{\sqrt{h^2+R_2^2}} \mathbb{P}_{\text{cov}}^{u,\text{N}}\left(P_{\text{AsD}}^{max}|z\right) f_{\mathcal{Z}_A}(z)\text{d}z, & \text{cond.4 } || \text{ cond.8} \\ \\ \int_h^{\left(\frac{P_{\text{AsD}}^{max}\eta_{\text{L}}}{\rho_{\text{A}}}\right)^{\frac{1}{\alpha_{\text{L}}}}} \mathbb{P}_{\text{cov}}^{u,\text{L}}\left(\frac{\rho_{\text{A}}}{\eta_{\text{L}}} z^{\alpha_{\text{L}}}|z\right) f_{\mathcal{Z}_A}(z)\text{d}z \\ + \int_{\left(\frac{P_{\text{AsD}}^{max}}{\rho_{\text{A}}}\right)^{\frac{1}{\alpha_{\text{L}}}}}^{\sqrt{h^2+R_2^2}} \mathbb{P}_{\text{cov}}^{u,\text{L}}\left(P_{\text{AsD}}^{max}|z\right) f_{\mathcal{Z}_A}(z)\text{d}z \\ + \int_h^{\left(\frac{P_{\text{AsD}}^{max}\eta_{\text{N}}}{\rho_{\text{A}}}\right)^{\frac{1}{\alpha_{\text{N}}}}} \mathbb{P}_{\text{cov}}^{u,\text{N}}\left(\frac{\rho_{\text{A}}}{\eta_{\text{N}}} z^{\alpha_{\text{N}}}|z\right) f_{\mathcal{Z}_A}(z)\text{d}z \\ + \int_{\left(\frac{P_{\text{AsD}}^{max}}{\rho_{\text{A}}}\right)^{\frac{1}{\alpha_{\text{N}}}}}^{\sqrt{h^2+R_2^2}} \mathbb{P}_{\text{cov}}^{u,\text{N}}\left(P_{\text{AsD}}^{max}|z\right) f_{\mathcal{Z}_A}(z)\text{d}z, & \text{cond.5} \\ \\ \int_h^{\sqrt{h^2+R_2^2}} \mathbb{P}_{\text{cov}}^{u,\text{L}}\left(\frac{\rho_{\text{A}}}{\eta_{\text{L}}} z^{\alpha_{\text{L}}}|z\right) f_{\mathcal{Z}_A}(z)\text{d}z \\ + \int_h^{\sqrt{h^2+R_2^2}} \mathbb{P}_{\text{cov}}^{u,\text{N}}\left(P_{\text{AsD}}^{max}|z\right) f_{\mathcal{Z}_A}(z)\text{d}z, & \text{cond.6} \\ \\ \int_h^{\sqrt{h^2+R_2^2}} \mathbb{P}_{\text{cov}}^{u,\text{L}}\left(\frac{\rho_{\text{A}}}{\eta_{\text{L}}} z^{\alpha_{\text{L}}}|z\right) f_{\mathcal{Z}_A}(z)\text{d}z \\ + \int_h^{\left(\frac{P_{\text{AsD}}^{max}\eta_{\text{N}}}{\rho_{\text{A}}}\right)^{\frac{1}{\alpha_{\text{N}}}}} \mathbb{P}_{\text{cov}}^{u,\text{N}}\left(\frac{\rho_{\text{A}}}{\eta_{\text{N}}} z^{\alpha_{\text{N}}}|z\right) f_{\mathcal{Z}_A}(z)\text{d}z \\ + \int_{\left(\frac{P_{\text{AsD}}^{max}}{\rho_{\text{A}}}\right)^{\frac{1}{\alpha_{\text{N}}}}}^{\sqrt{h^2+R_2^2}} \mathbb{P}_{\text{cov}}^{u,\text{N}}\left(P_{\text{AsD}}^{max}|z\right) f_{\mathcal{Z}_A}(z)\text{d}z, & \text{cond.7 } || \text{ cond.9} \\ \\ \int_h^{\sqrt{h^2+R_2^2}} \mathbb{P}_{\text{cov}}^{u,\text{L}}\left(\frac{\rho_{\text{A}}}{\eta_{\text{L}}} z^{\alpha_{\text{L}}}|z\right) f_{\mathcal{Z}_A}(z)\text{d}z \\ + \int_h^{\sqrt{h^2+R_2^2}} \mathbb{P}_{\text{cov}}^{u,\text{N}}\left(\frac{\rho_{\text{A}}}{\eta_{\text{N}}} z^{\alpha_{\text{N}}}|z\right) f_{\mathcal{Z}_A}(z)\text{d}z, & \text{cond.3N} \end{cases}, \tag{2.26}$$

where

$$\mathbb{P}^{u,\mathrm{L}}_{\mathrm{cov}}(p|z) = \sum_{n=0}^{m_{\mathrm{L}}-1} \frac{(-s_1)^n}{n!} \exp(-s_1\sigma^2) \sum_{k=0}^{n} \binom{n}{k} (-\sigma^2)^{n-k} \frac{\mathrm{d}^k}{\mathrm{d}s_1^k} \mathcal{L}_{I^u_{\mathrm{A}}}(s_1) p_{\mathrm{L}}, \quad (2.27)$$

$s_1 = \frac{m_{\mathrm{L}} \gamma^u_{\mathrm{A}} z^{\alpha_{\mathrm{L}}}}{\eta_{\mathrm{L}} p}$ *and* $\mathcal{L}_{I^u_{\mathrm{A}}}(s_1)$ *is given by Lemma 3 and*

$$\mathbb{P}^{u,\mathrm{N}}_{\mathrm{cov}}(p|z) = \sum_{n=0}^{m_{\mathrm{N}}-1} \frac{(-s_2)^n}{n!} \exp(-s_2\sigma^2) \sum_{k=0}^{n} \binom{n}{k} (-\sigma^2)^{n-k} \frac{\mathrm{d}^k}{\mathrm{d}s_2^k} \mathcal{L}_{I^u_{\mathrm{A}}}(s_2) p_{\mathrm{N}}, \quad (2.28)$$

$s_2 = \frac{m_{\mathrm{N}} \gamma^u_{\mathrm{A}} z^{\alpha_{\mathrm{N}}}}{\eta_{\mathrm{N}} p}$ *and* $\mathcal{L}_{I^u_{\mathrm{A}}}(s_2)$ *is given by Lemma 3. The PDF of the distance between the AsD and the ABS* $f_{Z_A}(z)$ *is provided in Lemma 2.* conds.1k, 3k, *4–9 are given in* (2.3), (2.5) *and* (2.13)–(2.18). *These conditions come from the fact that the AsD is first under full channel inversion and then transmits with its maximum power as the height of the ABS increases. Note that we can further specify conds. 1N, 2L, 2N and 3L as conds. 4–9 depending on whether* $\left(\frac{P^{max}_{\mathrm{AsD}} \eta_{\mathrm{N}}}{\rho_{\mathrm{A}}}\right)^{\frac{1}{\alpha_{\mathrm{N}}}}$ *is larger or smaller than* $\sqrt{\left(\frac{P^{max}_{\mathrm{AsD}} \eta_{\mathrm{L}}}{\rho_{\mathrm{A}}}\right)^{\frac{2}{\alpha_{\mathrm{L}}}} - R_2^2}$.

Proof: See Appendix A.5. ■

Combining Lemma 3, 4, and 5 with Theorem 2, we can calculate the uplink coverage probability of the ABS.

2.3 Downlink Coverage Probability

In this section, we present the analytical framework to analyze the performance metric, the downlink coverage probability, which is formally defined as

$$\mathbb{P}^{d,b}_{\mathrm{cov}} \triangleq \Pr(\mathsf{SINR}^d_b > \gamma^d_b), \quad (2.29)$$

where superscript b is T for TsUE and A for AsD, and γ^d_b is the downlink SINR threshold. $\mathsf{SINR}^d_{\mathrm{T}}$ and $\mathsf{SINR}^d_{\mathrm{A}}$ can be found in (2.8) and (2.9), respectively. The next two subsections investigate the downlink coverage probability of the TsUE and the AsD.

2.3.1 TsUE Downlink Coverage Probability

First we present a lemma, which is used in deriving the coverage probability of the TsUE in Theorem 3

Lemma 6 *The conditional Laplace transform of the interference power distribution at the TsUE is*

$$\mathcal{L}_{I_{\mathrm{T}}^d}(s|z) = p_{\mathrm{L}} m_{\mathrm{L}}^{m_{\mathrm{L}}} \left(m_{\mathrm{L}} + sP_{\mathrm{ABS}}\eta_{\mathrm{L}} z^{-\alpha_{\mathrm{L}}}\right)^{-m_{\mathrm{L}}} + p_{\mathrm{N}} m_{\mathrm{N}}^{m_{\mathrm{N}}} \left(m_{\mathrm{N}} + sP_{\mathrm{ABS}}\eta_{\mathrm{N}} z^{-\alpha_{\mathrm{N}}}\right)^{-m_{\mathrm{N}}}. \tag{2.30}$$

Proof: The proof follows the same lines as Lemma 3 and is skipped for the sake of brevity. ■

Theorem 3 *Based on the system model in Section 2.1, the downlink coverage probability of the TsUE is given as*

$$\begin{aligned}\mathbb{P}_{\mathrm{cov}}^{d,\mathrm{T}} = &\int_{\sqrt{R_2^2+h^2}}^{\sqrt{(R_1-d)^2+h^2}} \int_0^{2\pi} \mathcal{L}_{I_{\mathrm{T}}^d}(s|z) \exp(-s\sigma^2) f_{\Omega}(\omega|z) f_{\mathcal{Z}_T}(z) \mathrm{d}\omega \mathrm{d}z \\ &+ \int_{\sqrt{(R_1-d)^2+h^2}}^{\sqrt{(R_1+d)^2+h^2}} \int_{-\widehat{\omega}}^{\widehat{\omega}} \mathcal{L}_{I_{\mathrm{T}}^d}(s|z) \exp(-s\sigma^2) f_{\Omega}(\omega|z) f_{\mathcal{Z}_T}(z) \mathrm{d}\omega \mathrm{d}z, \end{aligned} \tag{2.31}$$

where $s = \frac{\gamma_{\mathrm{T}}^d}{P_{\mathrm{TBS}}} \left(z^2 - h^2 + d^2 - 2\sqrt{z^2-h^2} d\cos(\omega)\right)^{\frac{\alpha_{\mathrm{T}}}{2}}$, $\mathcal{L}_{I_{\mathrm{T}}^d}(s|z)$ *is given by Lemma 6,* $f_{\Omega}(\omega|z)$ *is given by Lemma 5 and* $f_{\mathcal{Z}_T}(z)$ *is given by Lemma 4.*

Proof: Using the fact that the downlink fading power gain between the TBS and the TsUE H_T^d follows exponential distribution with unit mean and cosine rule, we can derive the TsUE downlink coverage probability. ■

2.3.2 AsD Downlink Coverage Probability

First we present a lemma, which is used in deriving the coverage probability of the AsD in Theorem 4

Lemma 7 *The conditional Laplace transform of the interference power distribution at the AsD is*

$$\mathcal{L}_{I_{\mathrm{A}}^d}(s|z,\theta) = \frac{1}{1 + \frac{sP_{\mathrm{TBS}}}{\left(z^2 - h^2 + d^2 - 2\sqrt{z^2-h^2} d\cos(\theta)\right)^{\frac{\alpha_{\mathrm{T}}}{2}}}}. \tag{2.32}$$

Proof: The proof follows the same lines as Lemma 1 and is skipped for the sake of brevity. ■

Theorem 4 *Based on the system model in Section 2.1, the downlink coverage probability of the AsD is given as*

$$\begin{aligned}\mathbb{P}_{\text{cov}}^{d,\text{A}} = &\int_h^{\sqrt{R_2^2+h^2}} \int_0^{2\pi} \sum_{n=0}^{m_{\text{L}}-1} \frac{(-s_1)^n}{n!} \exp(-s_1\sigma^2) \\ &\times \sum_{k=0}^{n} \binom{n}{k} (-\sigma^2)^{n-k} \frac{\mathrm{d}^k}{\mathrm{d}s_1^k} \mathcal{L}_{I_{\text{A}}^d}(s_1|z,\theta) p_{\text{L}} \frac{1}{2\pi} f_{\mathcal{Z}_A}(z) \mathrm{d}\theta \mathrm{d}z \\ &+ \int_h^{\sqrt{R_2^2+h^2}} \int_0^{2\pi} \sum_{n=0}^{m_{\text{N}}-1} \frac{(-s_2)^n}{n!} \exp(-s_2\sigma^2) \\ &\times \sum_{k=0}^{n} \binom{n}{k} (-\sigma^2)^{n-k} \frac{\mathrm{d}^k}{\mathrm{d}s_2^k} \mathcal{L}_{I_{\text{A}}^d}(s_2|z,\theta) p_{\text{N}} \frac{1}{2\pi} f_{\mathcal{Z}_A}(z) \mathrm{d}\theta \mathrm{d}z, \end{aligned} \tag{2.33}$$

where $s_1 = \frac{m_{\text{L}} \gamma_{\text{A}}^d z^{\alpha_{\text{L}}}}{P_{\text{ABS}} \eta_{\text{L}}}$, $s_2 = \frac{m_{\text{N}} \gamma_{\text{A}}^d z^{\alpha_{\text{N}}}}{P_{\text{ABS}} \eta_{\text{N}}}$, $\mathcal{L}_{I_{\text{A}}^d}(s|z,\theta)$ *is given by Lemma 7 and* $f_{\mathcal{Z}_A}(z)$ *is given by Lemma 2.*

Proof: The proof follows the same lines as Theorem 2 and is skipped for the sake of brevity. ■

2.4 Results

In this section, we first validate the analytical results and then discuss the design insights of an underlay drone system for IoT devices inside a stadium. The simulation results are generated using Matlab by averaging over 10^7 Monte Carlo simulation runs. Similar to [23, 34, 80], we set the path-loss exponents of LOS and NLOS aerial links as 2.5 and 4 respectively. Unless stated otherwise, the values of the parameters summarized in Table 2.1 are used.

2.4.1 Aerial Channel Model Parameter Values

Before presenting results to validate our analytical model, we first discuss about the ariel channel model. The probabilities of LOS and NLOS are functions of the environment, density and height of buildings, altitude of the drone and elevation angle between the drone and the devices on ground. There are two models commonly used

Table 2.1: Parameter Values.

Parameter	Value	Parameter	Value	Parameter	Value
R_1	500 m	α_{T}	4	ρ_{T}	-75 dBm
R_2	100 m	α_{L}	2.5	ρ_{A}	-50 dBm
d	200 m	α_{N}	4	$P_{\mathrm{AsD}}^{\max}$	20 dBm
m_{L}	5	γ_{A}^{u}	0 dB	P_{ABS}	20 dBm
m_{N}	1	γ_{T}^{u}	0 dB	P_{TBS}	40 dBm
η_{L}	0 dB	γ_{A}^{d}	0 dB	σ^2	-100 dBm
η_{N}	-20 dB	γ_{T}^{d}	0 dB		

Table 2.2: Aerial Channel Model Parameter Values [1, 2].

Model 1 Environment	Suburban	Urban	Dense Urban	High-rise Urban
Parameter (C_1, B_1)	(4.88, 0.43)	(9.6117, 0.1581)	(11.95, 0.136)	(27.23, 0.08)

in literature [1, 22], which are both based on the statistical parameters provided by the ITU-R.

Model 1: The LOS probability is given by

$$p_{\mathrm{L}} = \frac{1}{1 + C_1 \exp\left(-B_1\left[\frac{180}{\pi}\sin^{-1}\left(\frac{h}{z}\right) - C_1\right]\right)}. \tag{2.34}$$

The NLOS probability is

$$p_{\mathrm{N}} = 1 - p_{\mathrm{L}}, \tag{2.35}$$

where C_1 and B_1 are constant values that depend on the environment (suburban, urban, dense urban, high-rise urban) and typical values are listed in Table 2.2.

Model 2: The LOS probability is expressed as

$$p_{\mathrm{L}} = C_2\left(\frac{180}{\pi}\sin^{-1}\left(\frac{h}{z}\right) - 15\right)^{B_2}. \tag{2.36}$$

The NLOS probability is

$$p_{\mathrm{N}} = 1 - p_{\mathrm{L}}, \tag{2.37}$$

where C_2 and B_2 are environment dependent parameters. $C_2 = 0.6$ and $B_2 = 0.11$ for 2 GHz signal transmission in an urban environment [22].

Remark 1 *Both models above are focusing on the lower stratosphere (for drone altitude between 200 m and 3000 m). A broader aerial communication model that can fit for different operational environments (e.g., hill, sea, rural and urban areas) is still an open problem. The 3rd generation partnership project (3GPP) is actively engaged in developing a three-dimensional aerial channel model valid for drone altitude from 10 m to 300 m [81]. However, such a model is still under development and is currently not available. Thus, in the figures, we consider drone altitude between 200 m and 1000 m. However, it must be noted that current drone regulations generally limit drone height to below 150 m. The analytical framework proposed in this chapter is able to accommodate any aerial channel model for which the probabilistic functions of LOS and NLOS are given, such as Model 1 and 2.*

2.4.2 Coverage Probabilities

Figure 2.2 and Figure 2.3 plot the uplink coverage probability of the TBS and the ABS and the downlink coverage probability of the TsUE and the AsD against the ABS height respectively with Model 1 and Model 2 urban parameters. The analytical results are obtained using Theorem 1, Theorem 2, Theorem 3 and Theorem 4. In Figure 2.2(b), Figure 2.3(a) and Figure 2.3(b), two sets of simulation results are generated. One with Nakagami-m fading for the aerial channel model and one without small-scale fading. For the TBS uplink coverage probability, the simulation results match very well with the analytical results. For the ABS uplink coverage probability, the TsUE downlink coverage probability and the AsD downlink coverage probability, the analytical results agree with the simulation results with Nakagami-m fading and hold similar trends with the simulation results without small-scale fading. This validates the accuracy of our analytical framework.

Figure 2.2 and Figure 2.3 show almost the same trends for Model 1 and Model 2. Therefore, we focus on Model 1 for the results presented later in this chapter. Also we only show the numerical results in the later subsections, since the numerical results are verified by comparison with the simulation.

2.4.3 Impact of ABS Height

In Figure 2.4 and Figure 2.5, we investigate the effect of ABS height on the uplink coverage performance at the TBS and the ABS and the downlink coverage performance

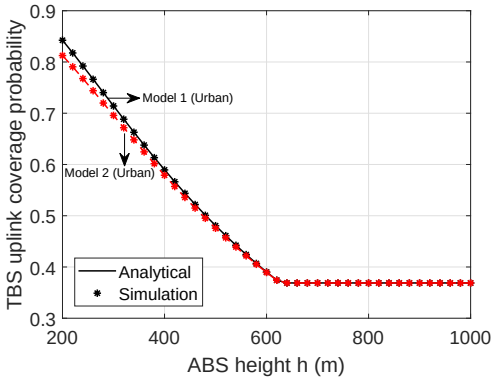

(a) TBS uplink coverage probability with different aerial channel models and simulations.

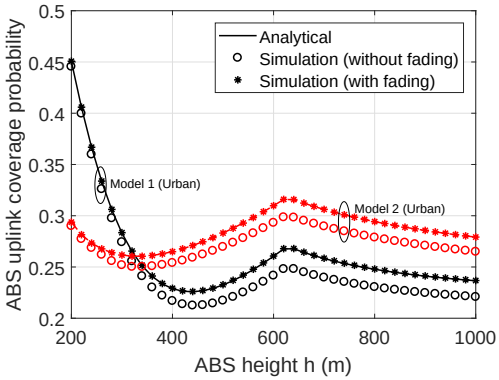

(b) ABS uplink coverage probability with different aerial channel models and simulations with and without Nakagami-m fading.

Figure 2.2: Uplink coverage probabilities versus height of ABS h with simulations.

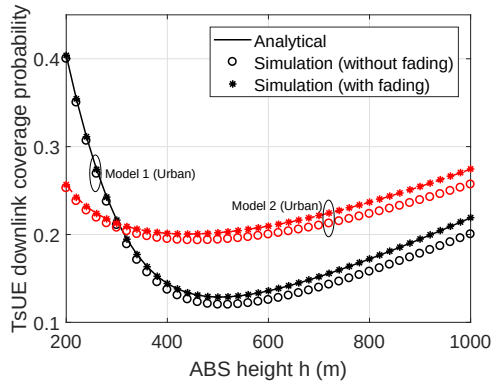

(a) TsUE downlink coverage probability with different aerial channel models and simulations with and without Nakagami-m fading.

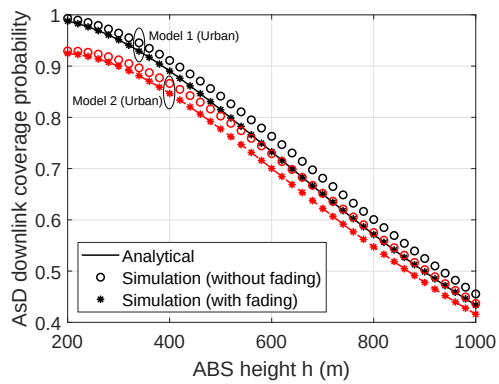

(b) AsD downlink coverage probability with different aerial channel models and simulations with and without Nakagami-m fading.

Figure 2.3: Downlink coverage probabilities versus height of ABS h with simulations.

at the TsUE and the AsD under different considered environments.

Insights: Figure 2.4(a) plots the uplink coverage probability of the TBS against the height of the ABS with different propagation environments (i.e., suburban, urban, dense urban and high-rise urban). From the figure, we can see that for most cases the uplink coverage probability of the TBS first decreases as the ABS height increases. This is because the transmit power of the AsD increases with the height of ABS, whereby the interference at the TBS increases. This decreases the coverage probability. After a certain ABS height, the coverage probability of the TBS stays as a

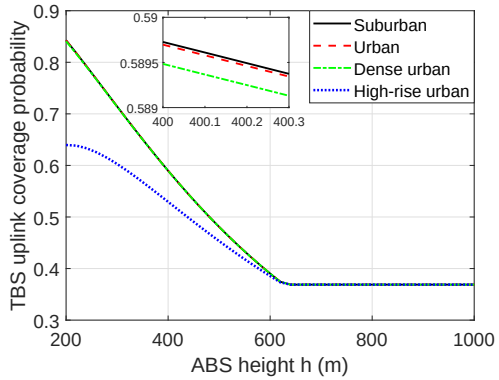

(a) TBS uplink coverage probability with different aerial channel environments.

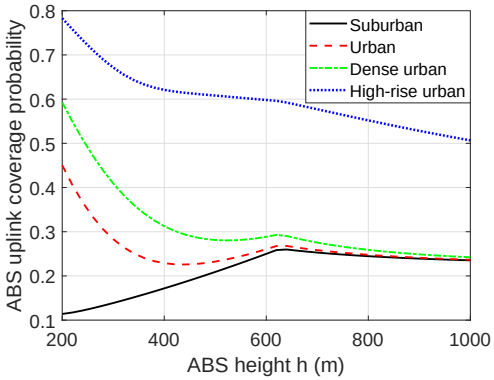

(b) ABS uplink coverage probability with different aerial channel environments.

Figure 2.4: Uplink coverage probabilities versus height of ABS h.

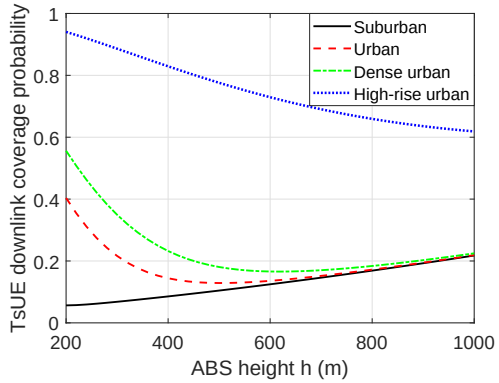

(a) TsUE downlink coverage probability with different aerial channel environments.

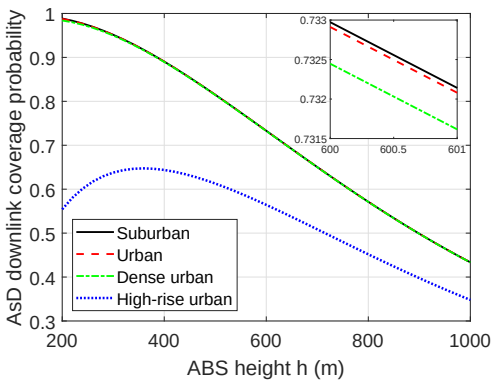

(b) AsD downlink coverage probability with different aerial channel environments.

Figure 2.5: Downlink coverage probabilities versus height of ABS h.

constant. This is due to the fact that the AsD has reached its maximum transmit power and the interference generated at the TBS keeps the same on average. Note that the height where the coverage probability of the TBS starts to level off is independent of the considered propagation environments.

Figure 2.4(b) plots the uplink coverage probability of the ABS against the height of the ABS with different considered environments in Table 2.2. For suburban environment, the ABS uplink coverage probability first increases and then decreases with the ABS height. In contrast, the ABS uplink coverage probability first decreases as the ABS height increases, then increases to its local maximum for other propagation environments. Thereafter it decreases again as the ABS height further increases. When

the ABS height is low, there is higher probability that the interference link between TsUE and ABS is in LOS as the height of ABS rises. Therefore, the ABS uplink coverage probability drops. As the height increases further, the interference link is highly likely in LOS, but the interference power drops and the average desired signal power received at the ABS stays the same under full channel inversion. Hence, the coverage probability increases. When the ABS height is above the global/local optimal height (depends on considered propagation environments), the AsD transmits with its maximum power $P_{\text{AsD}}^{\max}$ and the received power of the desired signal reduces as the height increases further. This leads to the drop of the uplink coverage probability at the ABS.

Figure 2.5(a) shows the downlink coverage probability of the TsUE versus the height of the ABS with different propagation environments in Table 2.2. The TsUE downlink coverage probability increases with the ABS height for suburban environment, but decreases for high-rise urban environment. For the other environments, the TsUE downlink coverage probability decreases with the increased ABS height and then increases as the ABS height further increases. When the ABS height increases, the interference link between TsUE and ABS has a higher chance of being in LOS, but the three-dimensional propagation distance and the path-loss also increases. This interplay leads to the above mentioned trends.

From Figure 2.5(b), we can see that the AsD downlink coverage probability first increases and then decreases as the ABS height increases in high-rise urban environment. For the other environments, the downlink coverage probability of the AsD drops with the increase in the height of ABS. Unlike uplink power control, the ABS transmits with a constant power for downlink communication. Therefore, the received power of the desired signal at the AsD reduces as the height increases and so does the AsD downlink coverage probability.

2.4.4 Impact of Environment

Insights: From Figure 2.4 and Figure 2.5, we can also see that different propagation environments heavily impact the network performance. Figure 2.4(a) shows that the TBS uplink coverage probability is ordered from highest to lowest as follows: suburban, urban, dense urban and high-rise urban when the ABS height is low. Figure 2.4(b) illustrates that the ABS uplink coverage probability is ordered from highest to lowest as follows: high-rise urban, dense urban, urban and suburban. This is because building blockage is severe for dense urban and high-rise urban environment. Therefore, the

path-loss between the ABS and the TsUE and between the ABS and the AsD is strong. The received interference power at the ABS from the TsUE is less. The AsD however needs to transmit with a higher power to overcome the path-loss, thus generates a higher interference power for the TBS.

The TsUE downlink coverage probability is ordered from highest to lowest as follows: high-rise urban, dense urban, urban and suburban in Figure 2.5(a), but the AsD downlink coverage probability is lowest for high-rise urban environment in Figure 2.5(b). The severe building blockage in the dense urban and high-rise urban environment reduces the received interfering power at the TsUE from the ABS and the received power of the desired signal at the AsD from the ABS.

These figures reveal that the height of the ABS and the propagation environment affect the network performance. In the next subsection, we are going to find the ABS heights which maximize TBS uplink coverage probability, ABS uplink coverage probability, TsUE downlink coverage probability and AsD downlink coverage probability under different propagation environments and how the optimal heights of ABS change with the distance between the center of the stadium and the TBS d in the next section.

2.4.5 Impact of Distance Between Center of Stadium and TBS

Figure 2.6(a), Figure 2.6(b), Figure 2.7(a) and Figure 2.7(b) plot the maximum uplink coverage probability at the TBS, the maximum uplink coverage probability at the ABS, the maximum downlink coverage probability at the TsUE and the maximum downlink coverage probability at the AsD against the distance between the center of the stadium and the TBS d with the corresponding ABS heights marked, respectively, for different propagation environment parameters.

Insights: From the figures, we can see that both the uplink and downlink network performance improve when the distance between the center of the stadium and the TBS d increases. This is because, the interference experienced at the drone cell and the terrestrial cell decreases, when the two cells are further apart.

From Figure 2.6(a), we can see that for most cases, the uplink coverage probability at the TBS is maximized when the ABS is placed as low as possible (which is 200 m for the aerial channel model considered). The optimal ABS height which maximizes the TBS uplink coverage probability increases with the distance between the center of the stadium and the TBS d for high-rise urban environment. If we refer to Figure 2.4(a), we can see that the TBS uplink coverage probability for high-rise urban environment

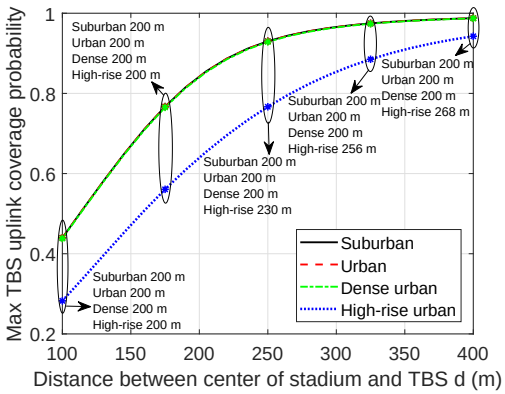

(a) Maximum TBS uplink coverage probability with different aerial channel environments.

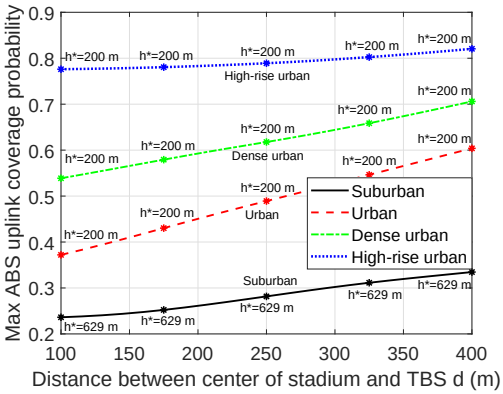

(b) Maximum ABS uplink coverage probability with different aerial channel environments.

Figure 2.6: Maximum uplink coverage probabilities versus distance between the center of the stadium and the TBS d.

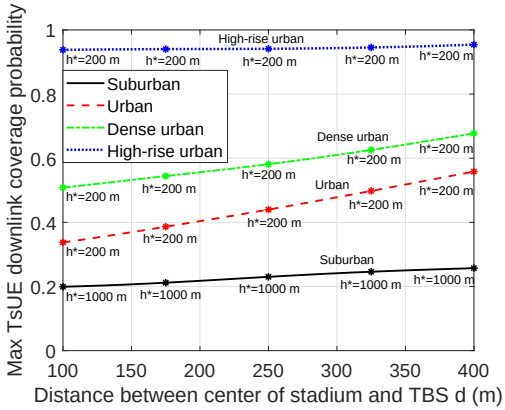

(a) Maximum TsUE downlink coverage probability with different aerial channel environments.

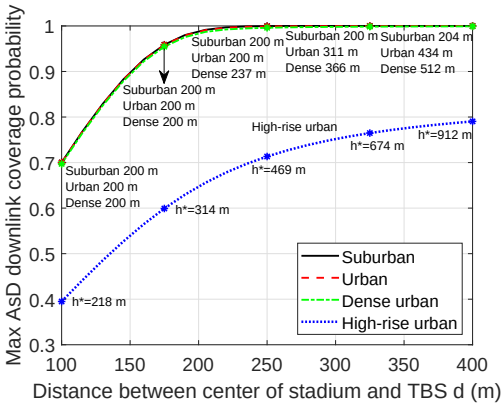

(b) Maximum AsD downlink coverage probability with different aerial channel environments.

Figure 2.7: Maximum downlink coverage probabilities versus distance between the center of the stadium and the TBS d.

increases a little before dropping to a constant level. When d increases, the drop starts at a higher ABS altitude.

Figure 2.6(b) shows that the uplink coverage probability at the ABS is maximized when the ABS is placed as low as possible (i.e., 200 m) for urban, dense urban and high-rise urban environments and at 629 m for suburban environment. Referring to Figure 2.4(b), the global maximum of ABS uplink coverage probability exists at 629 m for suburban environment, and at a lower altitude for other environments. The optimal ABS height is independent to the distance between the center of the stadium

and the TBS.

Figure 2.7(a) illustrates that the TsUE downlink coverage probability is maximized when the ABS is placed as low as possible (i.e., 200 m) for urban, dense urban and high-rise urban environments, but as high as possible (i.e., 1000 m) for the suburban environments. As shown in Figure 2.5(a), the TsUE downlink coverage probability increases with the ABS height for the suburban environment, but decreases for high-rise urban environment. For other environments, the maximum TsUE downlink coverage probability can be found at 200 m, even though the downlink coverage probability increases when the ABS height further increases. The optimal height of ABS is independent to the distance between the center of the stadium and the TBS.

Figure 2.7(b) shows that the height of ABS which maximizes the AsD downlink coverage probability increases with the distance between the center of the stadium and the TBS d. From Figure 2.5(b), we can see that the AsD downlink coverage probability first increases and then decreases as the ABS height increases. When d increases, the drop starts at a higher ABS altitude.

From Figure 2.6 and Figure 2.7, we can find that the uplink coverage probabilities at the TBS and the ABS and the downlink coverage probability at the TsUE are maximized when the ABS is deployed at 200 m for urban environment and dense urban environment. Although the maximum AsD downlink coverage probability is not achieved with an ABS height of 200 m and a large distance d, the downlink coverage probability at the AsD is much higher than the one at the TsUE for urban environment and dense urban environment. *Therefore, it is best to place the ABS at a low height (e.g., 200 m or lower) for urban environment and dense urban environment regardless of the distance between the center of the stadium and the TBS d. In contrast, the ABS should be placed at different heights depending on the distance between the center of the stadium and the TBS d and the task of the system (i.e., prioritize the terrestrial link or the aerial link, prioritize the uplink or the downlink communication) for suburban environment and high-rise urban environment.*

2.5 Summary

In this chapter, a two-cell network with a TBS and an underlay ABS for IoT device coverage in temporary events was considered. We presented a general analytical framework for uplink coverage probability of the TBS and the ABS and downlink

coverage probability of the TsUE and the AsD in terms of the Laplace transforms of the interference power distribution and the distance distribution between the ABS and an i.u.d. AsD and between the ABS and an i.u.d. TsUE. The framework is able to accommodate any aerial channel model. The simulation results confirmed the accuracy of the proposed model. The results have shown that the ABS is best to be deployed at 200 m or lower for urban environment and dense urban environment regardless of the distance between the center of the stadium and the TBS.

Chapter 3

Drone-Assisted Multihop Multicast Device-to-Device Networks for Emergency Information Dissemination

In Chapter 2, we have investigated the use of underlay drone cell to provide coverage for a temporary event in a stadium. In this chapter, we analyze another use case for drone in wireless network, which is emergency information dissemination in public safety scenarios. We consider a drone-assisted multihop multicast D2D network where a drone is deployed to broadcast an emergency alert message to all terrestrial D2D users at the first time slot. After that, the drone leaves and the D2D users that have successfully received the message become the active TXs for the next time slots. Using stochastic geometry, we propose a general analytical framework to compute the link coverage probability and the mean local delay for a D2D user and the network coverage probability. The framework is able to accommodate any aerial channel model for which the probabilistic functions of LOS and NLOS links are specified. The Monte Carlo simulation results confirm the accuracy of the proposed model. Our results reveal the impacts of the different system parameters (i.e., height and transmit power of the drone and density and sensitivity radius of the D2D users) on the link performance and the network performance.

This chapter is organized as follows: Section 3.1 describes the system model and assumptions. Section 3.2 focuses on the link performance of a D2D user. Section 3.3 details the analysis of the network coverage probability. Section 3.4 presents the results and the effect of the system parameters on the link performance and the network performance. Finally, Section 3.5 summarizes the chapter.

3.1 System Model

We consider a drone-assisted multihop multicast D2D network, in which an emergency alert message needs to be conveyed to all terrestrial D2D users under a public safety scenario. The terrestrial D2D users are assumed to be uniformly distributed over a disk network region $|\mathcal{S}|$ with radius R_C, i.e., $|\mathcal{S}| = \pi R_C^2$ and their locations form a finite Poisson point process (PPP) ϕ with density λ. Throughout the chapter, we use X_i to denote both the random location as well as the ith D2D user itself. We assume that the cellular network is unavailable or not operational, for instance, due to a natural disaster. So a drone is deployed at a height of h above the center of the network region and broadcasts an emergency alert message. Then the drone flies out of the network region to broadcast the emergency alert message in other areas and the terrestrial users multicast the emergency alert message to each others using D2D links. In this chapter, we focus our analysis on one terrestrial cell without inter terrestrial cell interference. This is based on the assumption that the terrestrial adjacent cells use different frequencies. Hence, the interference from far away cells becomes negligible and can be ignored [39, 76].

3.1.1 Channel Model

There are two types of communication links in the considered system model: aerial links and terrestrial links. The link between the D2D users are terrestrial links. The link between the drone and the D2D users are aerial links.

Terrestrial links: A general power-law path-loss model is considered for terrestrial links, in which the signal power decays at a rate $\ell^{-\alpha_T}$ with the propagation distance ℓ and α_T is the path-loss exponent. Furthermore, we assume the terrestrial links experience independent small-scale Rayleigh fading and AWGN with variance σ^2.

Aerial links: The channel characteristics of the aerial links (or known as air-to-ground links) are significantly different from the terrestrial links. Depending on altitude and type of the drone, elevation angle and type of propagation environment, the aerial links can be either LOS or NLOS with different probabilities of occurrence p_L and p_N [22].

The path-loss of the NLOS aerial link is greater than the LOS one, because of the shadowing effect and the reflection of signals from obstacles. Following [31], the

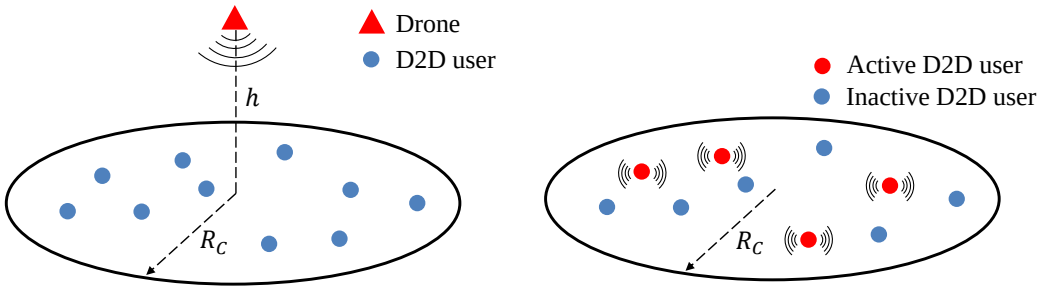

(a) Drone broadcasting phase: First time slot T_0.

(b) D2D multicasting phase: Second time slot onwards $T_n, n = 1, 2, 3 \cdots$.

Figure 3.1: Illustration of the multihop multicast system model.

path-loss of the aerial link is modeled as

$$PL_a(z) = \begin{cases} \eta_{\mathrm{L}} z^{-\alpha_{\mathrm{L}}}, & \text{LOS} \\ \eta_{\mathrm{N}} z^{-\alpha_{\mathrm{N}}}, & \text{NLOS} \end{cases}, \tag{3.1}$$

where z is the three-dimensional propagation distance between the drone and the D2D user, α_{L} and α_{N} is the path-loss exponent of LOS aerial link and NLOS aerial link respectively, η_{L} and η_{N} is the additional attenuation factor for LOS aerial link and NLOS aerial link respectively and $\eta_{\mathrm{L}} > \eta_{\mathrm{N}}$.

Similar to Chapter 2, the small-scale fading of the aerial link is modeled as Nakagami-m fading in this chapter. The fading parameter for the LOS aerial link and NLOS aerial link is denoted by m_{L} and m_{N} respectively and $m_{\mathrm{L}} > m_{\mathrm{N}}$. The aerial links also experience AWGN with variance σ^2.

3.1.2 Transmission Model

For the considered multihop multicast transmission scheme, time is slotted and the emergency alert message is delivered slot by slot to the D2D users on the ground through two phases, as shown in Figure 3.1.

Drone broadcasting phase: In the first time slot T_0, the drone broadcasts an emergency alert message to all terrestrial D2D users. At the end of the first time slot, terrestrial D2D users attempt to decode the message. User X_i decodes successfully if and only if the received signal-to-noise ratio (SNR) is greater than a threshold γ. The

instantaneous SNR at the D2D user at the first time slot T_0 is given as

$$\mathsf{SNR}_0 = \frac{P_{\mathrm{A}} G PL_a(\mathcal{Z})}{\sigma^2}, \tag{3.2}$$

where P_{A} is the transmit power of the drone. G is the aerial link fading power gain, which follows Gamma distribution. $\mathcal{Z}$ is the Euclidean distance between the drone and the terrestrial D2D user. The path-loss of the aerial link $PL_a(\cdot)$ is given in (3.1).

D2D multicasting phase: From the second time slot onwards, all D2D users that have successfully received the emergency alert message in the previous time slot become the active TXs and multicast the common message for the current time slot. Since the emergency alert message is a common message for all the terrestrial D2D users, there is no mutual interference between the D2D transmissions. The inactive D2D user is able to receive the aggregate signal from all the active neighbor D2D TXs within its sensitivity region with radius R_D. As before, user X_j decodes the non-coherent sum of message successfully and becomes active at the end of the current time slot if the received SNR is above the threshold γ. The delivery of the emergency alert message by the multihop multicast scheme proceeds slot by slot in this way (for time slots $T_n, n \neq 0$). Furthermore, we assume that mutual synchronization among the terrestrial D2D users is achieved by distributed synchronization algorithm and the terrestrial D2D users are static during the whole transmission [82, 83, 84].

SNR is an important measure that affects the state of the D2D user, whether being active (acting as a TX) or inactive (acting as a RX). For the considered setup, the instantaneous SNR at the inactive D2D user at the later time slots $T_n, n \neq 0$ is shown as

$$\mathsf{SNR}_n = \frac{P_{\mathrm{D}} \sum_{X_i \in \phi_{\text{active}}} H_i \ell_i^{-\alpha_{\mathrm{T}}}}{\sigma^2}, \quad n \neq 0, \tag{3.3}$$

where P_{D} is the transmit power of the active D2D users. H_i is the fading power gain between the inactive D2D user and the ith active D2D TX within its sensitivity region, which follows exponential distribution. The fading power gain H_i is assumed to be independent during successive time slots. ℓ_i is the Euclidean distance between the inactive D2D user and the ith active D2D TX within its sensitivity region.

3.2 Link Performance

In this section, we provide the mathematical formulations to analyze the link performance at the given D2D user, which incorporate the analysis of both phases. We are interested in the following two performance metrics that directly reflect the perceived experience of D2D users:

- *Link coverage probability after time slot T_n, $\mathbb{P}^n_{\text{cov}}(X_i)$:* The link coverage probability after time slot T_n measures the probability that the specific D2D user X_i has successfully received the message after the given time slot.

- *Mean local delay, $\overline{D}(X_i)$:* The local delay is defined as the number of transmission attempts needed until the first success of message transmission. The mean local delay characterizes that the specific D2D user X_i successfully receives the message after $\overline{D}(X_i)$ time slots on average.

Before calculating these two metrics, we need to first look at the link success probability at each time slot which is defined as follows:

Definition 1 *The link success probability at time slot T_n is the probability that the received SNR at the D2D user X_i is higher than the threshold γ. It can be expressed as*

$$\mathbb{P}^n_s(X_i) \triangleq \Pr(\mathsf{SNR}_n > \gamma). \tag{3.4}$$

Theorem 5 *Based on the system model in Section 3.1, the link success probability at the first time slot T_0 is given as*

$$\begin{aligned}\mathbb{P}^0_s(X_i) = &\sum_{i=0}^{m_{\text{L}}-1} \frac{p_{\text{L}}}{i!} \left(\frac{m_{\text{L}}\gamma\sigma^2 z_i^{\alpha_{\text{L}}}}{P_{\text{A}}\eta_{\text{L}}}\right)^i \exp\left(-\frac{m_{\text{L}}\gamma\sigma^2 z_i^{\alpha_{\text{L}}}}{P_{\text{A}}\eta_{\text{L}}}\right) \\ &+ \sum_{j=0}^{m_{\text{N}}-1} \frac{p_{\text{N}}}{j!} \left(\frac{m_{\text{N}}\gamma\sigma^2 z_i^{\alpha_{\text{N}}}}{P_{\text{A}}\eta_{\text{N}}}\right)^j \exp\left(-\frac{m_{\text{N}}\gamma\sigma^2 z_i^{\alpha_{\text{N}}}}{P_{\text{A}}\eta_{\text{N}}}\right),\end{aligned} \tag{3.5}$$

where $z_i = \sqrt{X_i^2 + h^2}$.

Proof: From (3.2) and (3.4), we have

$$\begin{aligned}\mathbb{P}_s^0(X_i) &= \Pr(\mathsf{SNR}_0 > \gamma) = \Pr\left(\frac{P_{\mathrm{A}} G P L_a(\mathcal{Z})}{\sigma^2} > \gamma\right) \\ &= \Pr\left(G > \frac{\gamma\sigma^2}{P_{\mathrm{A}} P L_a(\mathcal{Z})}\right) \\ &= \sum_{i=0}^{m_{\mathrm{L}}-1} \frac{p_{\mathrm{L}}}{i!}\left(\frac{m_{\mathrm{L}}\gamma\sigma^2 z_i^{\alpha_{\mathrm{L}}}}{P_{\mathrm{A}}\eta_{\mathrm{L}}}\right)^i \exp\left(-\frac{m_{\mathrm{L}}\gamma\sigma^2 z_i^{\alpha_{\mathrm{L}}}}{P_{\mathrm{A}}\eta_{\mathrm{L}}}\right) \\ &+ \sum_{j=0}^{m_{\mathrm{N}}-1} \frac{p_{\mathrm{N}}}{j!}\left(\frac{m_{\mathrm{N}}\gamma\sigma^2 z_i^{\alpha_{\mathrm{N}}}}{P_{\mathrm{A}}\eta_{\mathrm{N}}}\right)^j \exp\left(-\frac{m_{\mathrm{N}}\gamma\sigma^2 z_i^{\alpha_{\mathrm{N}}}}{P_{\mathrm{A}}\eta_{\mathrm{N}}}\right), \end{aligned} \tag{3.6}$$

where (3.6) comes from the fact that G follows Gamma distribution with parameter m_{L} and m_{N} for LOS and NLOS aerial link respectively and we can arrive at Theorem 5. ■

After the first time slot T_0, the drone leaves the network region and all D2D users that have successfully received the emergency alert message become the TXs and multicast the message. However, the network will be in outage if none of the D2D users has successfully received the message from the drone at the first time slot T_0.

Theorem 6 *Based on the system model in Section 3.1, the network outage probability at the first time slot T_0 is given as*

$$\begin{aligned}\mathbb{P}_{\mathrm{out}} = \exp\Bigg(-\int_h^{\sqrt{R_{\mathrm{C}}^2+h^2}} \Bigg(&\sum_{i=0}^{m_{\mathrm{L}}-1} \frac{p_{\mathrm{L}}}{i!}\left(\frac{m_{\mathrm{L}}\gamma\sigma^2 z^{\alpha_{\mathrm{L}}}}{P_{\mathrm{A}}\eta_{\mathrm{L}}}\right)^i \exp\left(-\frac{m_{\mathrm{L}}\gamma\sigma^2 z^{\alpha_{\mathrm{L}}}}{P_{\mathrm{A}}\eta_{\mathrm{L}}}\right) \\ &+ \sum_{j=0}^{m_{\mathrm{N}}-1} \frac{p_{\mathrm{N}}}{j!}\left(\frac{m_{\mathrm{N}}\gamma\sigma^2 z^{\alpha_{\mathrm{N}}}}{P_{\mathrm{A}}\eta_{\mathrm{N}}}\right)^j \exp\left(-\frac{m_{\mathrm{N}}\gamma\sigma^2 z^{\alpha_{\mathrm{N}}}}{P_{\mathrm{A}}\eta_{\mathrm{N}}}\right)\Bigg) 2\pi\lambda z \mathrm{d}z\Bigg). \end{aligned} \tag{3.7}$$

Proof: The network will be in outage if none of the D2D users has successfully received the message from the drone at the first time slot T_0. From Theorem 5, we have

$$\mathbb{P}_{\mathrm{out}} = \mathbb{E}_\phi\left[\prod_{x\in\phi}\left(1-\mathbb{P}_s^0(x)\right)\right] = \exp\left(-\int_0^{R_{\mathrm{C}}} \mathbb{P}_s^0(x) 2\pi\lambda x \mathrm{d}x\right) \tag{3.8a}$$

$$= \exp\left(-\int_h^{\sqrt{R_{\mathrm{C}}^2+h^2}} \mathbb{P}_s^0(\sqrt{z^2-h^2}) 2\pi\lambda z \mathrm{d}z\right), \tag{3.8b}$$

where (3.8a) follows from the probability generating functional for PPP. Substituting (3.5) into (3.8b), we can arrive at Theorem 6. ■

Now let us assume there is at least one active D2D user broadcasting the message at time slot T_n for $n \neq 0$, the inactive D2D user receives the message from all the active TXs within its sensitivity region. The following remark discusses the challenges and proposes solution for modeling the locations of the active D2D TXs.

Remark 2 *After the first time slot T_0, the D2D users closer to the drone have higher chances to become active than the ones further away from the drone. Therefore, the positions of the active TXs within the sensitivity region of a D2D user X_i are inhomogeneous with more active TXs located closer to the center of the network region. Moreover, the locations of the active TXs at the current time slot is correlated with their locations in the previous time slots. However, it is very difficult to identify and fit a spatial point process for the location of the active TXs inside the sensitivity region. Hence, for analytical tractability, we propose to model the active TXs inside the D2D user X_i's sensitivity region at time slot T_n as an independent homogeneous PPP. At time slot T_1, the active TXs inside the D2D user X_i's sensitivity region have a density of $\lambda_i^1 = \mathbb{P}_s^0(X_i)\lambda$. The accumulated density of the active TXs inside the D2D user X_i's sensitivity region at time slot T_n for $n = 2, 3, 4...$ is $\lambda_i^n = (\mathbb{P}_s^0(X_i) + \sum_{k=1}^{n-1} \mathbb{P}_s^k(X_i)(1 - \mathbb{P}_{\text{out}}) \prod_{l=0}^{k-1}(1 - \mathbb{P}_s^l(X_i)))\lambda$. The accuracy of this approximation will be validated in Section 3.4.*

In this chapter, we adopt a numerical inversion method, which is easy to compute and also provides controllable error estimation [85, 86]. By numerically inverting the Laplace transform of the aggregate received signal power via a trapezoidal summation, we can express the link success probability of D2D user X_i at time slot T_n for $n \neq 0$ as below

$$\mathbb{P}_s^n(X_i) = 1 - \frac{2^{-B} P_{\text{D}} \exp(\frac{A}{2})}{\gamma \sigma^2} \sum_{b=0}^{B} \binom{B}{b} \sum_{c=0}^{C+b} \frac{(-1)^c}{D_c} \text{Re}\left[\frac{\mathcal{L}_{P_i^n}(s)}{s}\right], \tag{3.9}$$

where $\text{Re}[\cdot]$ is the real part operator, $s = \frac{(A + j2\pi c)P_{\text{D}}}{2\gamma\sigma^2}$, $\mathcal{L}_{P_i^n}(s)$ is the Laplace transform of the aggregate received signal power at the user X_i, $P_i^n = \sum_{X_j \in \phi_{\text{active}}} H_j \ell_j^{-\alpha_{\text{T}}}$, $D_c = 2$ (if $c = 0$) and $D_c = 1$ (if $c = 1, 2, ..., C + b$). A, B and C are positive parameters used to control the estimation accuracy.

From (3.9), the key parameter in order to obtain the link success probability at time

slot T_n for D2D user X_i is $\mathcal{L}_{P_i^n}(s)$. By the definition of Laplace transform of a random variable, we can express $\mathcal{L}_{P_i^n}(s)$ in the following theorem.

Theorem 7 *Following the system model in Section 3.1, the Laplace transform of the aggregate received signal power at the D2D user X_i from all the active TXs inside its sensitivity region is*

$$\mathcal{L}_{P_i^n}(s)=\begin{cases}\exp\left(-\pi\lambda_i^n R_D^2\left(1-\frac{2R_D^{\alpha_T}}{s(\alpha_T+2)}\,{}_2F_1\left(1,1+\frac{2}{\alpha_T};2+\frac{2}{\alpha_T};-\frac{R_D^{\alpha_T}}{s}\right)\right)\right), & X_i\leqslant R_C-R_D\\ \exp\left(-\pi\lambda_i^n (R_C-X_i)^2\left(1-\frac{2(R_C-X_i)^{\alpha_T}}{s(\alpha_T+2)}\,{}_2F_1\left(1,1+\frac{2}{\alpha_T};2+\frac{2}{\alpha_T};-\frac{(R_C-X_i)^{\alpha_T}}{s}\right)\right)\right) & \\ \times\exp\left(-\int_{R_C-X_i}^{R_D}\frac{2s\lambda_i^n\ell}{\ell^{\alpha_T}+s}\text{arcsec}\left(\frac{2\ell X_i}{\ell^2+X_i^2-R_C^2}\right)\mathrm{d}\ell\right), & R_C-R_D<X_i\leqslant R_C\end{cases}, \tag{3.10}$$

where ${}_2F_1(\cdot,\cdot;\cdot;\cdot)$ is the Gaussian (or ordinary) hypergeometric function.

Proof: See Appendix B.1. ■

Although the Laplace transform of the aggregate received signal power at the D2D user X_i for $R_C-R_D<X_i\leqslant R_C$ cannot be expressed in close-form due to complexity of the inverse trigonometric functions which is inside the integration. However, it can be easily evaluated numerically using Mathematica.

Recall that the link coverage probability after time slot T_n, $\mathbb{P}_{\text{cov}}^n(X_i)$ is defined as the probability that the D2D user X_i has successfully received the message after $n+1$ time slots, which is shown as follows:

Proposition 1 *Based on the system model in Section 3.1 and the definition of the link coverage probability after time slot T_n, we have*

$$\mathbb{P}_{\text{cov}}^n(X_i)=\begin{cases}\mathbb{P}_s^0(X_i), & n=0\\ \mathbb{P}_s^0(X_i)+\sum_{k=1}^n\mathbb{P}_s^k(X_i)(1-\mathbb{P}_{\text{out}})\prod_{l=0}^{k-1}(1-\mathbb{P}_s^l(X_i)), & n=1,2,3...\end{cases}, \tag{3.11}$$

where $\mathbb{P}_s^0(X_i)$ is given in Theorem 5 and $\mathbb{P}_s^k(X_i)$ for $k\neq 0$ is given in (3.9). *$\mathbb{P}_{\text{out}}$ is shown in Theorem 6.*

We now turn to the delay metric. For the considered drone-assisted multihop multicast network, the local delay at the D2D user X_i is a discrete random variable with a

probability mass function (PMF) as follows:

$$\Pr(D(X_i)=d)=\begin{cases}\mathbb{P}_s^0(X_i), & d=1\\ \mathbb{P}_s^{d-1}(X_i)(1-\mathbb{P}_{\text{out}})\prod_{l=0}^{d-2}(1-\mathbb{P}_s^l(X_i)), & d=2,3,4...\end{cases}. \quad (3.12)$$

Hence the mean local delay is given by $\overline{D}(X_i)=\mathbb{E}[D(X_i)]=\sum_{d=1}^{\infty} d\Pr(D(X_i)=d)$ and the specific expression of the mean local delay is shown in the following proposition.

Proposition 2 *Based on the system model in Section 3.1, the mean local delay at the D2D user X_i is given as*

$$\overline{D}(X_i)=\mathbb{P}_s^0(X_i)+\sum_{d=2}^{\infty} d\mathbb{P}_s^{d-1}(X_i)(1-\mathbb{P}_{\text{out}})\prod_{l=0}^{d-2}(1-\mathbb{P}_s^l(X_i)), \quad (3.13)$$

where $\mathbb{P}_s^0(X_i)$ is given in Theorem 5 and $\mathbb{P}_s^n(X_i)$ for $n\neq 0$ is given in (3.9). *$\mathbb{P}_{\text{out}}$ is shown in Theorem 6.*

3.3 Network Performance

In the previous section, we have focused on the link performance where the distance between the D2D user and the ground projection of the drone is known. Now we turn to study the network performance charaterized by the network coverage probability after time slot T_n. $\mathbb{P}_{\text{cov}}^n$ measures the average probability that a randomly chosen D2D user in the network has successfully received the message after time slot T_n, in other words, it presents the fraction of active D2D TXs in the network after the given time slot.

Before looking into the network coverage probability, we first investigate the network success probability at time slot T_n. To evaluate the network success probability, we need to calculate the expectancy of the link success probability over the spatial distribution of the distance between a D2D user and the ground projection of the drone.

The expression of the network success probability is shown below:

$$\mathbb{P}_s^n = \begin{cases} \int_h^{\sqrt{R_C^2+h^2}} \frac{2z}{R_C^2} \sum_{i=0}^{m_L-1} \frac{p_L}{i!} \left(\frac{m_L \gamma \sigma^2 z^{\alpha_L}}{P_A \eta_L}\right)^i \exp\left(-\frac{m_L \gamma \sigma^2 z^{\alpha_L}}{P_A \eta_L}\right) \mathrm{d}z \\ + \int_h^{\sqrt{R_C^2+h^2}} \frac{2z}{R_C^2} \sum_{j=0}^{m_N-1} \frac{p_N}{j!} \left(\frac{m_N \gamma \sigma^2 z^{\alpha_N}}{P_A \eta_N}\right)^j \exp\left(-\frac{m_N \gamma \sigma^2 z^{\alpha_N}}{P_A \eta_N}\right) \mathrm{d}z, \quad n=0 \\ 1 - \frac{2^{-B} P_D \exp(\frac{A}{2})}{\gamma \sigma^2} \sum_{b=0}^{B} \binom{B}{b} \sum_{c=0}^{C+b} \frac{(-1)^c}{D_c} \mathrm{Re}\left[s^{-1} \int_h^{\sqrt{R_C^2+h^2}} \frac{2z}{R_C^2} \mathcal{L}_{P_i^n}(s) \mathrm{d}z \right], \quad n=1,2,3... \end{cases} \tag{3.14}$$

where $s = \frac{(A+j2\pi c)P_D}{2\gamma\sigma^2}$, the Laplace transform of the aggregate received signal power $\mathcal{L}_{P_i^n}(s)$ is given in Theorem 7, $D_c = 2$ (if $c = 0$) and $D_c = 1$ (if $c = 1, 2, ..., C+b$).

Remark 3 *To the best of our knowledge, it is not easy to evaluate the integration* $\int_h^{\sqrt{R_C^2+h^2}} \frac{2z}{R_C^2} \mathcal{L}_{P_i^n}(s) \mathrm{d}z$ *due to the non-closed-form Laplace transform. We propose to make a simplification assumption that, from the second time slot onwards, a D2D user will become active if there is one or more active TXs multicasting the message within its sensitivity region. We show that this approximation allows tractable computation of the network success probability at time slot* T_n *for* $n \neq 0$*. Our results in Section 3.4 show that a good level of accuracy is obtained with this approximation.*

Lemma 8 *Following the system model in Section 3.1, the approximated link success probability for D2D user* X_i *at time slot* T_n *for* $n = 1, 2, 3...$ *is given as*

$$\widetilde{\mathbb{P}_s^n}(X_i) = \begin{cases} 1 - \exp(-\lambda_i^n R_D^2 \pi), & X_i \leqslant R_C - R_D \\ 1 - \exp\left(\lambda_i^n R_D^2 \left(\arccos\left(\frac{R_C^2 - X_i^2 - R_D^2}{2X_i R_D}\right) - \pi \right) - \lambda_i^n R_C^2 \arccos\left(\frac{R_C^2 + X_i^2 - R_D^2}{2X_i R_C}\right) \right. & \\ \left. + \frac{\lambda_i^n}{2} \sqrt{-R_C^4 - R_D^4 - X_i^4 + 2R_C^2 X_i^2 + 2R_D^2 X_i^2 + 2R_C^2 R_D^2} \right), & R_C - R_D < X_i \leqslant R_C \end{cases} \tag{3.15}$$

where $\lambda_i^n = (\mathbb{P}_s^0(X_i) + \sum_{k=1}^{n-1} \widetilde{\mathbb{P}_s^k}(X_i)(1 - \mathbb{P}_{\text{out}}) \prod_{l=0}^{k-1} (1 - \widetilde{\mathbb{P}_s^l}(X_i)))\lambda$.

Proof: See Appendix B.2. ■

Using the approximated link success probability above, we can express the approx-

Table 3.1: Summary of the Analytical Model for Drone-assisted Multihop Multicast D2D Networks.

Performance metrics	General form	Key factor(s)
Link coverage probability	Proposition 1	$\mathbb{P}_s^0(X_i)$ in (3.5) $\mathbb{P}_{\text{out}}$ in (3.7) $\mathbb{P}_s^n(X_i)$ for $n \neq 0$ in (3.9)
Mean local delay	Proposition 2	$\mathbb{P}_s^0(X_i)$ in (3.5) $\mathbb{P}_{\text{out}}$ in (3.7) $\mathbb{P}_s^n(X_i)$ for $n \neq 0$ in (3.9)
Network coverage probability	Proposition 3	$\mathbb{P}_{\text{out}}$ in (3.7) $\mathbb{P}_s^0$ in (3.14) $\widetilde{\mathbb{P}_s^n}$ in (3.16)

imated network success probability at time slot T_n for $n = 1, 2, 3...$ as below:

$$\widetilde{\mathbb{P}_s^n} = \int_0^{R_C - R_D} \frac{2x}{R_C^2} - \frac{2x}{R_C^2} \exp(-\lambda_i^n R_D^2 \pi) \mathrm{d}x + \int_{R_C - R_D}^{R_C} \frac{2x}{R_C^2} \left(1 - \exp\left(\lambda_i^n R_D^2 \left(\arccos\left(\frac{R_C^2 - x^2 - R_D^2}{2xR_D}\right) - \pi\right) - \lambda_i^n R_C^2 \arccos\left(\frac{R_C^2 + x^2 - R_D^2}{2xR_C}\right) + \frac{\lambda_i^n}{2}\sqrt{-R_C^4 - R_D^4 - x^4 + 2R_C^2x^2 + 2R_D^2x^2 + 2R_C^2R_D^2}\right)\right) \mathrm{d}x, \tag{3.16}$$

where $\lambda_i^n = (\mathbb{P}_s^0(X_i) + \sum_{k=1}^{n-1} \widetilde{\mathbb{P}_s^k}(X_i)(1 - \mathbb{P}_{\text{out}}) \prod_{l=0}^{k-1}(1 - \widetilde{\mathbb{P}_s^l}(X_i)))\lambda$.

Proposition 3 *Based on the system model in Section 3.1, the network coverage probability after time slot T_n is given as*

$$\mathbb{P}_{\text{cov}}^n = \begin{cases} \mathbb{P}_s^0, & n = 0 \\ \mathbb{P}_s^0 + \widetilde{\mathbb{P}_s^1}(1 - \mathbb{P}_{\text{out}})(1 - \mathbb{P}_s^0), & n = 1 \\ \mathbb{P}_s^0 + \widetilde{\mathbb{P}_s^1}(1 - \mathbb{P}_{\text{out}})(1 - \mathbb{P}_s^0) + \sum_{k=2}^{n} \widetilde{\mathbb{P}_s^k}(1 - \mathbb{P}_{\text{out}})(1 - \mathbb{P}_s^0) \prod_{l=1}^{k-1}(1 - \widetilde{\mathbb{P}_s^l}), & n = 2, 3... \end{cases} \tag{3.17}$$

where $\mathbb{P}_s^0$ is given in (3.14) *and $\widetilde{\mathbb{P}_s^k}$ is given in* (3.16). *$\mathbb{P}_{\text{out}}$ is shown in Theorem 6.*

The key performance metrics are summarized in Table 3.1.

Table 3.2: Parameter Values.

Parameter	Value	Parameter	Value	Parameter	Value
R_D	75 m	α_{T}	4	λ	50 /km^2
R_C	2000 m	α_{L}	2.5	γ	0 dBm
h	200 m	α_{N}	4	P_{A}	25 dBm
m_{L}	5	η_{L}	0 dB	P_{D}	10 dBm
m_{N}	1	η_{N}	-20 dB	σ^2	-100 dBm

3.4 Results

In this section, we first validate the analytical results of both the link performance and the network performance and then discuss the design insights of a drone-assisted multihop multicast D2D network. The simulation results are generated using Matlab by averaging over 10^6 Monte Carlo simulation runs. We set $A = 24$, $B = 20$ and $C = 30$ in order to achieve an estimation error of 10^{-10}. Unless stated otherwise, the values of the other parameters summarized in Table 3.2 are used.

To generate the results in this section, we adopt a widely used aerial channel model [2, 22, 87]. The LOS probability is given as $p_{\mathrm{L}} = \frac{1}{1+C_a \exp\left(-B_a\left[\frac{180}{\pi}\sin^{-1}\left(\frac{h}{z}\right)-C_a\right]\right)}$ and the NLOS probability is $p_{\mathrm{N}} = 1 - p_{\mathrm{L}}$. $C_a = 9.6117$ and $B_a = 0.1581$ for signal transmission in an urban environment. Note that the analytical framework proposed in this chapter is able to accommodate any aerial channel model for which the probabilistic functions of LOS and NLOS are provided.

3.4.1 Link Coverage Probability

Figure 3.2(a) and Figure 3.2(b) plot the link coverage probability of a D2D user after the first time slot T_0, $\mathbb{P}^0_{\mathrm{cov}}(X_i)$, and after time slot T_5, $\mathbb{P}^5_{\mathrm{cov}}(X_i)$, against its distance from the ground projection of the drone with different transmit power of the drone respectively. The analytical results are obtained using Proposition 1. For both link coverage probabilities, the simulation results match very well with the analytical results. This validates the accuracy of our analytical framework.

From Figure 3.2(b), we can see that the link coverage probability at the D2D user close to the ground projection of the drone is very closed to 1 after time slot T_5. Therefore, we focus on the link coverage probability at the cell edge D2D user, i.e., user located at 2 km from the ground projection of the drone. In the results presented later in this chapter, we investigate the effect of some important system parameters, the

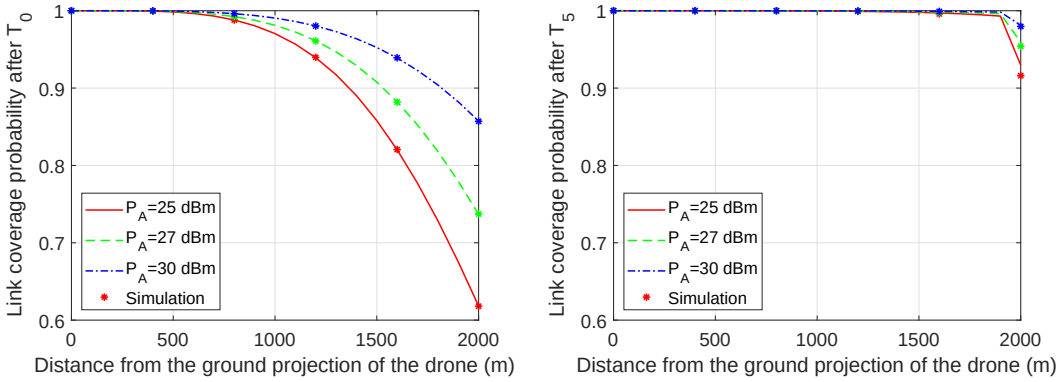

(a) Link coverage probability after the first time slot T_0 with different transmit power of the drone and simulations.

(b) Link coverage probability after time slot T_5 with different transmit power of the drone and simulations.

Figure 3.2: Link coverage probabilities versus the distance of D2D user from the ground projection of the drone with simulations.

transmit power and the height of the drone and the density and the sensitivity radius of the D2D users, on the link coverage probability of the cell edge user.

3.4.2 Impact of Drone Transmit Power

Figure 3.3(a) plots the link coverage probability after time slot T_n at the cell edge user located at 2 km from the ground projection of the drone for different drone transmit power with simulations. Figure 3.3(b) shows the mean local delay of a D2D user against its distance from the ground projection of the drone with different transmit power of the drone and simulations. Figure 3.3(c) illustrates the network coverage probability after time slot T_n for different transmit power of the drone with simulations.

From Figures 3.3(a) and 3.3(b), we can see that our analytical results for link performance provide a good approximation to the simulation. The small gap between them comes from two reasons: (i) ignorance of the inhomogeneity of the active TXs inside the D2D user's sensitivity region, and (ii) ignorance of the correlation between the locations of active D2D TXs across different time slots, as discussed in Remark 2. From the figures, we can see that the gap between the simulation and the analytical results is small which validates the independent homogeneous PPP assumption. Figure 3.3(c) also shows that the approximation we made in Remark 3 in the analysis of the network performance provides good accuracy. We only show the numerical results in the later subsections, since the numerical results are verified by comparison with the

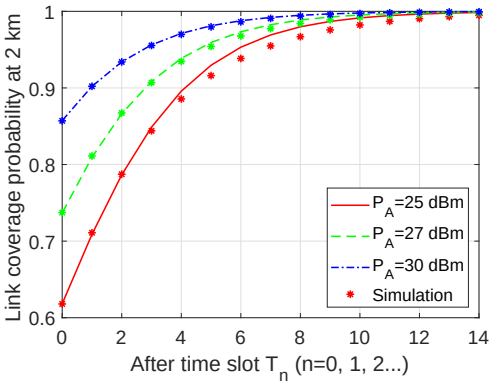

(a) Link coverage probability after time slot T_n at the cell edge user located at 2 km from the ground projection of the drone.

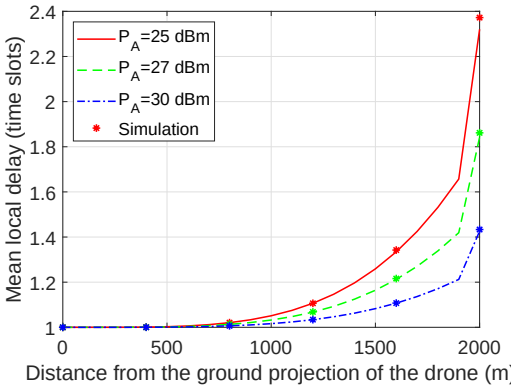

(b) Mean local delay of a D2D user versus its distance from the ground projection of the drone.

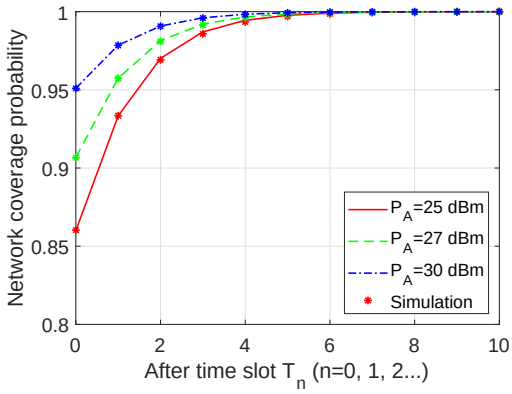

(c) Network coverage probability after time slot T_n.

Figure 3.3: Link performance and network performance with different transmit power of the drone and simulations.

simulation.

Insights: Figure 3.3(a) shows that the increase in the drone transmit power improves the link coverage probability of the cell edge user. With a higher transmit power of the drone, the link coverage probability of the cell edge user approaches 1 faster. From Figure 3.3(b), we can see that the benefit of increasing transmit power of the drone is more significant for the D2D users further away from the ground projection of the drone than for the ones closer to the ground projection of the drone. Figure 3.3(c) illustrates that a higher drone transmit power provides a higher network coverage probability. With a higher transmit power of the drone, the network coverage probability approaches 1 using less time slots. This is because that more D2D users

successfully receive the message after the first time slot T_0 if the drone broadcasts with a higher transmit power. Therefore, there are more active D2D users which multicast the message from the second time slot T_1 onwards and the message spreads over the network region more quickly.

3.4.3 Impact of Drone Height

In Figure 3.4(a), Figure 3.4(b) and Figure 3.4(c), we investigate the effect of deployment height of the drone on the link coverage probability at the cell edge user, the mean local delay of a D2D user and the network coverage probability after time slot T_n respectively.

The aerial channel model we adopted in this section is for low altitude aerial platform with an altitude between 200 m and 3000 m. In the figures shown, we consider drone altitude between 200 m and 1000 m. However, it must be noted that current drone regulations generally limit drone height to below 150 m. This is expected to change in the future.

Insights: Figure 3.4(a) shows the link coverage probability after time slot T_n at the cell edge user located at 2 km from the ground projection of the drone for different drone height. From this figure, we can see that the link coverage probability of the cell edge user after certain time slots is higher if the drone is deployed at a higher altitude at the first time slot T_0. With a higher altitude of the drone, the link coverage probability of the cell edge user approaches 1 after less time slots. Figure 3.4(b) plots the mean local delay of a D2D user against its distance from the ground projection of the drone with different height of the drone. The figure shows that the increase of the deployment height of the drone decreases the mean local delay more significantly for the D2D users further away from the ground projection of the drone than for the ones closer to the ground projection of the drone. Although the signal propagates a longer distance as the height of the drone rises, there is higher probability that the link between the drone and the user around the cell edge is in LOS and experiences a lower path-loss.

Figure 3.4(c) illustrates the network coverage probability after time slot T_n for different deployment height of the drone. From the figure, we can find that a higher drone altitude provides a higher network coverage probability. The network coverage probability approaches 1 using less time slots when the drone is initially positioned at a higher height. This is because, if the drone is at a higher altitude, more D2D users

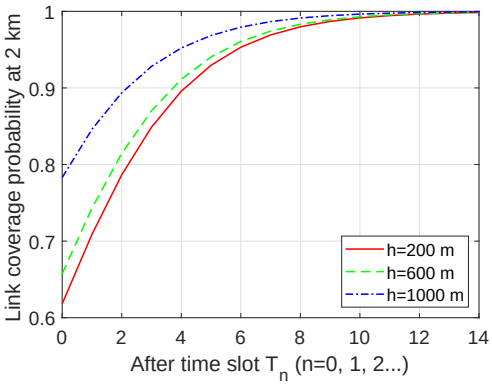

(a) Link coverage probability after time slot T_n at the cell edge user located at 2 km from the ground projection of the drone.

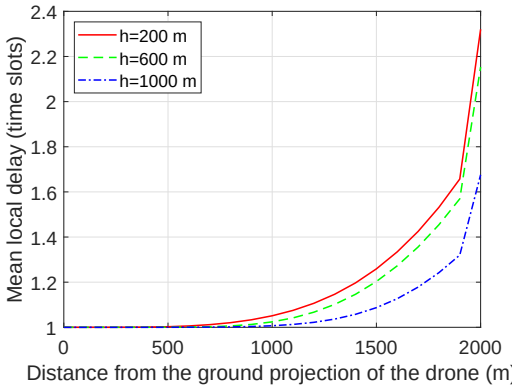

(b) Mean local delay of a D2D user versus its distance from the ground projection of the drone.

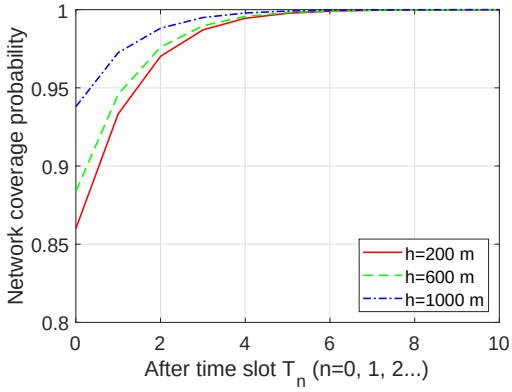

(c) Network coverage probability after time slot T_n.

Figure 3.4: Link performance and network performance with different height of the drone.

around the cell edge receive the message and become active TX after the first time slot T_0 and the message spreads over the network region faster.

3.4.4 Impact of D2D User Density

We study the impact of the density of D2D users on the link coverage probability at the cell edge user, the mean local delay of a D2D user and the network coverage probability after time slot T_n in Figure 3.5(a), Figure 3.5(b) and Figure 3.5(c) respectively.

Insights: Figure 3.5(a) illustrates the link coverage probability after time slot T_n at the cell edge user located at 2 km from the ground projection of the drone for different D2D user density. Figure 3.5(b) plots the mean local delay of a D2D user against

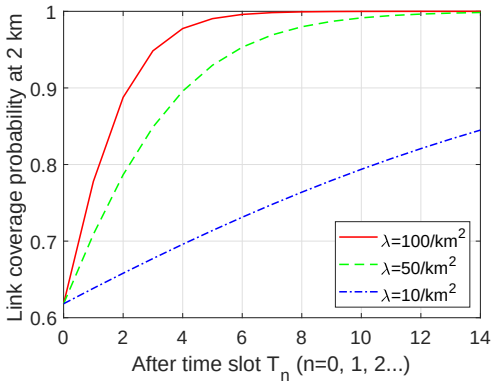

(a) Link coverage probability after time slot T_n at the cell edge user located at 2 km from the ground projection of the drone.

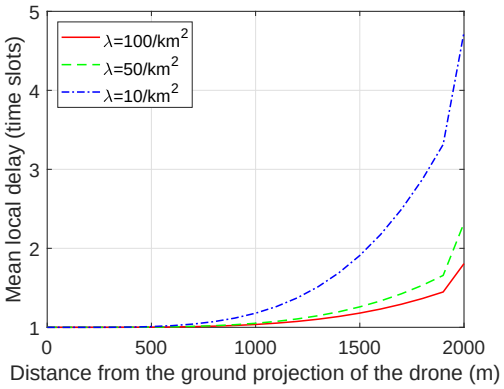

(b) Mean local delay of a D2D user versus its distance from the ground projection of the drone.

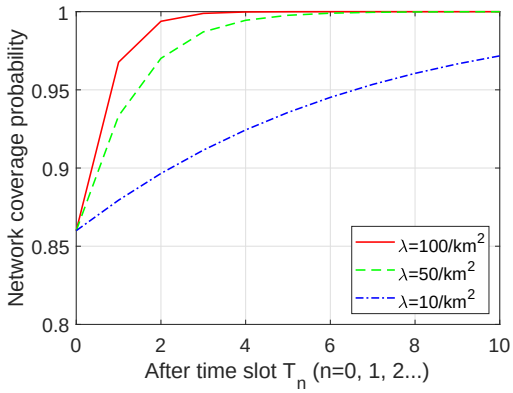

(c) Network coverage probability after time slot T_n.

Figure 3.5: Link performance and network performance with different D2D user density.

its distance from the ground projection of the drone with various D2D user density. Figure 3.5(c) shows the network coverage probability after time slot T_n for different density of D2D users.

From Figure 3.5(a) and Figure 3.5(c), we can see that after a given number of time slots, the link coverage probability of the cell edge user and the network coverage probability are higher if the D2D user density is higher. Figure 3.5(b) demonstrates that the mean local delay of a D2D user at 2 km from the ground projection of the drone decreases from 4.736 time slots to 1.806 time slots, when the density of the D2D users increases from 10 per km^2 to 100 per km^2. With a higher density of D2D users, there are more D2D users in the cell that have received the message successfully

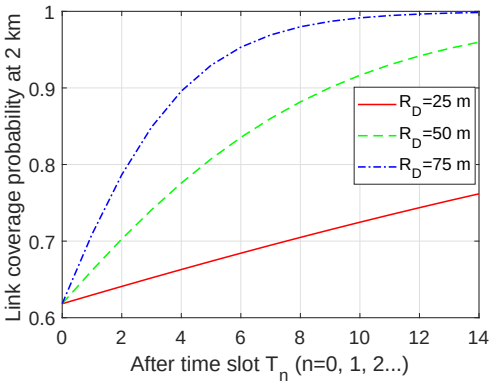

(a) Link coverage probability after time slot T_n at the cell edge user located at 2 km from the ground projection of the drone.

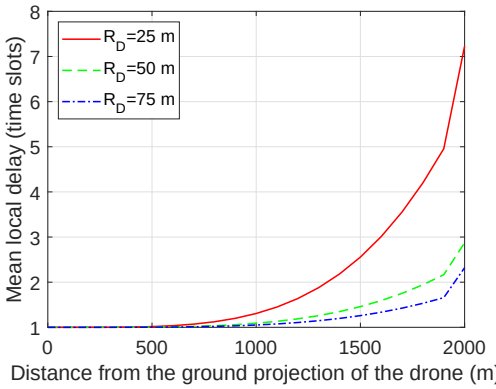

(b) Mean local delay of a D2D user versus its distance from the ground projection of the drone.

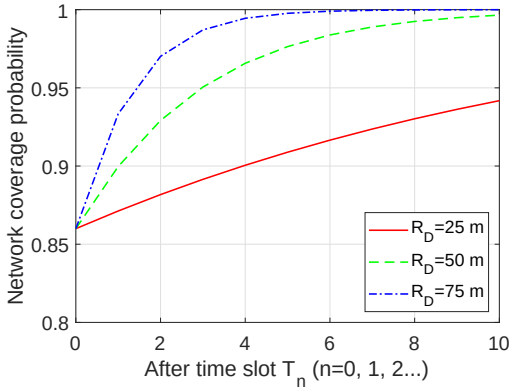

(c) Network coverage probability after time slot T_n.

Figure 3.6: Link performance and network performance with different D2D sensitivity radius.

and more active TXs located inside the D2D user's sensitivity region. So the message is delivered to the cell edge user within fewer time slots.

3.4.5 Impact of D2D Sensitivity Radius

In Figure 3.6(a), Figure 3.6(b) and Figure 3.6(c), we evaluate the effect of the radius of D2D sensitivity region on the link coverage probability at the cell edge user after time slot T_n, the mean local delay of a D2D user and the network coverage probability after time slot T_n respectively.

Insights: Figures 3.6(a) and 3.6(c) show the link coverage probability at the cell edge user located at 2 km from the ground projection of the drone and the network

coverage probability after time slot T_n for different radius of D2D sensitivity region. From these two figures, we can find that the link coverage probability of the cell edge user and the network coverage probability after a given number of time slots are higher if the D2D sensitivity region has a larger radius. This is because, there are more active TXs located inside the D2D user's sensitivity region if the radius is higher.

Figure 3.6(b) plots the mean local delay of a D2D user versus its distance from the ground projection of the drone with different radius of D2D sensitivity region. The figure shows that the increase of D2D sensitivity radius drops the mean local delay more significantly for the D2D users further away from the ground projection of the drone than for the ones closer to the ground projection of the drone. This is because, with a larger D2D sensitivity radius, the message multicasted by the active TXs located closer to the ground projection of the drone reaches the cell edge user within fewer hops.

3.5 Summary

In this chapter, we considered a drone-assisted multihop multicast D2D network in public safety scenarios, where an emergency alert message is broadcasted by the drone and then multicasted by the D2D users which have successfully received the message through multihop. A general analytical framework for link coverage probability and mean local delay for a D2D user was presented in terms of the link success probability, the network outage probability and the Laplace transform of the aggregate received signal power. An approximate and yet accurate analytical model was proposed for link success probability, network success probability and network coverage probability. Our frameworks are valid for any aerial channel model. The accuracy of the analytical results was verified by simulations. The results showed that the link performance and the network performance improve by raising the deployment altitude and the transmit power of the drone and increasing the density and the sensitivity radius of the D2D users.

Chapter 4

Characterization of Aggregate Received Power from Power Beacons in Millimeter Wave Ad Hoc Networks

WPT has emerged as an attractive solution to power future wireless communication networks. Deployment of low cost PBs is a promising technique for dedicated WPT in beyond 5G networks. In this chapter, we consider WPT using PBs for a mmWave wireless ad hoc network. Using stochastic geometry, we derive the MGF and the nth cumulant of the aggregate received power from PBs at a reference RX in closed-form. The MGF allows the CCDF of the aggregate received power from PBs to be numerically evaluated. We also compare different closed-form distributions which can be used to approximate the CCDF of the aggregate received power. Our results show that the lognormal distribution provides the best CCDF approximation compared to other distributions considered in the literature. The results also show that under practical setups, it is feasible to power users in a mmWave ad hoc network using PBs.

This chapter is organized as follows: Section 4.1 describes the system model in detail. The MGF and the nth cumulant of the aggregate received power are derived in Section 4.2. The distributions used to approximate the CCDF of the aggregate received power are presented in Section 4.2.3. The analytical and simulation results are shown in Section 4.3. Finally, the chapter is summarized in Section 4.4.

4.1 System Model

We consider a two-dimensional mmWave wireless ad hoc network, where PBs are deployed to charge users. The PBs are located outdoors and their locations form a homogeneous PPP ϕ with density λ. Throughout the chapter, we use X_i to denote both the random location as well as the ith PB itself. The PBs have access to a dedicated power supply (e.g., a battery or power grid) and transmit with constant power P using beamforming. The PB transmissions set up an energy field over the wireless ad hoc network region and users harvest power from the aggregate PB received signal [88]. We assume that the PBs randomly and independently choose a direction to point their main beams. Given a sufficient density of the PBs, this simple strategy ensures that the aggregate received power from PBs at different locations in the network is roughly on the same order. Similarly, the users point their main beam in a randomly chosen direction. This avoids the need for channel estimation and accurate beam alignment. In this chapter, without loss of generality, we focus on the characterization of the aggregate received power from PBs at an outdoor reference RX, Y_0, located at the origin.

4.1.1 MmWave Blockage Model

For outdoor mmWave transmissions, each link between the ith PB and the reference RX is susceptible to building blockages due to their high diffraction and penetration characteristics [68]. We adopt the state-of-the-art three-state blockage model [69], where each link can be in one of the following three states: (i) the link is in LOS state if no blockage exists, (ii) the link is in NLOS state if blockage exists and (iii) the link is in outage (OUT) state if the link is too weak to be established.

Assuming that the link between the ith PB and the RX has a Euclidean length of $r_i = \|X_i - Y_0\|$, the probabilities $p_{\text{LOS}}(\cdot)$, $p_{\text{NLOS}}(\cdot)$ and $p_{\text{OUT}}(\cdot)$ of it being in LOS, NLOS and OUT states, respectively, are

$$\begin{aligned} p_{\text{OUT}}(r_i) &= u(r_i - R_{\max}); \\ p_{\text{NLOS}}(r_i) &= u(r_i - R_{\min}) - u(r_i - R_{\max}); \\ p_{\text{LOS}}(r_i) &= 1 - u(r_i - R_{\min}), \end{aligned} \tag{4.1}$$

where $u(\cdot)$ denotes the unit step function, $R_{\min}$ is the radius of the LOS region and

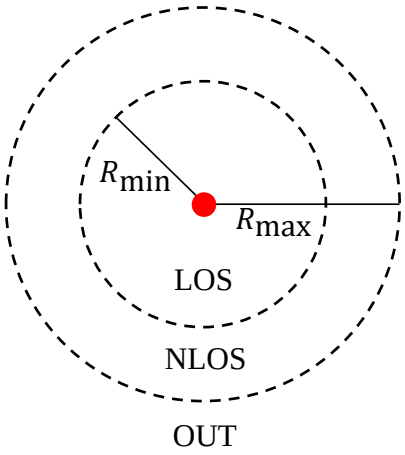

Figure 4.1: Illustration of mmWave blockage model.

$R_{\max}$ is the exclusion radius of the OUT region, as illustrated in Figure 4.1. The values of $R_{\min}$ and $R_{\max}$ depend on the propagation scenario and the carrier frequency. Typical values used in this chapter are summarized in Table 4.2.

4.1.2 MmWave Channel Model

Measurements have shown that mmWave links experience different channel conditions under LOS, NLOS and OUT states [89]. Hence, we adopt a path-loss plus fading channel model as follows.

We assume that a link in LOS state experiences Nakagami-m fading, while a link in NLOS state experiences Rayleigh fading. For the path-loss, we modify and adapt a multi-slope path-loss model and define the path-loss between the ith PB and the reference RX with a distance of r_i as follows:

$$PL(r_i) = \begin{cases} 1, & 0 \leqslant r_i < 1 \\ r_i^{-\alpha_{\mathrm{L}}}, & 1 \leqslant r_i < R_{\min} \\ \beta r_i^{-\alpha_{\mathrm{N}}}, & R_{\min} \leqslant r_i < R_{\max} \\ \infty, & R_{\max} \leqslant r_i \end{cases}, \tag{4.2}$$

where the first condition is added to ensure a bounded path-loss model, α_{L} denotes the path-loss exponent for the link in LOS state and subscript L denotes LOS, α_{N} denotes the path-loss exponent for the link in NLOS state ($2 \leqslant \alpha_{\mathrm{L}} \leqslant \alpha_{\mathrm{N}}$) and subscript N

Table 4.1: PMF of G_i

k	Gain G_k	Probability p_k
1	$G_p^{\max} G_r^{\max}$	$\frac{\theta_p \theta_r}{4\pi^2}$
2	$G_p^{\max} G_r^{\min}$	$\frac{\theta_p (2\pi - \theta_r)}{4\pi^2}$
3	$G_p^{\min} G_r^{\max}$	$\frac{(2\pi - \theta_p)\theta_r}{4\pi^2}$
4	$G_p^{\min} G_r^{\min}$	$\frac{(2\pi - \theta_p)(2\pi - \theta_r)}{4\pi^2}$

denotes NLOS, the path-loss of the link in OUT state is assumed to be infinite [69] and the continuity in the multi-slope path-loss model is maintained by introducing the constant $\beta \triangleq R_{\min}^{\alpha_N - \alpha_L}$ [90]. We also define $\delta_L = \frac{2}{\alpha_L}$ and $\delta_N = \frac{2}{\alpha_N}$ for convenience in presenting the analytical results in Section 4.2.

4.1.3 Beamforming Model

We assume that antenna arrays are used for beamforming at both the PBs and the reference RX. Following [68, 69], we approximate the actual antenna array pattern by a sectorized gain pattern which can be expressed as

$$G_a(\theta) = \begin{cases} G_a^{\max}, & |\theta| \leq \frac{\theta_a}{2} \\ G_a^{\min}, & \text{otherwise} \end{cases}, \tag{4.3}$$

where subscript $a = p$ for PB and $a = r$ for reference RX, $G_a^{\max}$ is the main lobe antenna gain, $G_a^{\min}$ is the side lobe antenna gain, $\theta \in [-\pi, \pi)$ is the angle off the boresight direction and θ_a is the main lobe beam-width. Note this model can be easily related to specific array geometries, such as an N element uniform planar or linear or circular array [70].

As stated earlier, the main beam at the PBs and RX are assumed to be randomly oriented with respect to each other and uniformly distributed in $[-\pi, \pi)$. Let G_i be the effective antenna gain on the link from the ith PB to the reference RX. As a result of sectorization, G_i is a discrete random variable with probability distribution as $G_i = G_k$ with probability p_k, $k \in \{1, 2, 3, 4\}$. The values of G_k and p_k are summarized in Table 4.1.

4.1.4 Power Transfer Model

We assume that the reference RX is equipped with a typical rectifier-based power RX to harvest power from the aggregate PB received signal [88]. Practical rectifier-based power RXs have a power RX activation threshold ϵ, i.e., the power RX is only activated when the aggregate received power from all the PBs is greater than ϵ [54]. We assume that once the power RX is properly activated, then the harvested power is linearly proportional to the aggregate received power from the PBs and the constant of proportionality ζ is the power conversion efficiency.

4.2 Aggregate Received Power from PBs

In this section, we provide the mathematical formulation to characterize the aggregate received power at the reference RX from all PBs.

Since the power harvested from the noise is negligible, the instantaneous aggregate received power at the reference RX from all the PBs can be expressed as

$$P_{\text{agg}} = P \sum_{X_i \in \phi} G_i h_i PL(r_i), \tag{4.4}$$

where P is the PB transmit power, G_i is the effective antenna gain between X_i and Y_0, h_i is the fading power gain between X_i and Y_0, which follows the Gamma distribution (under the Nakagami-m fading assumption) if the link is in LOS state and exponential distribution (under the Rayleigh fading distribution) if the link is in NLOS state and $PL(r_i)$ is the path-loss function in (4.2).

Note that P_{agg} in (4.4) is a random variable because of the randomness in the antenna gain, mmWave channels and locations of PBs. We use stochastic geometry to find its CCDF and also its nth cumulant.

4.2.1 CCDF and MGF of the Aggregate Received Power from PBs

The CCDF of the aggregate received power at the reference RX from all the PBs can be obtained by using the Gil-Pelaez inversion theorem [91]

$$\Pr(P_{\text{agg}} > z) = \frac{1}{2} + \frac{1}{\pi}\int_0^{\infty} \text{Im}[\mathcal{M}_{P_{\text{agg}}}(-j\omega)\exp(-j\omega z)]\frac{\text{d}\omega}{\omega}, \tag{4.5}$$

where $\Pr(\cdot)$ denotes the probability, $\text{Im}[\cdot]$ denotes the imaginary part of a complex number, $j = \sqrt{-1}$ is the imaginary unit, $\mathcal{M}_{P_{\text{agg}}}(s) = \mathbb{E}[\exp(-sP_{\text{agg}})]$ is the MGF of P_{agg} and $\mathbb{E}[\cdot]$ is the expectation operator.

The following proposition characterizes the exact MGF of P_{agg} in closed-form.

Proposition 4 *The MGF of the aggregate received power at the reference RX from all the PBs in a mmWave ad hoc network, following the system model in Section 4.1, is*

$$\begin{aligned}\mathcal{M}_{P_{agg}}(s) = &\prod_{k=1}^{4}\exp\Big(\pi\lambda R_{min}^2 p_k\Big(m^m(m+sR_{min}^{-\alpha_{\text{L}}}PG_k)^{-m}-1\Big)\\
&+\pi\lambda p_k\left(sPG_k\right)^{\delta_{\text{L}}}\left(\Xi_1\left(1\right)-\Xi_1\left(R_{min}\right)\right)+\pi\lambda p_k sPG_k\beta\left(\Xi_2(R_{min})-\Xi_2(R_{max})\right)\\
&+\frac{\pi\lambda}{2+\alpha_{\text{N}}}p_k(sPG_k\beta)^{\delta_{\text{N}}}\left(\Xi_3(R_{min})-\Xi_3(R_{max})\right)\Big),\end{aligned} \tag{4.6}$$

where

$$\Xi_1(r) = \frac{m^{m+1}\alpha_{\text{L}}(r^{-\alpha_{\text{L}}}sPG_k)^{-\delta_{\text{L}}-m}}{(2+m\alpha_{\text{L}})}\,{}_2F_1\left(1+m,m+\delta_{\text{L}};1+m+\delta_{\text{L}};-\frac{mr^{\alpha_{\text{L}}}}{sPG_k}\right), \tag{4.7}$$

$$\Xi_2(r) = \frac{r^2}{r^{\alpha_{\text{N}}}+sPG_k\beta}, \tag{4.8}$$

$$\begin{aligned}\Xi_3(r) = &\frac{(r^{-\alpha_{\text{N}}}sPG_k\beta)^{-\delta_{\text{N}}-1}}{r^{\alpha_{\text{N}}}+sPG_k\beta}\Big(sPG_k\beta(2+\alpha_{\text{N}})\\
&-2(r^{\alpha_{\text{N}}}+sPG_k\beta)\,{}_2F_1\Big(1,\delta_{\text{N}}+1;2+\delta_{\text{N}};-\frac{r^{\alpha_{\text{N}}}\beta^{-1}}{sPG_k}\Big)\Big),\end{aligned} \tag{4.9}$$

and ${}_2F_1(\cdot,\cdot;\cdot;\cdot)$ *is the Gaussian (or ordinary) hypergeometric function.*

Proof: See Appendix C.1. ■

Remark 4 *To the best of our knowledge, Proposition 4 presents the result for the MGF of P_{agg} in closed-form for the first time in the literature In addition,* (4.6) *substituted in* (4.5) *allows the CCDF to be numerically computed. Note that although the MGF in* (4.6) *is in closed-form, the CCDF in* (4.5) *cannot be expressed in closed-form due to complexity of the MGF which is inside the integration. However, it can be easily evaluated numerically using Mathematica.*

4.2.2 nth Cumulant of the Aggregate Received Power from PBs

The nth cumulant of the aggregate received power at the reference RX from all the PBs, $\kappa_{P_{\text{agg}}}(n)$, can also be expressed in terms of the MGF of P_{agg} as [92]

$$\kappa_{P_{\text{agg}}}(n) = (-1)^n \frac{d^n \ln \mathcal{M}_{P_{\text{agg}}}(s)}{ds^n}\Big|_{s=0}, \tag{4.10}$$

where ln is the natural logarithm. The following proposition characterizes the nth cumulant of P_{agg} in closed-form.

Proposition 5 *The nth cumulant of the aggregate received power at the reference RX from all the PBs in a mmWave ad hoc network, following the system model in Section 4.1, is given by*

$$\kappa_{P_{agg}}(n) = \sum_{k=1}^{4} \Big(\Psi_k^1(n) - \Psi_k^2(n) - \Psi_k^3(n) \Big), \tag{4.11}$$

where

$$\Psi_k^1(n) = \pi\lambda p_k P^n G_k^n m^{-n} m_{(n)}, \tag{4.12}$$

$$\Psi_k^2(n) = \begin{cases} 2\pi\lambda p_k P G_k \ln R_{min}, & \alpha_{\text{L}}{=}2 \;\&\; n{=}1 \\ \frac{2\pi\lambda\left(1-R_{min}^{-n\alpha_{\text{L}}+2}\right)}{2-n\alpha_{\text{L}}} (m)_n p_k \left(\frac{PG_k}{m}\right)^n, & \text{otherwise} \end{cases}, \tag{4.13}$$

$$\Psi_k^3(n) = \frac{2\pi\lambda\left(R_{min}^{-n\alpha_{\text{N}}+2} - R_{max}^{-n\alpha_{\text{N}}+2}\right)}{2-n\alpha_{\text{N}}} p_k P^n G_k^n \beta^n \Gamma(1{+}n), \tag{4.14}$$

$m_{(n)} = \frac{(m+n-1)!}{(m-1)!}$ *is the rising factorial and* $\Gamma(\cdot)$ *is the complete Gamma function.*

Proof: See Appendix C.2. ■

4.2.3 Closed-form Approximation of the CCDF of the Aggregate Received Power

Since the exact CCDF of the aggregate received power cannot be expressed in closed-form, we test various distributions which can be used to approximate the CCDF in this section. The distribution of P_{agg} is approximated by the well known closed-form

distributions by second-order moment matching, i.e., by matching the mean and the variance of the two distributions, where the mean and the variance of P_{agg} can be found from Proposition 5. First, we present the skewness and the kurtosis of P_{agg}, which are two important measures of a real-valued random variable.

Skewness and Kurtosis of P_{agg}: The skewness and the kurtosis describe the shape of the probability distribution of P_{agg} [93], and are given by

$$\text{Skew}\left[P_{\text{agg}}\right] = \frac{\kappa_{P_{\text{agg}}}(3)}{\kappa_{P_{\text{agg}}}(2)^{1.5}}, \tag{4.15}$$

$$\text{Kurt}\left[P_{\text{agg}}\right] = \frac{\kappa_{P_{\text{agg}}}(4)}{\kappa_{P_{\text{agg}}}(2)^{2}}. \tag{4.16}$$

The skewness shows whether a distribution is left or right tailed and the kurtosis measures the heaviness of the tail.

Gaussian Distribution: The CCDF of the Gaussian distribution is

$$\Pr\left(P_{\text{agg}} > z\right)^{\text{Gaussian}} = Q\left(\frac{z - \kappa_{P_{\text{agg}}}(1)}{\sqrt{\kappa_{P_{\text{agg}}}(2)}}\right), \tag{4.17}$$

where $Q(\cdot)$ is the Q-function, $\kappa_{P_{\text{agg}}}(1)$ and $\kappa_{P_{\text{agg}}}(2)$ are the first and the second cumulant of P_{agg}, respectively, which can be calculated by (4.11).

Lognormal Distribution: The CCDF of the lognormal distribution is

$$\Pr\left(P_{\text{agg}} > z\right)^{\text{lognormal}} = Q\left(\frac{\ln z - \mu^{\text{lognormal}}}{\sigma^{\text{lognormal}}}\right), \tag{4.18}$$

where $\mu^{\text{lognormal}}$ and $\sigma^{\text{lognormal}}$ are the location parameter and the scale parameter given by

$$\mu^{\text{lognormal}} = \ln\left(\frac{\kappa_{P_{\text{agg}}}(1)}{\sqrt{1 + \frac{\kappa_{P_{\text{agg}}}(2)}{\kappa_{P_{\text{agg}}}(1)^{2}}}}\right), \tag{4.19}$$

$$\sigma^{\text{lognormal}} = \sqrt{\ln\left(1 + \frac{\kappa_{P_{\text{agg}}}(2)}{\kappa_{P_{\text{agg}}}(1)^{2}}\right)}. \tag{4.20}$$

Table 4.2: Parameter Values.

Parameter	Value	Parameter	Value
α_{L}	$\{2, 2.5\}$	$R_{\min}$	$\{50\text{ m}, 100\text{ m}\}$
α_{N}	4	$R_{\max}$	200 m
P	10 dB	$G_p^{\max}$, $G_p^{\min}$, θ_p	$\{[0\text{ dB}, 0\text{ dB}, 360^{\mathrm{o}}]$, $[20\text{ dB}, -10\text{ dB}, 30^{\mathrm{o}}]$, $[30\text{ dB}, -10\text{ dB}, 6^{\mathrm{o}}]\}$
λ	$10^5 \sim 1$ per km^2	$G_r^{\max}$, $G_r^{\min}$, θ_r	$\{[0\text{ dB}, 0\text{ dB}, 360^{\mathrm{o}}]$, $[10\text{ dB}, -10\text{ dB}, 45^{\mathrm{o}}]\}$
ζ	0.5	m	$\{5, 10\}$

Gamma Distribution: The CCDF of the Gamma distribution is

$$\Pr\left(P_{\mathrm{agg}} > z\right)^{\mathrm{gamma}} = 1 - \frac{\gamma\left(k^{\mathrm{gamma}}, \frac{z}{\theta^{\mathrm{gamma}}}\right)}{\Gamma\left(k^{\mathrm{gamma}}\right)}, \tag{4.21}$$

where $\gamma(\cdot,\cdot)$ is the lower incomplete Gamma function, $k^{\mathrm{gamma}} = \frac{\kappa_{P_{\mathrm{agg}}}(1)^2}{\kappa_{P_{\mathrm{agg}}}(2)}$ and $\theta^{\mathrm{gamma}} = \frac{\kappa_{P_{\mathrm{agg}}}(2)}{\kappa_{P_{\mathrm{agg}}}(1)}$ are the shape parameter and scale parameter of Gamma distribution, respectively.

4.3 Results

In this section, we present the analytical or numerical results and compare with the simulation results. The simulation results are generated by averaging over 10^8 Monte carlo simulation runs. The values of the main parameters are summarized in Table 4.2, which are chosen to be consistent with the literature in mmWave and WPT [13, 68]. Note that if the distance between the PB and the RX is more than $R_{\max} = 200$ m, the mmWave link is in OUT state.

4.3.1 Distribution Approximation of the Aggregate Received Power

The skewness and the kurtosis of P_{agg} versus the density of PB λ are plotted in Figure 4.2(a) and 4.2(b) respectively for different path-loss exponents of LOS link $\alpha_{\mathrm{L}} = 2, 2.5$ and different Nakagami-m fading parameters $m = 5, 10$. We can see that the curves are monotonic for the considered range of λ. Smaller α_{L} and larger m lead

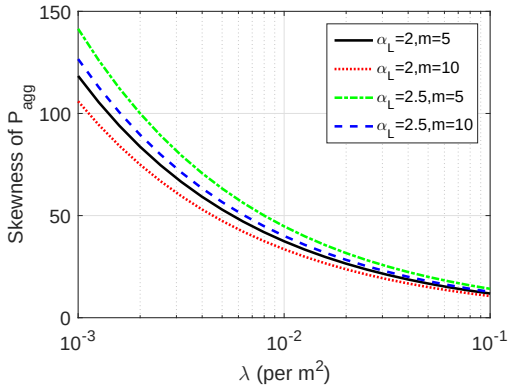

(a) Skewness of the aggregate received power versus the density of PB for different path-loss exponents and Nakagami-m fading parameters for LOS links.

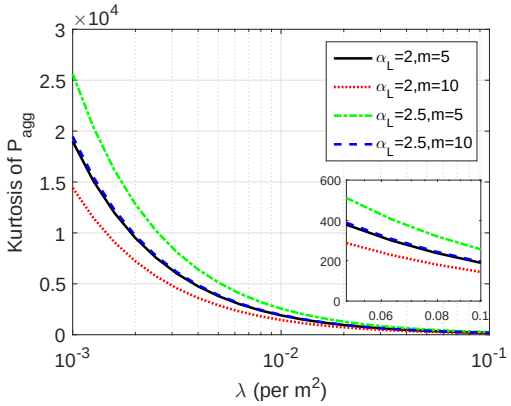

(b) Kurtosis of the aggregate received power versus the density of PB for different path-loss exponents and Nakagami-m fading parameters for LOS links.

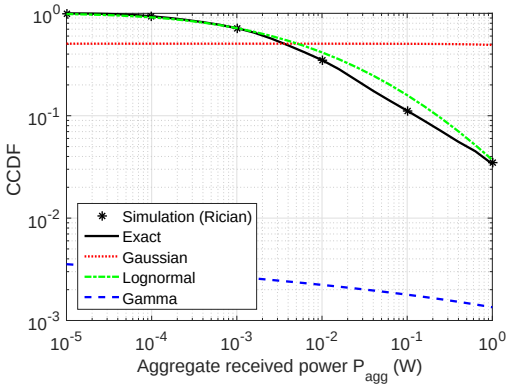

(c) CCDF approximation of the aggregate received power P_{agg} of networks in which LOS links experience Nakagami-m fading with $m = 5$ and simulation of networks in which LOS links experience Rician fading with $K = 10$ dB. The PB density is 100 per km^2 and the path-loss exponent of LOS links is 2.

Figure 4.2: Skewness, kurtosis and CCDF approximation of the aggregate received power with the radius of the LOS region being 100 m and the PB and RX beamforming parameter being [20 dB, -10 dB, 30$^{\text{o}}$] and [10 dB, -10 dB, 45$^{\text{o}}$] respectively.

to smaller skewness and kurtosis. As the density of PB increases, the gap between the different curves becomes smaller. The distribution of the aggregate received power is skewed to the right with a heavy tail, because both the skewness and the kurtosis of P_{agg} are much greater than 0. Moreover, the skewness and the kurtosis of a Gaussian distributed random variable are 0. Hence, we can conclude that the aggregate received

power under the considered system model does not converge to a Gaussian distribution (even for the very extreme case with a PB density of 0.1 per m^2).

Figure 4.2(c) plots the exact and approximated CCDF of P_{agg} for $\alpha_{\text{L}} = 2$ and $m = 5$. The simulation results assume the LOS links undergo Rician fading with $K = 10$ dB. The exact CCDF is plotted numerically using (4.5) and (4.6), while the approximated CCDFs are obtained using (4.17) for Gaussian distribution, (4.18) for lognormal distribution and (4.21) for Gamma distribution. From the figure, we can see that the CCDF of P_{agg} under Rician fading LOS links can be closely approximated by Nakagami-m fading by adjusting the m values. Gaussian distribution does not provide a good approximation, which agrees with our discussion above. Gamma distribution is found to provide a close approximation to the power distribution of homogeneous PPP network [94] and heterogeneous PPP network [95] with non-singular path-loss model, but it clearly does not provide a good fit under the mmWave system model. We have tested the CCDF approximations using inverse Gaussian distribution, exponential distribution, Suzuki distribution and inverse Gamma distribution against the exact CCDF and Rician LOS fading simulation under different channel parameters as well. However, they perform poorly and the results are omitted here for the sake of brevity. Overall, our results show that lognormal distribution provides the best CCDF approximation of P_{agg}.

4.3.2 Mean Aggregate Received Power

Next, we investigate the impact of the channel parameters and the beamforming parameters on the the mean aggregate received power $\overline{P_{\text{agg}}} = \kappa_{P_{\text{agg}}}(1)$.

Figure 4.3 plots $\overline{P_{\text{agg}}}$ against the density of PB for different path-loss exponents of LOS link $\alpha_{\text{L}} = 2, 2.5$ and different radius of the LOS region $R_{\text{min}} = 50$ m, 100 m. We can see that the simulation results match perfectly with the analytical results. The figure also shows that $\overline{P_{\text{agg}}}$ increases with λ. With smaller α_{L} and larger R_{min}, $\overline{P_{\text{agg}}}$ grows at a faster rate. When $\alpha_{\text{L}} = 2.5$, the traces of two different R_{min} overlap. We can see that the benefit of increasing the radius of the LOS region is insignificant, when α_{L} is large.

Figure 4.4 plots $\overline{P_{\text{agg}}}$ against the density of PB for different beamforming parameter for PB $[0\text{ dB}, 0\text{ dB}, 360^{\text{o}}]$, $[20\text{ dB}, -10\text{ dB}, 30^{\text{o}}]$, $[30\text{ dB}, -10\text{ dB}, 6^{\text{o}}]$ and TX $[0\text{ dB}, 0\text{ dB}, 360^{\text{o}}]$, $[10\text{ dB}, -10\text{ dB}, 45^{\text{o}}]$. Again the simulation results match perfectly with the analytical results. We can see that a narrower main lobe beam-width gives a

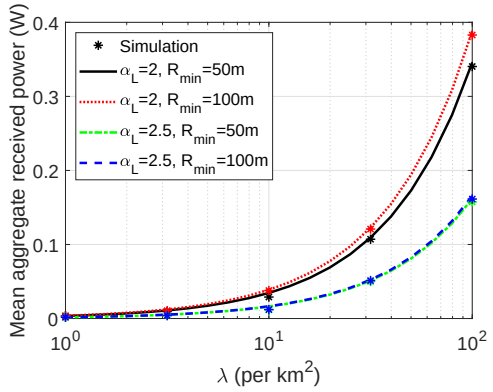

Figure 4.3: Mean aggregate received power versus the density of PB for different path-loss exponents of LOS links and different radius of the LOS region with the Nakagami-m fading parameter being 5 and the PB and RX beamforming parameter being [20 dB, -10 dB, 30^o] and [10 dB, -10 dB, 45^o] respectively.

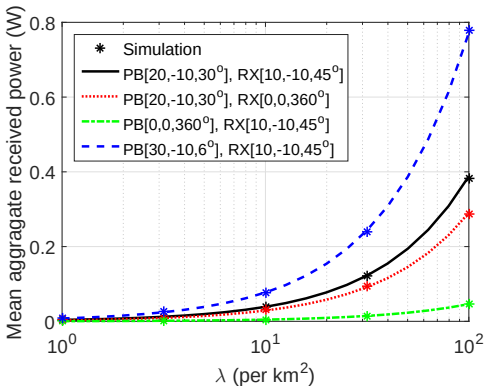

Figure 4.4: Mean aggregate received power versus the density of PB for different beamforming parameters for PB and RX with the radius of the LOS region being 100 m and the path-loss exponent being 2 and the Nakagami-m fading parameter being 5 for LOS links.

larger main lobe gain which results in a faster rate of growth of $\overline{P_{\text{agg}}}$ with respect to λ.

4.3.3 Feasibility of Wireless Power Transfer via PBs

In this section, we examine the feasibility of WPT via PBs in a mmWave ad hoc network. In this regard, it is important to note that the electronic circuitry of a power RX has an activation threshold which has a value typically between -30 dBm and -20 dBm [13]. In addition, the typical maintenance power for a smart phone is between 20 mW and 30 mW [96].

Figure 4.5 plots the required transmit power of PB to achieve an average harvested power of 15 dBm ($=$ 31.62 mW), which is the typical maintenance power for a smart phone and is much higher than the power sensitivity level, versus the density of PB by assuming a constant power conversion efficiency of $\zeta = 0.5$ [13]. From the figure, we can see that for a fixed PB density the decrease in the LOS path-loss exponents brings a higher saving in the transmit power needed than the increase in the radius of LOS region. From Figure 4.5, the maximum transmit power required at a PB density of 10 per km^2 is 39.12 W. If PB transmits with this maximum value, the power density at a distant of 1 m from the PB is 3.113 W$/$m^2. This power density is smaller than 10

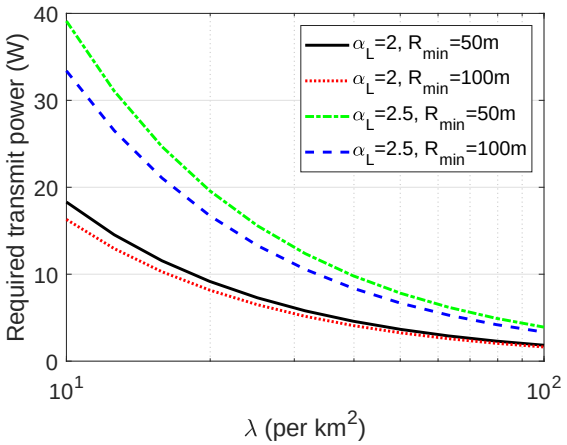

Figure 4.5: Required transmit power of PB versus the density of PB for different path-loss exponents of LOS links and different radius of the LOS region with the Nakagami-m fading parameter being 5 and the PB and RX beamforming parameter being [20 dB, -10 dB, 30°] and [10 dB, -10 dB, 45°] respectively.

W/m^2, which is the permissible safety level of human exposure to RF electromagnetic fields based on IEEE Standard [88].

4.4 Summary

In this chapter, the mmWave wireless ad hoc network where RX harvests energy from all PBs was considered. We first derived the MGF and the nth cumulant of the aggregate received power at the RX to study the CCDF of the aggregate received power. Furthermore, we compared the different closed-form distributions which can be used to approximate the characteristics of the aggregate received power. Our results showed that the lognormal distribution provided the best CCDF approximation compared to other distributions considered in the literature for microwave network. The results have also shown that application of mmWave PB is feasible under practical network setup.

Chapter 5

Power Beacon-Assisted Millimeter Wave Ad Hoc Networks

In Chapter 4, we have studied the characteristic of the aggregate received power from PBs in mmWave ad hoc networks. In this chapter, we present a tractable model for PB-assisted mmWave wireless ad hoc networks, where each TX harvests energy from all PBs and then uses the harvested energy to transmit information to its desired RX. Our model accounts for realistic aspects of WPT and mmWave transmissions, such as power circuit activation threshold, allowed maximum harvested power, maximum transmit power, beamforming and blockage. Using stochastic geometry, we obtain the Laplace transform of the aggregate received power at the TX to calculate the power coverage probability. We approximate and discretize the transmit power of each TX into a finite number of discrete power levels in log scale to compute the channel and total coverage probability. We compare our analytical predictions to simulations and observe good accuracy. The proposed model allows insights into effect of system parameters, such as transmit power of PBs, PB density, main lobe beam-width and power circuit activation threshold on the overall coverage probability. The results confirm that it is feasible and safe to power TXs in a mmWave wireless ad hoc network using PBs.

This chapter is organized as follows: Section 5.1 describes the system model and assumptions. Section 5.2 focuses on the power transfer phase of the system and derives the power coverage probability. Section 5.3 details the information transmission phase, which covers the analysis of transmit power statistics and channel coverage probability. Section 5.4 investigates the total coverage probability. Section 5.5 presents the results and the effect of the system parameters on the network performance. Finally, Section 5.6 summarizes the chapter.

5.1 System Model

We consider a two-dimensional mmWave wireless ad hoc network, where TXs are first wirelessly charged by PBs and then they transmit information to RXs. The locations of PBs are modeled as a homogeneous PPP ϕ_p in $\mathbb{R}^2$ with constant node density λ_p. TXs are assumed to be randomly independently deployed and their locations are modeled as a homogeneous PPP ϕ_t with node density λ_t. For each TX, it has a desired RX located at a distance d_0 in a random direction. We use X_i to denote both the random location as well as the ith TX itself, Y_i to denote both the location and the corresponding ith RX and Z_i to denote both the location and the ith PB, respectively. Note that we assume the indoor-to-outdoor penetration loss is high. Therefore, all the PBs, TXs and RXs can be regarded as outdoor devices.

5.1.1 Power Transfer and Information Transmission Model

We assume that each PB has access to a dedicated power supply (e.g., a battery or power grid) and transmits with a constant power P_p. Time is divided into slots and T denotes one time slot. TXs adopt the harvest-then-transmit protocol to perform power transfer and information transmission. Specifically, each time slot T is divided into two parts with ratio $\tau \in (0,1)$: in the first τT seconds each TX harvests energy from the RF signal transmitted by PBs and stores the energy in an ideal (infinite capacity) battery[1]. In the remaining $(1-\tau)T$ seconds, TXs use all the harvested energy to transmit information to their desired RXs. Hence, there is no interference between the power transfer and information transmission stages. We make the following assumptions for realistic modeling of power transfer:

- Different from previous works [53, 60, 98], where energy harvesting activation threshold is not considered and the devices can harvest power from any amount of incident power, we assume that the TX can scavenge energy if and only if the instantaneous aggregate received power from all PBs is greater than a power circuit activation threshold γ_{PT}. If this condition is met, then the TX is called an *active TX*. Otherwise, the TX will be inactive and will not scavenge any energy from the PBs.

- Once the energy harvesting circuit is activated, the harvested power at the active

[1] In this chapter, we do not consider the impact of battery imperfections [97].

TX is assumed to be linearly proportional to the aggregate received power with power conversion efficiency ζ. Due to the saturation of the energy harvesting circuit, the harvested power at the active TX cannot exceed a maximum level denoted as $P_1^{\max}$ [99]. In addition, the active TX cannot transmit information with a power greater than $P_2^{\max}$ because of the safety regulation and the electrical rating of the antenna circuit [88].

5.1.2 MmWave Blockage Model

Under outdoor mmWave transmissions, each link between the PB and the TX (i.e., PB-TX link) or between the TX and the RX (i.e., TX-RX link) is susceptible to building blockages due to their high diffraction and penetration characteristics [68]. We adopt the state-of-the-art three-state blockage model as in [69, 100], where each PB-TX or TX-RX link can be in one of the following three states: (i) the link is in LOS state if no blockage exists, (ii) the link is in NLOS state if blockage exists and (iii) the link is in OUT state if the link is too weak to be established.

Given that the PB-TX or TX-RX link has a length of r, the probabilities $p_{\mathrm{LOS}}(\cdot)$, $p_{\mathrm{NLOS}}(\cdot)$ and $p_{\mathrm{OUT}}(\cdot)$ of it being in LOS, NLOS and OUT states, respectively, are

$$\begin{aligned} p_{\mathrm{OUT}}(r) &= u(r - R_{\max}); \\ p_{\mathrm{NLOS}}(r) &= u(r - R_{\min}) - u(r - R_{\max}); \\ p_{\mathrm{LOS}}(r) &= 1 - u(r - R_{\min}), \end{aligned} \tag{5.1}$$

where $u(\cdot)$ denotes the unit step function, $R_{\min}$ is the radius of the LOS region and $R_{\max}$ is the exclusion radius of the OUT region[2]. The values of $R_{\min}$ and $R_{\max}$ depend on the propagation scenario and the mmWave carrier frequency [69]. Moreover, the communication link between TX and its desired RX is assumed to be always in LOS state.

5.1.3 MmWave Channel Model

It has been shown by the measurements that mmWave links experience different channel conditions under LOS, NLOS and OUT states [89]. Thus, we consider the following path-loss plus block fading channel model.

[2]Note that the two-state blockage model in [101, 102], which does not consider the OUT region, can be considered as a special case of the three-state blockage model with $R_{\max} = \infty$.

For the path-loss, we adopt and modify a multi-slope path-loss model [90] and define the path-loss of PB-TX or TX-RX link with a propagation distance of r as follows:

$$PL(r) = \begin{cases} 1, & 0 \leqslant r < 1 \\ r^{-\alpha_{\mathrm{L}}}, & 1 \leqslant r < R_{\min} \\ \beta r^{-\alpha_{\mathrm{N}}}, & R_{\min} \leqslant r < R_{\max} \\ \infty, & R_{\max} \leqslant r \end{cases}, \tag{5.2}$$

where the first condition is added to avoid the singularity as $r \to 0$, α_{L} denotes the path-loss exponent for the link in LOS state, α_{N} denotes the path-loss exponent for the link in NLOS state ($2 \leqslant \alpha_{\mathrm{L}} \leqslant \alpha_{\mathrm{N}}$), the path-loss of the link in OUT state is assumed to be infinite [69] and the continuity in the multi-slope path-loss model is maintained by introducing the constant $\beta \triangleq R_{\min}^{\alpha_{\mathrm{N}}-\alpha_{\mathrm{L}}}$ [90].

As for the fading, the link under LOS state is assumed to experience Nakagami-m fading, while the link under NLOS state is assumed to experience Rayleigh fading[3]. Furthermore, both the LOS and the NLOS links experience AWGN with variance σ^2. However, under the power transfer phase, the AWGN power is too small to be harvested by TXs. Hence, we ignore it in the power transfer phase.

5.1.4 Beamforming Model

To compensate the large path-loss in mmWave band, directional beamforming is necessary for devices [104]. In this chapter, we consider that mmWave antenna arrays perform directional beamforming at all PBs, TXs and RXs. Similar to [68, 69], the actual antenna array pattern can be approximated by a sectorized gain pattern which is given by

$$G_a(\theta) = \begin{cases} G_a^{\max}, & |\theta| \leq \frac{\theta_a}{2} \\ G_a^{\min}, & \text{otherwise} \end{cases}, \tag{5.3}$$

where subscript $a = p$ for PB, $a = t$ for TX and $a = r$ for RX, $G_a^{\max}$ is the main lobe antenna gain, $G_a^{\min}$ is the side lobe antenna gain, $\theta \in [-\pi, \pi)$ is the angle off the boresight direction and θ_a is the main lobe beam-width. Note that, as shown in

[3]We do not consider shadowing but it can be included using the composite fading model in [103].

Table 5.1: PMF of G_{ij} and D_{ij}.

	PB-TX gain G_{ij}		TX-RX gain D_{ij}	
k	Gain G_k	Probability p_k	Gain D_k	Probability q_k
1	$G_p^{\max}G_t^{\max}$	$\frac{\theta_p\theta_t}{4\pi^2}$	$G_t^{\max}G_r^{\max}$	$\frac{\theta_t\theta_r}{4\pi^2}$
2	$G_p^{\max}G_t^{\min}$	$\frac{\theta_p(2\pi-\theta_t)}{4\pi^2}$	$G_t^{\max}G_r^{\min}$	$\frac{\theta_t(2\pi-\theta_r)}{4\pi^2}$
3	$G_p^{\min}G_t^{\max}$	$\frac{(2\pi-\theta_p)\theta_t}{4\pi^2}$	$G_t^{\min}G_r^{\max}$	$\frac{(2\pi-\theta_t)\theta_r}{4\pi^2}$
4	$G_p^{\min}G_t^{\min}$	$\frac{(2\pi-\theta_p)(2\pi-\theta_t)}{4\pi^2}$	$G_t^{\min}G_r^{\min}$	$\frac{(2\pi-\theta_t)(2\pi-\theta_r)}{4\pi^2}$

Section 5.5.3, this model can be easily related to specific array geometries, such as an N element uniform planar or linear or circular array [70].

The main beam at the PBs are assumed to be randomly and independently oriented with respect to each other and uniformly distributed in $[-\pi, \pi)$. Given a sufficient density of the PBs, this simple strategy ensures that the aggregate received power from PBs at different locations in the network is roughly on the same order and avoids the need for channel estimation and accurate beam alignment. In addition, it has been shown in [104] that the random directional beamforming can perform reasonably well given that more than one users need to be served.

Let G_{ij} be the effective antenna gain on the link from the ith PB to the jth TX. Under sectorization, G_{ij} is a discrete random variable with probability $p_k = \Pr(G_{ij} = G_k)$ and $k \in \{1, 2, 3, 4\}$, where its distribution is summarized in Table 5.1.

With regards to TX and RX, we assume that each TX points its main lobe towards its desired RX directly. Therefore, the effective antenna gain of the desired TX-RX link is $D_0 = G_t^{\max}G_r^{\max}$ and the orientation of the beam of the interfering TX is uniformly distributed in $[-\pi, \pi)$. Let $D_{ij}(i \neq j)$ be the effective antenna gain on the link from the ith TX to the jth RX. Similar to G_{ij}, D_{ij} is a discrete random variable with probability $q_k = \Pr(D_{ij} = D_k)$, where its distribution is given in Table 5.1.

5.1.5 Metrics

In this chapter, we are interested in the PB-assisted mmWave wireless ad hoc network in terms of the total coverage probability for RXs (i.e., the probability that a RX can successfully receive the information from its TX after the TX successfully harvests energy from PBs). Based on the system model described above, the success of this event has to satisfy two requirements, which are:

- *The corresponding TX is in power coverage*. Due to the random network topology and the fading channels, the aggregate received power from all PBs is a random variable. If the aggregate received power at a TX is greater than the power circuit activation threshold, the energy harvesting circuit is active and this TX can successfully harvest energy from PBs. As a result, the TX is under power coverage and information transmission then takes place.

- *The RX is in channel coverage*. The instantaneous transmit power for each active TX depends on its random received power. RX can receive the information from its desired TX (i.e., in channel coverage) if the SINR at the RX is above a certain threshold.

By leveraging the Laplace transform of the aggregate received power at a typical TX and the interference at a typical RX, we compute the power coverage probability and channel coverage probability in the following sections. In the subsequent analysis, we condition on having a reference RX Y_0 at the origin $(0,0)$ and its associated TX X_0 located at a distance d_0 away at $(d_0,0)$. According to Slivnyak's theorem, the conditional distribution is the same as the original one for the rest of the network [105].

5.2 Power Transfer

In this section, we focus on the power transfer phase of the system. We analyze the aggregate received power at a reference TX from all PBs and find the power coverage probability at the corresponding RX.

Since the power harvested from the noise is negligible, the instantaneous aggregate received power at the typical TX X_0 from all the PBs can be expressed as

$$P_{\mathrm{PT}} = P_p \sum_{Z_i \in \phi_p} G_{i0} g_{i0} PL(r_i), \tag{5.4}$$

where P_p is the PB transmit power, G_{i0} is the effective antenna gain between Z_i and X_0, g_{i0} is the fading power gain between the ith PB Z_i and the typical TX X_0, which follows the Gamma distribution (under Nakagami-m fading assumption) if the PB-TX link is in LOS state and exponential distribution (under Rayleigh fading distribution) if the PB-TX link is in NLOS state. $PL(r_i)$ is the path-loss function given in (5.2) and

$r_i = \|Z_i - X_0\|$ is the Euclidean length of the PB-TX link between Z_i and X_0. Using (5.4), the power coverage probability is defined as follows:

Definition 2 *The power coverage probability is the probability that the aggregate received power at the typical TX is higher than the power circuit activation threshold γ_{PT}. It can be expressed as*

$$\mathbb{P}^{P}_{\mathrm{cov}}(\gamma_{\mathrm{PT}}) = \Pr(P_{\mathrm{PT}} > \gamma_{\mathrm{PT}}). \tag{5.5}$$

Remark 5 *Analytically characterizing the power coverage probability in* (5.5) *is a challenging open problem in the literature. Generally, it is not possible to obtain a closed-form power coverage probability because of the randomness in the antenna gain, mmWave channels and locations of PBs. The closed-form expression only exists under the unbounded path-loss model with $\alpha = 4$ and Rayleigh fading for all links, which is shown to be Lévy distribution [105]. To overcome this problem, some works [59, 101, 106] employed the Gamma scaling method. This approach involves introducing a dummy Gamma random variable with parameter N' to reformulate the original problem. However, the approach can sometimes lead to large errors with finite N' value. Other works adopted the Gil-Pelaez inversion theorem [91]. This approach involves one fold integration and is only suitable for the random variable with a simple Laplace transform. If the Laplace transform is even moderately complicated, this method is not very efficient even if the Laplace transform is in closed-form.*

In this chapter, we adopt a numerical inversion method, which is easy to compute, if the Laplace transform of a random variable is in closed-form, and provides controllable error estimation. Following [85, 86], the cumulative distribution function (CDF) of the aggregate received power P_{PT} is given as

$$F_{P_{\mathrm{PT}}}(x) = \frac{1}{2\pi j}\int_{a-j\infty}^{a+j\infty} \mathcal{L}_{F_{P_{\mathrm{PT}}}}(s)\exp(sx)\mathrm{d}s \tag{5.6a}$$

$$= \frac{1}{2\pi j}\int_{a-j\infty}^{a+j\infty} \frac{\mathcal{L}_{P_{\mathrm{PT}}}(s)}{s}\exp(sx)\mathrm{d}s. \tag{5.6b}$$

where (5.6a) is obtained according to the Bromwich integral [107] and (5.6b) follows from probability theory that $\mathcal{L}_{P_{\mathrm{PT}}}(s) = s\mathcal{L}_{F_{P_{\mathrm{PT}}}}(s)$. Using the trapezoidal rule and the Euler summation, the above integral can be transformed into a finite sum. Therefore,

we can express the power coverage probability as

$$\mathbb{P}^{P}_{\text{cov}}(\gamma_{\text{PT}}) = 1 - \frac{2^{-B}\exp(\frac{A}{2})}{\gamma_{\text{PT}}} \sum_{b=0}^{B} \binom{B}{b} \sum_{c=0}^{C+b} \frac{(-1)^c}{D_c} \text{Re}\left[\frac{\mathcal{L}_{P_{\text{PT}}}(s)}{s}\right], \tag{5.7}$$

where $\text{Re}[\cdot]$ is the real part operator, $s = \frac{A+j2\pi c}{2\gamma_{\text{PT}}}$, $\mathcal{L}_{P_{\text{PT}}}(s)$ is the Laplace transform of P_{PT}, $D_c = 2$ (if $c = 0$) and $D_c = 1$ (if $c = 1, 2, ..., C + b$). A, B and C are positive parameters used to control the estimation accuracy.

From (5.7), the key parameter in order to obtain the power coverage probability is $\mathcal{L}_{P_{\text{PT}}}(s)$. By the definition of Laplace transform of a random variable, we express $\mathcal{L}_{P_{\text{PT}}}(s)$ in closed-form in the following theorem.

Theorem 8 *Following the system model in Section 5.1, the Laplace transform of the aggregate received power at the typical TX from all the PBs in a mmWave ad hoc network is*

$$\begin{aligned}\mathcal{L}_{P_{\text{PT}}}(s) =& \prod_{k=1}^{4} \exp\Big(\pi\lambda_p R_{min}^2 p_k \Big(m^m (m + sR_{min}^{-\alpha_{\text{L}}} P_p G_k)^{-m} - 1\Big) \\ &+ \pi\lambda_p p_k \left(sP_p G_k\right)^{\delta_{\text{L}}} \left(\Xi_1(1) - \Xi_1(R_{min})\right) + \pi\lambda_p p_k sP_p G_k \beta \left(\Xi_2(R_{min}) - \Xi_2(R_{max})\right) \\ &+ \frac{\pi\lambda_p}{2+\alpha_{\text{N}}} p_k (sP_p G_k \beta)^{\delta_{\text{N}}} (\Xi_3(R_{min}) - \Xi_3(R_{max}))\Big),\end{aligned} \tag{5.8}$$

where

$$\Xi_1(r) = \frac{m^{m+1}\alpha_{\text{L}} (r^{-\alpha_{\text{L}}} sP_p G_k)^{-\delta_{\text{L}}-m}}{(2 + m\alpha_{\text{L}})} \, {}_2F_1\left(1+m, m+\delta_{\text{L}}; 1+m+\delta_{\text{L}}; -\frac{mr^{\alpha_{\text{L}}}}{sP_p G_k}\right), \tag{5.9}$$

$$\Xi_2(r) = \frac{r^2}{r^{\alpha_{\text{N}}} + sP_p G_k \beta}, \tag{5.10}$$

$$\begin{aligned}\Xi_3(r) = & \frac{(r^{-\alpha_{\text{N}}} sP_p G_k \beta)^{-\delta_{\text{N}}-1}}{r^{\alpha_{\text{N}}} + sP_p G_k \beta} \Big(sP_p G_k \beta (2 + \alpha_{\text{N}}) \\ & -2(r^{\alpha_{\text{N}}} + sP_p G_k \beta) {}_2F_1\left(1, \delta_{\text{N}}+1; 2+\delta_{\text{N}}; -\frac{r^{\alpha_{\text{N}}} \beta^{-1}}{sP_p G_k}\right)\Big),\end{aligned} \tag{5.11}$$

${}_2F_1(\cdot,\cdot;\cdot;\cdot)$ is the Gaussian (or ordinary) hypergeometric function, $\delta_{\text{L}} \triangleq \frac{2}{\alpha_{\text{L}}}$ and $\delta_{\text{N}} \triangleq \frac{2}{\alpha_{\text{N}}}$.

Proof: The proof follows the same lines as Proposition 4 and is skipped for the sake of brevity. ■

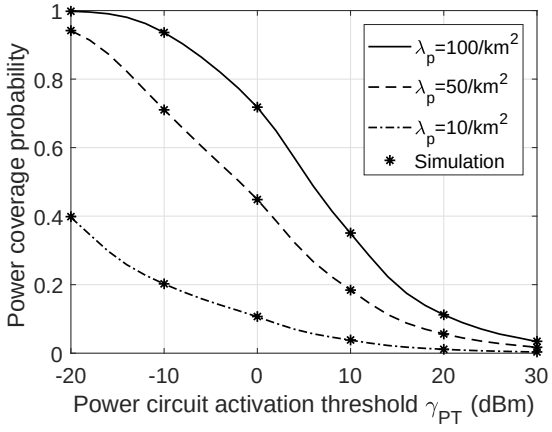

Figure 5.1: Power coverage probability versus power circuit activation threshold γ_{PT} for different PB densities. Other system parameters follow Table 5.3.

By substituting (5.8) into (5.7), we can compute the power coverage probability. As shown in Theorem 8, the Laplace transform of P_{PT} is in closed-form; hence, $\mathbb{P}^{P}_{\mathrm{cov}}(\gamma_{\mathrm{PT}})$ is just a summation over a finite number of terms. Following the selection guideline of parameters A, B and C in [86], we can achieve a stable numerical result by carefully choosing them.

Finally, we validate the analysis for the power coverage probability. Figure 5.1 plots the power coverage probability versus power circuit activation threshold. The simulation results are generated by averaging over 10^8 Monte Carlo simulation runs. We set $A = 24$, $B = 20$ and $C = 30$ in order to achieve an estimation error of 10^{-10}. The other system parameters follow Table 5.3. From the figure, we can see that the analytical results match perfectly with the simulation results, which demonstrates the accuracy of the proposed approach. Figure 5.1 also shows that the power coverage probability increases with the density of PBs, because the aggregate received power at TX increases as the PB density increases.

5.3 Information Transmission

In this section we focus on the information transmission phase between the TX and RX. We assume that the TX uses all the harvested energy in the information transmission phase. As indicated in Section 5.1.1, the transmit power of an active TX is a random variable which depends on its harvested power. Hence, we first evaluate the transmit power for an active TX. Then, we calculate the channel coverage prob-

ability at the reference RX. Note that the derived channel coverage probability is in fact a conditional probability, which is conditioned on the reference TX-RX link being active.

5.3.1 Transmit Power and Locations of Active TX

Using the power transfer assumptions in Section 5.1.1, the instantaneous transmit power for each active TX is

$$P_t = \begin{cases} \frac{\zeta\tau}{1-\tau} P_{\mathrm{PT}}, & \min(\frac{P_1^{\max}}{\zeta}, \frac{1-\tau}{\zeta\tau} P_2^{\max}) > P_{\mathrm{PT}} \geqslant \gamma_{\mathrm{PT}} \\ \min(\frac{\tau P_1^{\max}}{1-\tau}, P_2^{\max}), & P_{\mathrm{PT}} \geqslant \min(\frac{P_1^{\max}}{\zeta}, \frac{1-\tau}{\zeta\tau} P_2^{\max}) \end{cases}, \tag{5.12}$$

where $0 \leqslant \zeta \leqslant 1$ is the power conversion efficiency. Note that the first condition in (5.12) comes from the fact that the received power at an active TX must be greater than γ_{PT}. For the second condition in (5.12), $P_1^{\max}$ is the maximum harvested power at an active TX when the energy harvesting circuit is saturated and $P_2^{\max}$ is the maximum transmit power for an active TX. Thus, the second condition caps the transmit power by the allowed maximum harvested power constraint or the maximum transmit power constraint.

The following remarks discuss the modeling challenges and proposed solution for characterizing P_t.

Remark 6 *To the best of our knowledge, the closed-form expression for the PDF of P_t is very difficult to obtain. This is because P_t and P_{PT} are correlated and the closed-form CDF of P_{PT} is not available according to Section 5.2. In the literature, some papers [52, 60] have proposed to use the average harvested power as the transmit power for each TX. However, this does not always lead to accurate results. Hence, inspired from the approach in [58], we propose to discretize P_t in* (5.12) *into a finite number of levels. We show that this approximation allows tractable computation of the channel coverage probability. The accuracy of this approximation depends on the number of levels. Our results in Section 5.5.1 show that if we discretize the power level in the log scale, a reasonable level of accuracy is reached with as little as* 10 *levels.*

Remark 7 *From* (5.12)*, we can see that P_t depends on P_{PT}. Hence, the motivation for discretizing P_t in the log scale comes from looking into two important measures of P_{PT}, the skewness and the kurtosis. The skewness and the kurtosis describe the shape of the*

probability distribution of P_{PT}. As presented in [74], the distribution of the aggregate received power is skewed to the right with a heavy tail, because both the skewness and the kurtosis of P_{PT} are much greater than 0 for most cases. Therefore, most of the TXs will be at the lowest power level if we discretize P_t in linear scale. Hence, we discretize the power level in the log scale. This improves the accuracy of the approximation.

Let $N+1$ and w denote the total number of levels and the step size of each level, respectively. They are related by $w = \left(\frac{\min\left(\zeta^{-1} P_1^{\max}, \frac{1-\tau}{\zeta\tau} P_2^{\max}\right) - \gamma_{\mathrm{PT}}}{N} \right)$ dBm. We further define k_n as the portion of TXs whose P_t is at the nth level, i.e.,

$$k_n = \begin{cases} \Pr\left((nw+\gamma_{\mathrm{PT}})\,\mathrm{dBm} \leqslant P_{\mathrm{PT}} < ((n+1)\,w+\gamma_{\mathrm{PT}})\,\mathrm{dBm} \right), & n=0,1,2,...,N-1 \\ \Pr(P_{\mathrm{PT}} \geqslant \min(\zeta^{-1} P_1^{\max}, \frac{1-\tau}{\zeta\tau} P_2^{\max})), & n=N \end{cases}.$$

Combining with the power coverage probability derived in Section 5.2, we can express k_n as

$$k_n = \begin{cases} \mathbb{P}_{\mathrm{cov}}^{P}((nw+\gamma_{\mathrm{PT}})\mathrm{dBm}) - \mathbb{P}_{\mathrm{cov}}^{P}(((n+1)\,w+\gamma_{\mathrm{PT}})\,\mathrm{dBm}), & n=0,1,2,...,N-1 \\ \mathbb{P}_{\mathrm{cov}}^{P}\left(\min\left(\frac{P_1^{\max}}{\zeta}, \frac{1-\tau}{\zeta\tau} P_2^{\max}\right)\right), & n=N \end{cases}. \tag{5.13}$$

The above expression allows us to determine the portion of TXs whose P_t is at the nth level. The transmit power for the active TX at the nth level is

$$P_t^n = \left(\zeta \frac{\tau}{1-\tau} 10^{\frac{nw+\gamma_{\mathrm{PT}}-30}{10}} \right) \mathrm{W}. \tag{5.14}$$

The next step is to decide how to model the locations of the TXs whose P_t is at the nth level. This is discussed in the remark below.

Remark 8 *In general, the location and the transmit power of an active TX are correlated, i.e., a TX has higher chance to be activated and transmits with a larger power, if its location is closer to a PB. However, it is not easy to identify and fit a spatial point process with local clustering to model the location of active TXs [54, 57]. For analytical tractability, we assume that the location and the transmit power of an active TX are independent, i.e., a TX in ϕ_t can have a transmit power of P_t^n with probability k_n independently of other TXs. Therefore, using the thinning theorem, we interpret*

the active TX at the nth level as an independent homogeneous PPP with node density $\lambda_t^n = k_n\lambda_t$, denoted as ϕ_t^n. The accuracy of this approximation will be validated in Section 5.5.1.

5.3.2 Channel Coverage Probability

Given that the desired TX is active, the instantaneous SINR at the reference RX, Y_0, is given as

$$\mathsf{SINR} = \frac{P_{X_0} D_0 h_0 PL(d_0)}{\sum_{X_i \in \phi_{\text{active}}} P_{X_i} D_{i0} h_{i0} PL(X_i) + \sigma^2}, \tag{5.15}$$

where h_0 and h_{i0} denote the fading power gains on the reference link and the ith interference link respectively, D_0 and D_{i0} denote the beamforming antenna gain at the RX from its reference TX and the ith interfering TX respectively and σ^2 is the AWGN power. P_{X_0} and P_{X_i} are the transmit power for the reference TX and the active TX X_i, respectively. Using (5.15), the channel coverage probability is defined as follows:

Definition 3 *The channel coverage probability is the probability that the SINR at the reference RX is above a threshold γ_{TR} and can be expressed as*

$$\mathbb{P}_{\text{cov}}^{C}(\gamma_{\text{TR}}) = \Pr(\mathsf{SINR} > \gamma_{\text{TR}}). \tag{5.16}$$

Remark 9 *It is possible to employ the numerical inversion method in Section 5.2 to find the channel coverage probability. In doing so, the Laplace transform of the term $\frac{I_X+\sigma^2}{P_{X_0} D_0 h_0 PL(d_0)}$ is required. This Laplace tranform cannot be expressed in closed-form because of the random variables P_{X_0} and h_0 in the denominator. Although it is still computable, it leads to greater computation complexity. Consequently, we employ the reference link power gain based method in [86] to efficiently find the channel coverage probability. The basic principle of this approach is to first find the conditional outage probability in terms of the CDF of the reference link's fading power gain and then remove the conditioning on the fading power gains and locations of the interferers, respectively. In order to apply this method, the reference TX-RX link is assumed to undergo Nakagami-m fading with integer m. The result for the conditional channel coverage probability is presented in the following proposition.*

Proposition 6 *Following the system model in Section 5.1, the conditional channel coverage probability at the reference RX in a mmWave ad hoc network is*

$$\mathbb{P}_{\text{cov}}^{C}(\gamma_{\text{TR}}) = \sum_{n=0}^{N}\sum_{l=0}^{m-1}\frac{(-s)^l}{l!}\frac{dl}{ds^l}\mathcal{L}_{I_X+\sigma^2}(s)\frac{k_n}{\mathbb{P}_{\text{cov}}^{P}(\gamma_{\text{PT}})}, \tag{5.17}$$

where $I_X = \sum_{n=0}^{N}\sum_{X_i\in\phi_t^n} P_t^n D_{i0} h_{i0} PL(X_i)$ *and* $s = \frac{m\gamma_{\text{TR}}}{P_t^n D_0 l(d_0)}$.

Proof: See Appendix D.1. ■

(5.17) needs the Laplace transform of the interference plus noise. Using stochastic geometry, we can derive it and the result is shown in the following corollary.

Corollary 1 *Following the system model in Section 5.1 and the discretization assumption in Section 5.3.1, the Laplace transform of the aggregate interference plus noise at the reference RX in a mmWave ad hoc network is*

$$\begin{aligned}\mathcal{L}_{I_X+\sigma^2}(s) = &\prod_{n=0}^{N}\prod_{k=1}^{4}\exp\Big(\pi\lambda_t^n R_{min}^2 q_k\Big(m^m(m+sR_{min}^{-\alpha_{\text{L}}}P_t^n D_k)^{-m}-1\Big)\\
&+\pi\lambda_t^n q_k\left(sP_t^n D_k\right)^{\delta_{\text{L}}}\left(\Xi_1'(1)-\Xi_1'(R_{min})\right)+\pi\lambda_t^n q_k sP_t^n D_k\beta\left(\Xi_2'(R_{min})-\Xi_2'(R_{max})\right)\\
&+\frac{\pi\lambda_t^n}{2+\alpha_{\text{N}}}q_k(sP_t^n D_k\beta)^{\delta_{\text{N}}}\left(\Xi_3'(R_{min})-\Xi_3'(R_{max})\right)\Big)\exp(-s\sigma^2),\end{aligned} \tag{5.18}$$

where

$$\Xi_1'(r) = \frac{m^{m+1}(r^{-\alpha_{\text{L}}}sP_t^n D_k)^{-\delta_{\text{L}}-m}}{(\delta_{\text{L}}+m)}\,{}_2F_1\left(1+m,m+\delta_{\text{L}};1+m+\delta_{\text{L}};-\frac{mr^{\alpha_{\text{L}}}}{sP_t^n D_k}\right), \tag{5.19}$$

$$\Xi_2'(r) = \frac{r^2}{r^{\alpha_{\text{N}}}+sP_t^n D_k\beta}, \tag{5.20}$$

$$\begin{aligned}\Xi_3'(r) = &\frac{(r^{-\alpha_{\text{N}}}sP_t^n D_k\beta)^{-\delta_{\text{N}}-1}}{r^{\alpha_{\text{N}}}+sP_t^n D_k\beta}\Big(sP_t^n D_k\beta(2+\alpha_{\text{N}})\\
&-2(r^{\alpha_{\text{N}}}+sP_t^n D_k\beta)\,{}_2F_1\left(1,\delta_{\text{N}}+1;2+\delta_{\text{N}};-\frac{r^{\alpha_{\text{N}}}\beta^{-1}}{sP_t^n D_k}\right)\Big).\end{aligned} \tag{5.21}$$

Proof: Following the definition of Laplace transform, we have

$$\begin{aligned}\mathcal{L}_{I_X+\sigma^2}(s) =&\mathbb{E}_{I_X}[\exp(-s(I_X+\sigma^2))]\\
=&\mathbb{E}_{I_X}[\exp(-sI_X)]\exp(-s\sigma^2)\\
=&\mathcal{L}_{I_X}(s)\exp(-s\sigma^2),\end{aligned} \tag{5.22}$$

where the Laplace transform of the aggregate interference can be expressed as

$$\begin{aligned}\mathcal{L}_{I_X}(s) =& \mathbb{E}_{I_X}[\exp(-sI_X)] = \mathbb{E}_{D_{i0},h_{i0},\phi_t^n}\left[\exp\left(-s\sum_{n=0}^{N}\sum_{X_i\in\phi_t^n} P_t^n D_{i0} h_{i0} PL(X_i)\right)\right] \\ =& \prod_{n=0}^{N} \mathbb{E}_{D_{i0},h_{i0},\phi_t^n}\left[\exp\left(-s\sum_{X_i\in\phi_t^n} P_t^n D_{i0} h_{i0} PL(X_i)\right)\right]. \end{aligned} \tag{5.23}$$

Then, following the same steps as the proof of the Laplace transform of the aggregate received power, we can find the expectation in (5.23) and arrive at the result in (5.18). ■

The Laplace transform shown in Corollary 1 is in closed-form. Substituting (5.18) into (5.17), we can easily compute the conditional channel coverage probability. Note that (5.17) requires higher order derivatives of the Laplace transform of the interference plus noise $\frac{dl}{ds^l}\mathcal{L}_{I_X+\sigma^2}(s)$, which can be yielded in closed-form using chain rules and changing variables. For brevity, the details are omitted here.

5.4 Total Coverage Probability

As discussed in Section 5.1.5, the event that the information can be successfully delivered to RX has two requirements, i.e., satisfying power coverage and channel coverage. Based on our definition, the total coverage probability is

$$\begin{aligned}\mathbb{P}_{\text{cov}}(\gamma_{\text{PT}},\gamma_{\text{TR}}) &= \Pr(\text{TX is in power coverage \& RX is in channel coverage}) \\ &= \Pr(\text{TX is in power coverage}) \\ &\times \Pr(\text{RX is in channel coverage} \mid \text{TX is in power coverage})\end{aligned}$$

Combining our analysis presented in Section 5.2 and 5.3, we have

$$\begin{aligned}\mathbb{P}_{\text{cov}}(\gamma_{\text{PT}},\gamma_{\text{TR}}) =& \mathbb{P}^P_{\text{cov}}(\gamma_{\text{PT}})\mathbb{P}^C_{\text{cov}}(\gamma_{\text{TR}}) \\ =& \sum_{n=0}^{N}\sum_{l=0}^{m-1}\frac{(-s)^l}{l!}\frac{dl}{ds^l}\mathcal{L}_{I_X+\sigma^2}(s)k_n,\end{aligned} \tag{5.24}$$

where $s = \frac{m\gamma_{\text{TR}}}{P_t^n D_0 l(d_0)}$, $\mathcal{L}_{I_X+\sigma^2}(s)$ is given in Corollary 1, k_n is presented in (5.13), which is determined by the power coverage probability. The key metrics are summarized in Table 5.2.

Table 5.2: Summary of the Analytical Model for PB-assisted mmWave Ad Hoc Networks.

Performance metrics	General form	Key factor(s)
Power coverage probability	(5.7)	$\mathcal{L}_{P_{\mathrm{PT}}}(s)$ in (5.8)
Channel coverage probability	(5.17)	$\mathbb{P}^{p}_{\mathrm{cov}}(\gamma_{\mathrm{PT}})$ in (5.7) $\mathcal{L}_{I_X+\sigma^2}(s)$ in (5.18)
Total coverage probability	(5.24)	$\mathbb{P}^{p}_{\mathrm{cov}}(\gamma_{\mathrm{PT}})$ in (5.7) $\mathcal{L}_{I_X+\sigma^2}(s)$ in (5.18)

Table 5.3: Parameter Values.

Parameter	Value	Parameter	Value
λ_p	50 /km^2	m	5
λ_t	100 /km^2	$G_p^{\max}$, $G_p^{\min}$, θ_p	[20 dB, -10 dB, 30$^{\mathrm{o}}$]
d_0	20 m	$G_t^{\max}$, $G_t^{\min}$, θ_t	[10 dB, -10 dB, 45$^{\mathrm{o}}$]
$R_{\min}$	100 m	$G_r^{\max}$, $G_r^{\min}$, θ_r	[10 dB, -10 dB, 45$^{\mathrm{o}}$]
$R_{\max}$	200 m	σ^2	-30 dBm
α_{L}	2	τ	0.5
α_{N}	4	ζ	0.5
P_p	40 dBm	γ_{PT}	-20 dBm
$P_1^{\max}$	20 dBm	γ_{TR}	30 dBm
$P_2^{\max}$	30 dBm	N	10

5.5 Results

In this section, we first validate the proposed model and then discuss the design insights provided by the model. Unless stated otherwise, the values of the parameters summarized in Table 5.3 are used. The chosen values are consistent with the literature in mmWave and WPT [13, 68, 69]. Note that the values of $R_{\min}$ and $R_{\max}$ correspond to 28 GHz mmWave carrier frequency [68]. Larger transmission bandwidths in mmWave networks increase the impact of thermal noise [69, 108]. We mainly focus on illustrating the results for total coverage probability and channel coverage probability. As for the power coverage probability, it will be explained within the text.

Table 5.4 summarizes the impact of varying the important system parameters[4], i.e., SINR threshold γ_{TR}, PB density λ_p, TX density λ_t, PB transmit power P_p, radius of the LOS region $R_{\min}$, power circuit activation threshold γ_{PT}, the beam-width of the main lobe of TX θ_t, RX's main lobe beam-width θ_r, allowed maximum harvested power at active TX $P_1^{\max}$, time switching parameter τ and TX maximum transmit

[4]Note that the trends reported in Table 5.4 remain the same for a two-state blockage model.

Table 5.4: Effect of Important System Parameters.

Parameter	Power coverage	Channel coverage	Total coverage
Increasing γ_{TR}	-	$\downarrow$	$\downarrow$
Increasing λ_p	$\uparrow$	$\downarrow\uparrow$	$\uparrow$
Increasing λ_t	-	$\downarrow$	$\downarrow$
Increasing P_p	$\uparrow$	$\uparrow$	$\uparrow$
Increasing $R_{\min}$	$\uparrow$	$\uparrow$	$\uparrow$
Increasing γ_{PT}	$\downarrow$	$\uparrow$	$\downarrow$
Increasing θ_t and θ_r	$\uparrow$	$\downarrow$	$\downarrow$
Increasing $P_1^{\max}$	-	$\uparrow\downarrow$	$\uparrow\downarrow$
Increasing τ	-	$\uparrow$	$\uparrow$
Increasing $P_2^{\max}$	-	$\downarrow$	$\downarrow$

power $P_2^{\max}$ on the three network performance metrics. In Table 5.4, $\uparrow$, $\downarrow$ and - denote increase, decrease and unrelated, respectively. $\uparrow\downarrow$ represents that the performance metric first increases then decreases with the system parameter. Please note that the trends in Table 5.4 originate from the analysis of the numerical results, which is presented in detail in the following subsections.

5.5.1 Model Validation

In this section, we validate the proposed model for the channel coverage probability and the total coverage probability. Figure 5.2 plots the channel coverage probability and the total coverage probability for a reference RX against SINR threshold for different densities of PBs and TXs. The analytical results are obtained using Proposition 6 and (5.24) with 10 discrete levels for P_t. The simulation results are generated by averaging over 10^8 Monte Carlo simulation runs and do not assume any discretization of power levels.

From the figure, we can see that our analytical results provide a good approximation to the simulation. The small gap between them comes from two reasons: (i) discretization of the power levels, as discussed in Remark 7, and (ii) ignorance of the correlation between the location and the transmit power of active TX, as discussed in Remark 8. From Figure 5.2, we can see that the gap between the simulation and the analytical results is smaller, when γ_{TR} is higher. At $\gamma_{\mathrm{TR}} = 30$ dBm, which is a typical SINR threshold, the relative errors between the proposed model and the simulation results for both channel coverage probability and total coverage probability are between

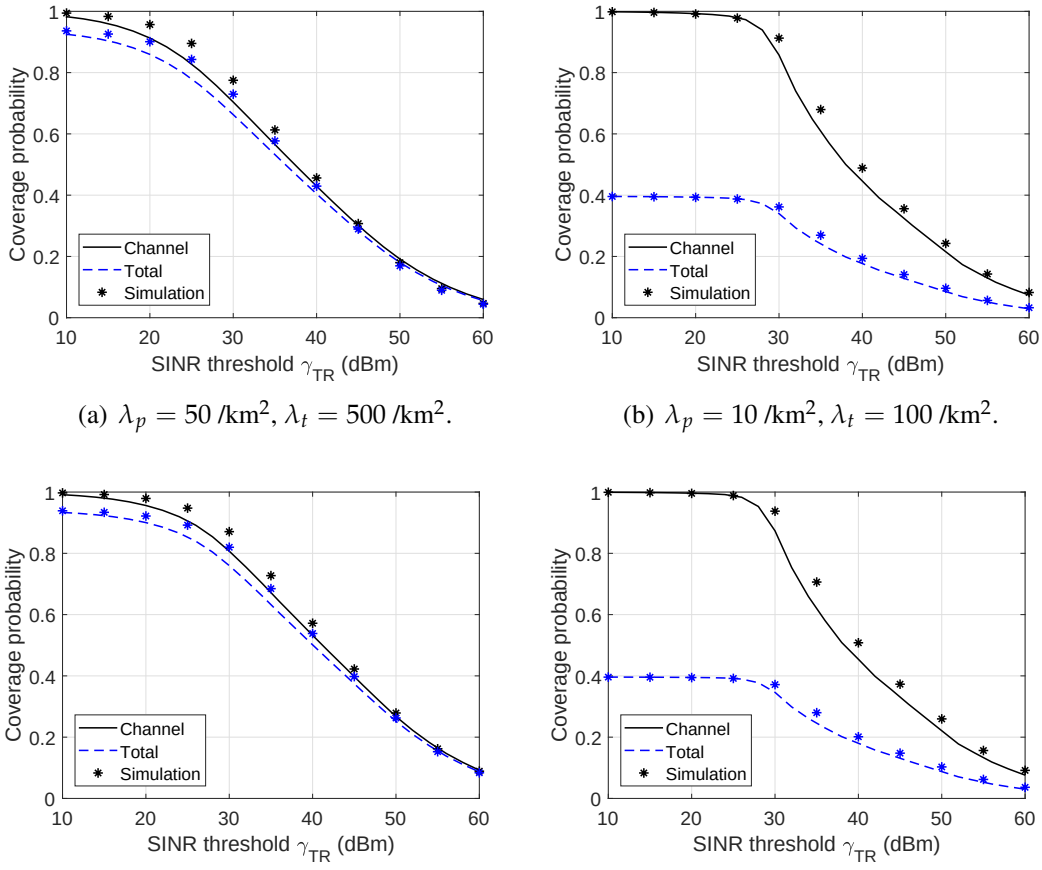

(a) $\lambda_p = 50$ /km^2, $\lambda_t = 500$ /km^2.

(b) $\lambda_p = 10$ /km^2, $\lambda_t = 100$ /km^2.

(c) $\lambda_p = 50$ /km^2, $\lambda_t = 250$ /km^2.

(d) $\lambda_p = 10$ /km^2, $\lambda_t = 50$ /km^2.

Figure 5.2: Channel coverage probability and total coverage probability versus SINR threshold γ_{TR}. The PB density is 50 and 10 per km^2 and the TX density is 500, 100, 250 and 50 per km^2.

5% to 10%. This validates the use of 10 discrete levels for P_t, which provides good accuracy. With more levels of discretization, i.e., larger N, better accuracy can be achieved.

Insights: Comparing the four cases for the different PB and TX densities, Figure 5.2 shows that: (i) The channel coverage probability decreases while the total coverage probability increases as PB density increases. As the PB density increases, the aggregate received power at TX increases as well as the number of active TXs. Therefore, interfering power received by the RX is higher and the channel coverage probability decreases. However, the total coverage probability increases because the power coverage probability increases with the PB density. (ii) When the PB density is

low, the TXs are very likely to be inactive and the total coverage probability is dominated by the power coverage probability. When the PB density is high, the TXs are very likely to be active. Hence, the interference is strong and the channel coverage probability dominates the total coverage probability. (iii) For the same PB density, both the total coverage probability and the channel coverage probability are higher, when the TX density is lower. This is because more interfering TXs exist if TX density increases.

5.5.2 Effect of PB Transmit Power

Figure 5.3(a) illustrates the effect of PB transmit power P_p on the total coverage probability and channel coverage probability, with different radius of the LOS region $R_{\min} = 50\text{m}, 100\text{m}$. The simulation results are also plotted in the figure, which are averaged over 10^8 Monte Carlo simulation runs. The accuracy is between 3% to 8%, which again validates the proposed model. Hence, in the subsequent figures in the chapter we only show the analytical results and discuss the insights.

Figure 5.3(b) plots the total coverage probability against the transmit power of PB. We also plot an asymptotic result when P_p approaches infinity. This result is obtained as follows. As P_p approaches infinity, if one or more PBs fall into the LOS or NLOS region of a TX, this TX will be active and transmit with a power of $P_t = \min(\frac{\tau}{1-\tau}P_1^{\max}, P_2^{\max})$. Hence, the asymptotic power coverage probability is equivalent to the probability that at least one PB falls into the LOS or NLOS region of the TX, which is given by

$$\lim_{P_p\to\infty} \mathbb{P}_{\text{cov}}^{P} = 1 - \exp\left(-\pi\lambda_p R_{\max}^2\right). \tag{5.25}$$

The asymptotic conditional channel coverage probability and the asymptotic total coverage probability can be found by (5.17) and (5.24) respectively with the portion of TXs at the nth level as

$$\lim_{P_p\to\infty} k_n = \begin{cases} 0, & n = 0, 1, 2, ..., N-1 \\ \mathbb{P}_{\text{cov}}^{P}, & n = N \end{cases}. \tag{5.26}$$

From the figure, we can see that the analytical and asymptotic results converge as P_p gets large, which validates the derivation of the asymptotic results. In addition, in Figure 5.3(b), we have marked the safe RF exposure region with a PB transmit power

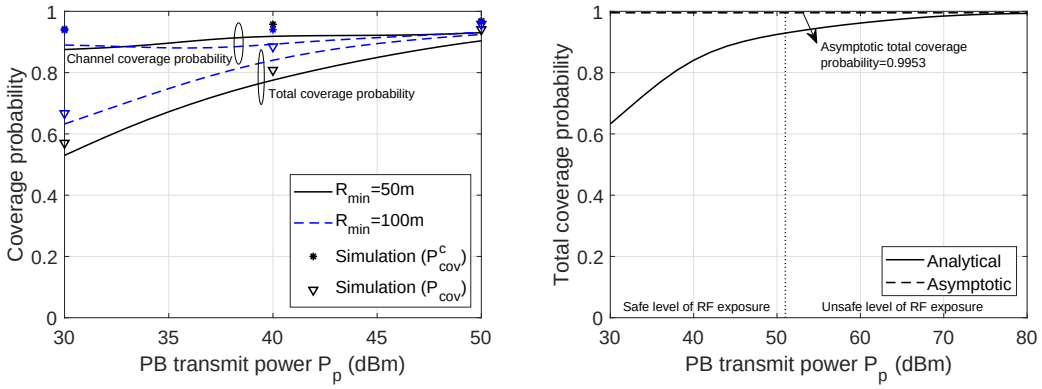

(a) Channel coverage and total coverage with different $R_{\min}$.

(b) Total coverage and asymptotic total coverage.

Figure 5.3: Coverage probabilities versus PB transmit power P_p.

less than 51 dBm, equivalently power density smaller than 10 W/m^2 at 1 m from the PB [88]. We will discuss in detail later in the feasibility study in Section 5.5.5.

Insights: Figure 5.3(a) shows that: (i) The channel coverage probability first slightly decreases and then increases with the increase of P_p. This can be explained as follows. At first, both the transmit power of the desired TX and the number of interfering TX increase with P_p. The interplay of this two factors results in the slightly decreasing trend for the channel coverage probability. As P_p further increases, the increase in the number of interfering TX is negligible, while the transmit power of the desired TX continues to increase, which leads to the increase of the channel coverage probability. (ii) The total coverage probability increases as PB transmit power P_p increases. When P_p is small, the desired TX might not receive enough power to activate the information transmission process. So the total coverage probability is small and is limited by the power coverage probability. When P_p is large, the channel coverage probability becomes the dominant factor in determining the total coverage probability. Hence, eventually the channel coverage probability and total coverage probability curves merge. (iii) The total coverage probability increase with $R_{\min}$, because more PBs falls into the LOS region and the path-loss is less severe, which improves the power coverage probability. The benefit of increasing the radius of the LOS region is less significant for the channel coverage probability.

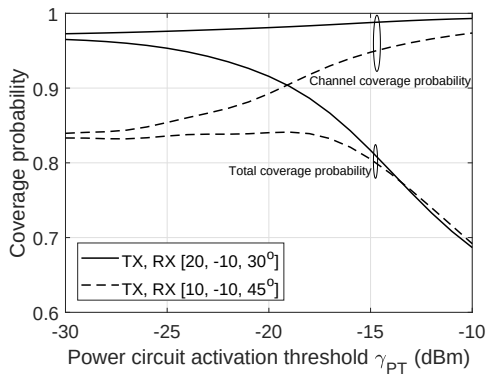

Figure 5.4: Channel coverage probability and total coverage probability versus power circuit activation threshold γ_{PT} with different TX and RX beamforming parameters.

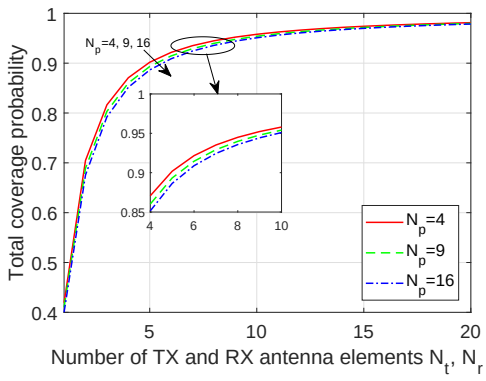

Figure 5.5: Total coverage probability versus the numbers of antenna elements at TX and RX $\mathcal{N}_t$ and $\mathcal{N}_r$ with different numbers of antenna elements at PB.

5.5.3 Effect of Directional Beamforming at PB, TX and RX

Figure 5.4 plots the total coverage probability and channel coverage probability against the power circuit activation threshold of TX for different beamforming parameters at TX and RX, i.e., [20 dB, -10 dB, 30^{o}] and [10 dB, -10 dB, 45^{o}].

Insights: Figure 5.4 shows that, for both sets of beamforming parameters, as the power circuit activation threshold γ_{PT} increases, the channel coverage probability is always increasing, while the total coverage probability stays roughly the same at first and then decreases. This can be explained as follows. When γ_{PT} increases, the power coverage probability decreases. The reduction in the number of active TXs improves the channel coverage probability. With regards to the total coverage probability, its trend is determined by the interplay of channel coverage probability and power coverage probability. At first, the drop in power coverage is relatively small as shown in Figure 5.1; so the total coverage probability is almost unchanged. After a certain point, the power coverage probability drops a lot, which mainly governs the total coverage probability. Hence, the total coverage probability decreases later on.

Comparing the curves for the different beamforming parameters, we can see that TX and RX with [20 dB, -10 dB, 30^{o}] gives a higher total coverage probability in the low power circuit activation threshold region. This is because a narrower main lobe beam-width gives a larger main lobe gain and makes less interfering TXs fall into its

main lobe which results in higher channel coverage probability. However, the total coverage probability is limited by the power coverage probability when γ_{PT} is large.

Impact of number of antenna elements: The beamforming model adopted in this chapter can be related to any specific array geometry by substituting the appropriate values for the three beamforming parameters. For instance, a uniform planar square array with half-wavelength antenna element spacing can be used at the PBs, TXs and RXs. The values for the main lobe antenna gain $G_a^{\max}$, side lobe antenna gain $G_a^{\min}$ and main lobe beamwidth θ_a depend on the number of the antenna elements $\mathcal{N}_a$ and can be calculated by using the equations below [70]:

$$G_a^{\max} = \mathcal{N}_a, G_a^{\min} = \frac{\sqrt{\mathcal{N}_a} - \frac{\sqrt{3}}{2\pi}\mathcal{N}_a \sin(\frac{\sqrt{3}}{2\sqrt{\mathcal{N}_a}})}{\sqrt{\mathcal{N}_a} - \frac{\sqrt{3}}{2\pi}\sin(\frac{\sqrt{3}}{2\sqrt{\mathcal{N}_a}})}, \theta_a = \frac{\sqrt{3}}{\sqrt{\mathcal{N}_a}}, \tag{5.27}$$

where $a = p$ for PB, $a = t$ for TX and $a = r$ for RX.

Figure 5.5 plots the total coverage probability versus the numbers of antenna elements at the TX and RX $\mathcal{N}_t$ and $\mathcal{N}_r$ with different PB antenna element number $\mathcal{N}_p$. The figure shows that the total coverage probability increases with the numbers of antenna elements at the TX and RX, which agrees with our previous findings. However, under our considered system parameters, the total coverage probability stays roughly the same after having more than about 15 TX and RX antenna elements, as the side lobe antenna gain and the main lobe beamwidth stay almost constant with further increase in the number of antenna elements. In addition, the number of antenna elements at the PB does not significantly impact the total coverage probability.

5.5.4 Effect of Allowed Maximum Harvested Power at TX

Figure 5.6 plots the total coverage probability and channel coverage probability against the allowed maximum harvested power of TX $P_1^{\max}$ for different time switching ratios 0.2, 0.5 and 0.8. Note that both the time switching ratio and the allowed maximum harvested power do not affect the power coverage probability.

Insights: Figure 5.6 shows that the channel coverage probability and the total coverage probability both first increase with $P_1^{\max}$, then decrease. The rise of the channel coverage probability is because the possible transmit power of the desired TX increases with its allowed maximum harvested power. However, as $P_1^{\max}$ further increases, the accumulated harvested energy during the power transfer phase is higher and the trans-

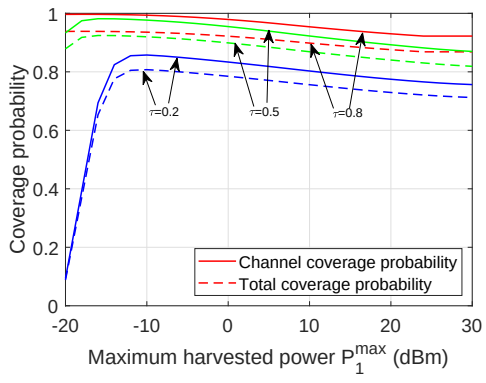

Figure 5.6: Channel coverage probability and total coverage probability versus allowed maximum harvested power $P_1^{\max}$ with different time switching ratios.

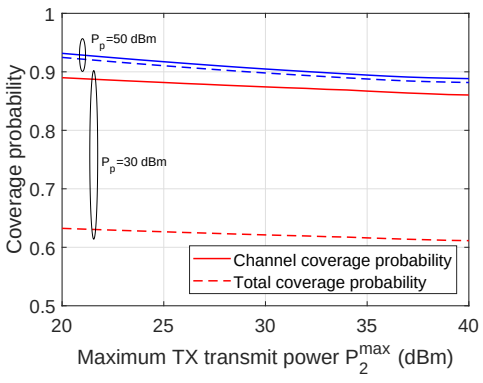

Figure 5.7: Channel coverage probability and total coverage probability versus maximum TX transmit power $P_2^{\max}$ for different PB transmit power with the allowed maximum harvested power of TX being 50 dBm.

mit power of other active TX also goes up. As a result, the interfering power received at the RX is higher and the channel coverage probability decreases. The channel coverage probability will converge to a constant value as $P_1^{\max}$ increases even further, because the maximum transmit power of active TX has limited the channel performance.

Comparing the curves for different τ, we can see that for a given maximum harvested power of TX $P_1^{\max}$, increasing τ improves the coverage probabilities. When τ is higher, more energy is captured during the power transfer phase. Therefore, the transmit power of active TX is now limited by the maximum transmit power $P_2^{\max}$. As a result, the channel coverage probability and total coverage probability converge and do not vary much with the changes in the allowed maximum harvested power.

5.5.5 Feasibility of PB-assisted mmWave Wireless Ad hoc Networks

Finally, we investigate the feasibility of PB-assisted mmWave wireless ad hoc network. Figure 5.7 is a plot of the total coverage probability and channel coverage probability versus maximum TX transmit power $P_2^{\max}$ with varied PB transmit power, 50 dBm and 30 dBm. To better highlight the impact of the maximum transmit power at TX,

we have set $P_1^{\max}$ equal to 50 dBm which is much higher than $P_2^{\max}$. From the figure, we can see that the channel coverage probability and total coverage probability do not change much with the considered maximum TX transmit power, which means that the PMF of the transmit power for the desired TX remains almost the same. Note that the power coverage probability is independent of the maximum transmit power of TX.

Insight: From Figure 5.7, the total coverage probability and the channel coverage probability are around 90% if P_p is 50 dBm. If PB transmits with a constant power of 50 dBm, the power density at a distant of 1 m from the PB is 7.95 $\mathrm{W/m^2}$. This power density is smaller than 10 $\mathrm{W/m^2}$, which is the permissible safety level of human exposure to RF electromagnetic fields based on IEEE Standard. Under this safety regulation, the maximum permissible PB transmit power would be 51 dBm. We have marked this value in Figure 5.3(b). From Figure 5.3(b), we can see that the total coverage probability with a PB transmit power less than 51 dBm can be up to 93.4% of the maximum system performance, as given by the asymptotic analysis in Section 5.5.2, based on our considered system parameters. The results in Figure 5.3(b) and Figure 5.7 show that PB-assisted mmWave ad hoc networks are feasible under practical network setup.

5.6 Summary

In this chapter, we have presented an approximate yet accurate model for PB-assisted mmWave wireless ad hoc networks, where TXs harvest energy from all PBs and then use the harvested energy to transmit information to their corresponding RXs. We first obtained the Laplace transform of the aggregate received power at the TX to compute the power coverage probability. Then, the channel coverage probability and total coverage probability were formulated based on discretizing the transmit power of TXs into a finite number of levels. The simulation results confirmed the accuracy of the proposed model. The results have shown that the total coverage probability improves by increasing the transmit power of PB, narrowing the main lobe beam-width and decreasing the allowed maximum harvested power at the active TX. Our results also showed that PB-assisted mmWave ad hoc network is feasible under realistic setup conditions.

Chapter 6

Conclusions and Future Research Directions

In this chapter, we summarize the general conclusions drawn from this thesis. We also outline some future research directions arising from this work.

6.1 Conclusions

This thesis has investigated two critical requirements for beyond 5G wireless communication networks, which are network flexibility and long battery life. We provided insights on how these two emerging requirements can be achieved by incorporating drone communication and WPT into the wireless communication systems.

The first half of this thesis focused on studying two important applications of drones for enhancing the flexibility of communication networks. In Chapter 2, a cellular network with underlay drone cell to provide coverage to IoT devices inside a stadium was considered for temporary event scenarios. We developed a general analytical framework to analyze the uplink coverage probability of the TBS and the ABS and the downlink coverage probability of the TsUE and the AsD in terms of the Laplace transforms of the interference power distribution at the TBS, the ABS, the TsUE and the AsD and the three-dimensional distance distribution between the ABS and an i.u.d. AsD and between the ABS and an i.u.d. TsUE. The proposed framework is able to accommodate any aerial channel model. Our results revealed the effect of different aerial channel environments on the network performance and provided design guidelines for best deployment altitude of the drone. For urban environment and dense urban environment, the ABS was found to be best deployed at 200 m or lower regardless of the distance between the center of the stadium and the TBS. However, for suburban environment and high-rise urban environment, the best ABS deloyment

altitude depends on the distance between the center of the stadium and the TBS.

In Chapter 3, we explored another use case for drones in wireless networks, which is emergency information dissemination in public safety scenarios. A drone-assisted multihop multicast D2D network was considered where a drone is depolyed to broadcast an emergency alert message to all terrestrial D2D users at the first time slot. After that, the drone leaves and the D2D users that have successfully received the message become the active TX for the next time slot to multicast the emergency alert message. We studied the link coverage probability and the mean local delay for a D2D user. We derived the key factors that determine the link performance, the link success probability, the network outage probability and the Laplace transform of the aggregate received signal power. An approximate analytical framework for the link success probability, the network success probability and the network coverage probability was proposed and its accuracy was verified by the simulation results. Our results illustrated that raising the deployment height and the transmit power of the drone and increasing the density and the sensitivity radius of the D2D users lead to higher link coverage probability and network coverage probability and lower mean local delay.

The second half of this thesis looked into WPT networks. A PB-assisted wireless ad hoc network under mmWave transmission was considered, where TXs adopt the harvest-then-transmit protocol, i.e., they harvest energy from all PBs and then use the harvested energy to transmit the information to their desired RXs. In Chapter 4, we studied the characteristic of the aggregate received power by deriving the MGF and the nth cumulant of the aggregate received power at the reference TX. The aggregate received power plays a key role in determining the overall network performance, which was discussed in Chapter 5. Furthermore, we tested the accuracy of well known closed-form distributions to model the aggregate received power and found that the lognormal distribution provides the best CCDF approximation compared to other distributions commonly considered in the literature.

Finally, in Chapter 5, we proposed a tractable analytical framework to investigate the power coverage probability, the channel coverage probability and the total coverage probability of a PB-assisted mmWave ad hoc network taking the power circuit activation threshold, the allowed maximum harvested power and the maximum transmit power into account. In the proposed framework, the power coverage probability was efficiently and accurately computed by numerical inversion using the Laplace transform of the aggregate received power at the typical TX. Then, we expressed the channel coverage probability and the total coverage probability by discretizing the transmit

power of TXs into a finite number of levels in the log scale. Our results showed that the total coverage probability improves by (i) increasing the transmit power of PB, (ii) narrowing the main lobe beam-width and (iii) decreasing the allowed maximum harvested power at the active TX. Our results also revealed that it is feasible and safe to power TXs in a mmWave ad hoc network using PBs under realistic setup.

6.2 Future Work

A number of future research directions arise from the work presented in this thesis. The following major research directions can be the focus of future work:

Multiple drones: In Chapter 2 and Chapter 3 of this thesis, we considered a single drone acting as a base station or a TX. Due to the maneuverability and the increasing affordability of commercial drones, multiple drones can be deployed at the same time to provide lower latency communications. In this case, user association scheme is a key research problem. Although a drone is closer to the user, it may have a smaller elevation angle which means the link between the drone and the user has a higher chance of being NLOS. Therefore, the classic user association scheme, in which the user is considered to be connected to the base station with the shortest distance, requires a redesign. Resource management is another critical design challenge in the communication systems with multiple drones. In particular, there is a need for developing frameworks to dynamically manage various network resources, including transmit power, load balancing, user scheduling, MAC access protocols and bandwidth and spectrum sharing.

DUEs: Besides the use of drones as ABSs, they can also act as DUEs for different applications. For instance, DUEs play key roles in cargo transport tasks. Amazon is working on providing their customers with a rapid parcel delivery service using drones [109]. Another important application of DUEs is for search and rescue operations, where drones search for and locate the people in distress and transmit the emergency information to terrestrial stations. Incorporating DUEs in the current communication systems introduces new research problems. Specifically, the systems need to be innovated to account for mobility, frequent handovers, strong LOS interference and low latency requirements of drones. Some important open problems include designing dynamic handover algorithms to manage frequent handovers due to mobility of the drones, developing robust interference reduction techniques for large scale deploy-

ment of DUEs and providing effective solutions for meeting the latency requirements of DUEs in different applications.

Visible light WPT: Light emitting diode (LED) is an emerging standard for lighting needs in everyday life. Comparing to compact fluorescent lamps and incandescent light bulbs, LEDs require lower power for their operation and last much longer. An interesting application of these devices is that they can be utilized for data transmission, while also providing illumination. Visible light communication refers to communication in the visible part of the electromagnetic spectrum. In this area, LEDs have a great potential for applications, due to their relatively simple design, energy efficiency and cost effective. In addition to their capability for information transmission, LEDs can be adopted for WPT. A significant feature of LEDs is that the light is directional which forms natural beamforming. Most importantly, the wireless channels between LED TXs and RXs are guaranteed to be LOS links for visible light communication, and hence, the WPT efficiency can be improved. The design consideration and system performance of visible light WPT using LEDs can be the subject of future work.

Wireless powered drones: In practical systems, drones are power-hungry devices. The flight time of small commercial drones is usually 20-30 minutes, while some large drones can spend hours in the air without recharging or refueling. For drone BSs, the onboard power supply is required to support the operation and the payload of both the drone and the additional mounted wireless communication hardware, such as antenna arrays, amplifier and processor. Therefore, the operation duration of drone BSs is further limited. The short flight time of the existing commercial drones is one of the major practical factors which limit the massive deployment of drones in the cellular networks [110]. In order to provide a more reliable communication network with drones without frequent recharging, a promising way is to power the drones by harvesting energy from the RF signal transmitted by PBs on the ground or by satellites. To the best of our knowledge, there are very limited research works considering the use of drones to power ground mobile terminals, but there is no available research work analyzing the performance of wireless powered drones.

Appendix A

This appendix contains the proofs needed in Chapter 2.

A.1 Proof of Lemma 1

Following the definition of the Laplace transform, the Laplace transform of the interference power distribution at the TBS is expressed as

$$\begin{aligned}\mathcal{L}_{I_{\mathrm{T}}^u}(s) &= \mathbb{E}_{I_{\mathrm{T}}^u}[\exp(-sI_{\mathrm{T}}^u)] \\ &= \mathbb{E}_{P,H,d}[\exp(-sP_{\mathrm{AsD}}H_A^u d_A^{-\alpha_{\mathrm{T}}})] \\ &= \mathbb{E}_{P,d}\left[\frac{1}{1+sP_{\mathrm{AsD}}d_A^{-\alpha_{\mathrm{T}}}}\right], \end{aligned} \tag{A.1}$$

where the third step comes from the fact that H_A^u follows exponential distribution with unit mean. Conditioned on the value of h, there are six possible cases for $\mathcal{L}_{I_{\mathrm{T}}^u}(s)$. When $\sqrt{\left(\frac{P_{\mathrm{AsD}}^{\max}\eta_{\mathrm{L}}}{\rho_{\mathrm{A}}}\right)^{\frac{2}{\alpha_{\mathrm{L}}}} - R_2^2} < h < \left(\frac{P_{\mathrm{AsD}}^{\max}\eta_{\mathrm{N}}}{\rho_{\mathrm{A}}}\right)^{\frac{1}{\alpha_{\mathrm{N}}}}$, the Laplace transform of the interference power distribution at the TBS equals to

$$\begin{aligned}\mathcal{L}_{I_{\mathrm{T}}^u}(s) = &\int_h^{\left(\frac{P_{\mathrm{AsD}}^{\max}\eta_{\mathrm{L}}}{\rho_{\mathrm{A}}}\right)^{\frac{1}{\alpha_{\mathrm{L}}}}} \mathbb{E}_d\left[\frac{p_{\mathrm{L}}}{1+s\rho_{\mathrm{A}}z^{\alpha_{\mathrm{L}}}\eta_{\mathrm{L}}^{-1}d_A^{-\alpha_{\mathrm{T}}}}\right] f_{\mathcal{Z}_A}(z)\mathrm{d}z \\ &+ \int_{\left(\frac{P_{\mathrm{AsD}}^{\max}\eta_{\mathrm{L}}}{\rho_{\mathrm{A}}}\right)^{\frac{1}{\alpha_{\mathrm{L}}}}}^{\sqrt{h^2+R_2^2}} \mathbb{E}_d\left[\frac{p_{\mathrm{L}}}{1+sP_{\mathrm{AsD}}^{\max}d_A^{-\alpha_{\mathrm{L}}}}\right] f_{\mathcal{Z}_A}(z)\mathrm{d}z \\ &+ \int_h^{\left(\frac{P_{\mathrm{AsD}}^{\max}\eta_{\mathrm{N}}}{\rho_{\mathrm{A}}}\right)^{\frac{1}{\alpha_{\mathrm{N}}}}} \mathbb{E}_d\left[\frac{p_{\mathrm{N}}}{1+s\rho_{\mathrm{A}}z^{\alpha_{\mathrm{N}}}\eta_{\mathrm{N}}^{-1}d_A^{-\alpha_{\mathrm{T}}}}\right] f_{\mathcal{Z}_A}(z)\mathrm{d}z \end{aligned}$$

$$
\begin{aligned}
&+\int_{\left(\frac{P_{\mathrm{AsD}}^{\max}\eta_{\mathrm{N}}}{\rho_{\mathrm{A}}}\right)^{\frac{1}{\alpha_{\mathrm{N}}}}}^{\sqrt{h^2+R_2^2}} \mathbb{E}_d\left[\frac{p_{\mathrm{N}}}{1+sP_{\mathrm{AsD}}^{\max}d_A^{-\alpha_{\mathrm{N}}}}\right] f_{\mathcal{Z}_A}(z)\mathrm{d}z \\
&=\int_h^{\left(\frac{P_{\mathrm{AsD}}^{\max}\eta_{\mathrm{L}}}{\rho_{\mathrm{A}}}\right)^{\frac{1}{\alpha_{\mathrm{L}}}}} \mathbb{E}_\theta\left[\frac{p_{\mathrm{L}}}{1+\frac{s\rho_{\mathrm{A}}z^{\alpha_{\mathrm{L}}}}{\eta_{\mathrm{L}}\left(z^2-h^2+d^2-2\sqrt{z^2-h^2}d\cos\Theta\right)^{\frac{\alpha_{\mathrm{T}}}{2}}}}\right] f_{\mathcal{Z}_A}(z)\mathrm{d}z \\
&+\int_{\left(\frac{P_{\mathrm{AsD}}^{\max}\eta_{\mathrm{L}}}{\rho_{\mathrm{A}}}\right)^{\frac{1}{\alpha_{\mathrm{L}}}}}^{\sqrt{h^2+R_2^2}} \mathbb{E}_\theta\left[\frac{p_{\mathrm{L}}}{1+\frac{sP_{\mathrm{AsD}}^{\max}}{\left(z^2-h^2+d^2-2\sqrt{z^2-h^2}d\cos\Theta\right)^{\frac{\alpha_{\mathrm{T}}}{2}}}}\right] f_{\mathcal{Z}_A}(z)\mathrm{d}z \\
&+\int_h^{\left(\frac{P_{\mathrm{AsD}}^{\max}\eta_{\mathrm{N}}}{\rho_{\mathrm{A}}}\right)^{\frac{1}{\alpha_{\mathrm{N}}}}} \mathbb{E}_\theta\left[\frac{p_{\mathrm{N}}}{1+\frac{s\rho_{\mathrm{A}}z^{\alpha_{\mathrm{N}}}}{\eta_{\mathrm{N}}\left(z^2-h^2+d^2-2\sqrt{z^2-h^2}d\cos\Theta\right)^{\frac{\alpha_{\mathrm{T}}}{2}}}}\right] f_{\mathcal{Z}_A}(z)\mathrm{d}z \\
&+\int_{\left(\frac{P_{\mathrm{AsD}}^{\max}\eta_{\mathrm{N}}}{\rho_{\mathrm{A}}}\right)^{\frac{1}{\alpha_{\mathrm{N}}}}}^{\sqrt{h^2+R_2^2}} \mathbb{E}_\theta\left[\frac{p_{\mathrm{N}}}{1+\frac{sP_{\mathrm{AsD}}^{\max}}{\left(z^2-h^2+d^2-2\sqrt{z^2-h^2}d\cos\Theta\right)^{\frac{\alpha_{\mathrm{T}}}{2}}}}\right] f_{\mathcal{Z}_A}(z)\mathrm{d}z \qquad \text{(A.2a)} \\
&=\int_h^{\left(\frac{P_{\mathrm{AsD}}^{\max}\eta_{\mathrm{L}}}{\rho_{\mathrm{A}}}\right)^{\frac{1}{\alpha_{\mathrm{L}}}}} \int_0^{2\pi} \mathcal{L}_{I_{\mathrm{T}}^u}\left(s,\frac{\rho_{\mathrm{A}}}{\eta_{\mathrm{L}}}z^{\alpha_{\mathrm{L}}}|\theta,z\right)\frac{p_{\mathrm{L}}}{2\pi}f_{\mathcal{Z}_A}(z)\mathrm{d}\theta\mathrm{d}z \\
&+\int_{\left(\frac{P_{\mathrm{AsD}}^{\max}\eta_{\mathrm{L}}}{\rho_{\mathrm{A}}}\right)^{\frac{1}{\alpha_{\mathrm{L}}}}}^{\sqrt{h^2+R_2^2}} \int_0^{2\pi} \mathcal{L}_{I_{\mathrm{T}}^u}(s,P_{\mathrm{AsD}}^{\max}|\theta,z)\frac{p_{\mathrm{L}}}{2\pi}f_{\mathcal{Z}_A}(z)\mathrm{d}\theta\mathrm{d}z \\
&+\int_h^{\left(\frac{P_{\mathrm{AsD}}^{\max}\eta_{\mathrm{N}}}{\rho_{\mathrm{A}}}\right)^{\frac{1}{\alpha_{\mathrm{N}}}}} \int_0^{2\pi} \mathcal{L}_{I_{\mathrm{T}}^u}\left(s,\frac{\rho_{\mathrm{A}}}{\eta_{\mathrm{N}}}z^{\alpha_{\mathrm{N}}}|\theta,z\right)\frac{p_{\mathrm{N}}}{2\pi}f_{\mathcal{Z}_A}(z)\mathrm{d}\theta\mathrm{d}z \\
&+\int_{\left(\frac{P_{\mathrm{AsD}}^{\max}\eta_{\mathrm{N}}}{\rho_{\mathrm{A}}}\right)^{\frac{1}{\alpha_{\mathrm{N}}}}}^{\sqrt{h^2+R_2^2}} \int_0^{2\pi} \mathcal{L}_{I_{\mathrm{T}}^u}(s,P_{\mathrm{AsD}}^{\max}|\theta,z)\frac{p_{\mathrm{N}}}{2\pi}f_{\mathcal{Z}_A}(z)\mathrm{d}\theta\mathrm{d}z, \qquad \text{(A.2b)}
\end{aligned}
$$

where d_A is expressed in terms of z, h, d, and θ by cosine rule in (A.2a) and (A.2b) is obtained by taking the expectation over Θ, which has a conditional PDF as $f_\Theta(\theta|z) = \frac{1}{2\pi}$ for $h \leqslant z \leqslant \sqrt{R_2^2+h^2}$.

Following similar steps, we can work out the Laplace transform of the interference power distribution at the TBS for the other five cases.

A.2 Proof of Lemma 2

The relation between the length of the AsD to ABS link $\mathcal{Z}_A$ with its projection distance on the ground r_A is $\mathcal{Z}_A = \sqrt{r_A^2 + h^2}$. The distance distribution of the projection distance on the ground is $f_{r_A}(r) = \frac{2r}{R_2^2}$ [111, 112]. Thus, we can get the PDF of $\mathcal{Z}_A$ as

$$f_{\mathcal{Z}_A}(z) = \frac{\mathrm{d}(\sqrt{z^2-h^2})}{\mathrm{d}z} f_{r_A}\left(\sqrt{z^2-h^2}\right) = \frac{z}{\sqrt{z^2-h^2}} \frac{2\sqrt{z^2-h^2}}{R_2^2} = \frac{2z}{R_2^2}. \quad \text{(A.3)}$$

A.3 Proof of Lemma 3

Following the definition of the Laplace transform, the Laplace transform of the interference power distribution at the ABS is expressed as

$$\begin{aligned}
&\mathcal{L}_{I_{\mathrm{A}}^u}(s) = \mathbb{E}_{I_{\mathrm{A}}^u}[\exp(-sI_{\mathrm{A}}^u)] = \mathbb{E}_{P,g,z}[\exp(-sP_{\mathrm{TsUE}} G_T^u P L_a(\mathcal{Z}_T))] \\
&= \mathbb{E}_{d,g,z}[\exp(-s\rho_{\mathrm{T}} d_T^{\alpha_{\mathrm{T}}} G_T^u P L_a(\mathcal{Z}_T))] \\
&= \mathbb{E}_{d,z}\left[\frac{p_{\mathrm{L}} m_{\mathrm{L}}^{m_{\mathrm{L}}}}{(m_{\mathrm{L}} + s\rho_{\mathrm{T}} d_T^{\alpha_{\mathrm{T}}} \mathcal{Z}_T^{-\alpha_{\mathrm{L}}} \eta_{\mathrm{L}})^{m_{\mathrm{L}}}} + \frac{p_{\mathrm{N}} m_{\mathrm{N}}^{m_{\mathrm{N}}}}{(m_{\mathrm{N}} + s\rho_{\mathrm{T}} d_T^{\alpha_{\mathrm{T}}} \mathcal{Z}_T^{-\alpha_{\mathrm{N}}} \eta_{\mathrm{N}})^{m_{\mathrm{N}}}}\right] \quad \text{(A.4a)} \\
&= \mathbb{E}_{\omega,z}\left[p_{\mathrm{L}} m_{\mathrm{L}}^{m_{\mathrm{L}}} \left(m_{\mathrm{L}} + \frac{s\rho_{\mathrm{T}}\eta_{\mathrm{L}}}{\mathcal{Z}_T^{\alpha_{\mathrm{L}}}} \left(\mathcal{Z}_T^2 - h^2 + d^2 - 2\sqrt{\mathcal{Z}_T^2 - h^2} d\cos\Omega\right)^{\frac{\alpha_{\mathrm{T}}}{2}}\right)^{-m_{\mathrm{L}}}\right. \\
&\left. + p_{\mathrm{N}} m_{\mathrm{N}}^{m_{\mathrm{N}}} \left(m_{\mathrm{N}} + \frac{s\rho_{\mathrm{T}}\eta_{\mathrm{N}}}{\mathcal{Z}_T^{\alpha_{\mathrm{N}}}} \left(\mathcal{Z}_T^2 - h^2 + d^2 - 2\sqrt{\mathcal{Z}_T^2 - h^2} d\cos\Omega\right)^{\frac{\alpha_{\mathrm{T}}}{2}}\right)^{-m_{\mathrm{N}}}\right] \quad \text{(A.4b)} \\
&= \int_{\sqrt{R_2^2+h^2}}^{\sqrt{(R_1-d)^2+h^2}} \int_0^{2\pi} \mathcal{L}_{I_{\mathrm{A}}^u}(s|\omega,z) f_\Omega(\omega|z) f_{\mathcal{Z}_T}(z)\mathrm{d}\omega\mathrm{d}z \\
&+ \int_{\sqrt{(R_1-d)^2+h^2}}^{\sqrt{(R_1+d)^2+h^2}} \int_{-\widehat{\omega}}^{\widehat{\omega}} \mathcal{L}_{I_{\mathrm{A}}^u}(s|\omega,z) f_\Omega(\omega|z) f_{\mathcal{Z}_T}(z)\mathrm{d}\omega\mathrm{d}z,
\end{aligned}$$

where (A.4a) comes from the fact that G_T^u follows Gamma distribution with parameter m_{L} and m_{N} for LOS and NLOS aerial link respectively. In (A.4b), d_T is expressed in terms of $\mathcal{Z}_T$, h, d, and Ω by cosine rule.

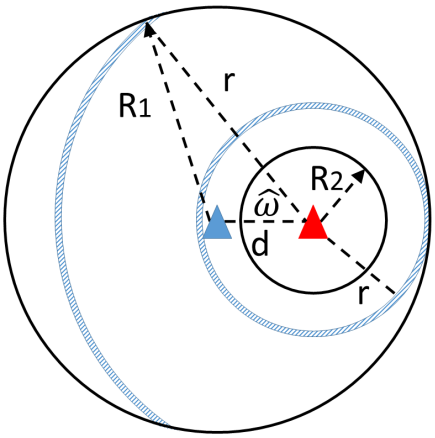

Figure A.1: Illustration of a disk region of radius R_1 with a circular hole with radius R_2. Their centers are d apart.

A.4 Proof of Lemma 4

The relation between the length of the TsUE to ABS link $\mathcal{Z}_T$ with its projection distance on the ground r_T is $\mathcal{Z}_T = \sqrt{r_T^2 + h^2}$. In order to find the distance distribution of $\mathcal{Z}_T$, the distance distribution of r_T is needed. As shown in Figure A.1, the total area of the region where the TsUE is located at is $\pi R_1^2 - \pi R_2^2$. When $R_2 \leqslant r_T \leqslant R_1 - d$, the TsUE falls onto the ring. Therefore, the distance distribution is $f_{r_T}(r) = \frac{2\pi r}{\pi R_1^2 - \pi R_2^2} = \frac{2r}{R_1^2 - R_2^2}$. When $R_1 - d < r_T \leqslant R_1 + d$, the TsUE lies in the arc. The distance distribution is $f_{r_T}(r) = \frac{2\hat{\omega} r}{\pi R_1^2 - \pi R_2^2}$. Based on cosine rule, $\hat{\omega} = \arccos\left(\frac{d^2 + r^2 - R_1^2}{2dr}\right)$. Using the PDF of the auxiliary random variable r_T, we can derive the distance distribution of $\mathcal{Z}_T$ in Lemma 4 as

$$
\begin{aligned}
f_{\mathcal{Z}_T}(z) &= \frac{\mathrm{d}(\sqrt{z^2 - h^2})}{\mathrm{dz}} f_{r_T}\left(\sqrt{z^2 - h^2}\right) \\
&= \begin{cases} \frac{2z}{R_1^2 - R_2^2}, & \sqrt{R_2^2 + h^2} \leqslant z \leqslant \sqrt{(R_1 - d)^2 + h^2} \\ \frac{2z}{\pi(R_1^2 - R_2^2)} \operatorname{arcsec}\left(\frac{2d\sqrt{z^2 - h^2}}{d^2 + z^2 - h^2 - R_1^2}\right), & \sqrt{(R_1 - d)^2 + h^2} < z \leqslant \sqrt{(R_1 + d)^2 + h^2} \end{cases}.
\end{aligned} \tag{A.5}
$$

A.5 Proof of Theorem 2

The uplink coverage probability of the ABS is given by

$$\begin{aligned}
\mathbb{P}_{\text{cov}}^{u,\text{A}} &= \Pr(\text{SINR}_{\text{A}}^{u} > \gamma_{\text{A}}^{u}) \\
&= \Pr\left(G_A^u > \frac{\gamma_{\text{A}}^{u}}{P_{\text{AsD}} PL_a(\mathcal{Z}_A)}\left(P_{\text{TsUE}} G_T^u PL_a(\mathcal{Z}_T) + \sigma^2\right)\right) \\
&= \mathbb{E}_z\left[\sum_{n=0}^{m_{\text{L}}-1}\frac{(-s_1)^n}{n!}\exp(-s_1\sigma^2)\sum_{k=0}^{n}\binom{n}{k}\frac{p_{\text{L}}}{(-\sigma^2)^{k-n}}\frac{\mathrm{d}^k}{\mathrm{d}s_1^k}\mathcal{L}_{I_{\text{A}}^u}(s_1)\right. \\
&\left.+\sum_{n=0}^{m_{\text{N}}-1}\frac{(-s_2)^n}{n!}\exp(-s_2\sigma^2)\sum_{k=0}^{n}\binom{n}{k}\frac{p_{\text{N}}}{(-\sigma^2)^{k-n}}\frac{\mathrm{d}^k}{\mathrm{d}s_2^k}\mathcal{L}_{I_{\text{A}}^u}(s_2)\right] \qquad \text{(A.6a)} \\
&= \mathbb{E}_z\left[\mathbb{P}_{\text{cov}}^{u,\text{L}}(P_{\text{AsD}}|z) + \mathbb{P}_{\text{cov}}^{u,\text{N}}(P_{\text{AsD}}|z)\right], \qquad \text{(A.6b)}
\end{aligned}$$

where (A.6a) comes from the fact that G_A^u follows Gamma distribution with parameter m_{L} and m_{N} for LOS and NLOS aerial link respectively. $I_{\text{A}}^u = P_{\text{TsUE}} G_T^u PL_a(\mathcal{Z}_T)$, $s_1 = \frac{m_{\text{L}}\gamma_{\text{A}}^u z^{\alpha_{\text{L}}}}{P_{\text{AsD}}\eta_{\text{L}}}$ and $s_2 = \frac{m_{\text{N}}\gamma_{\text{A}}^u z^{\alpha_{\text{N}}}}{P_{\text{AsD}}\eta_{\text{N}}}$. Conditioned on the value of h, there are six possible cases for (A.6b). Taking $\sqrt{\left(\frac{P_{\text{AsD}}^{\max}\eta_{\text{L}}}{\rho_{\text{A}}}\right)^{\frac{2}{\alpha_{\text{L}}}} - R_2^2} < h < \left(\frac{P_{\text{AsD}}^{\max}\eta_{\text{N}}}{\rho_{\text{A}}}\right)^{\frac{1}{\alpha_{\text{N}}}}$ as an example, the uplink coverage probability of the ABS equals to

$$\begin{aligned}
\mathbb{P}_{\text{cov}}^{u,\text{A}} = &\int_h^{\left(\frac{P_{\text{AsD}}^{\max}\eta_{\text{L}}}{\rho_{\text{A}}}\right)^{\frac{1}{\alpha_{\text{L}}}}} \mathbb{P}_{\text{cov}}^{u,\text{L}}\left(\frac{\rho_{\text{A}}}{\eta_{\text{L}}} z^{\alpha_{\text{L}}}|z\right) f_{\mathcal{Z}_A}(z)\mathrm{d}z + \int_{\left(\frac{P_{\text{AsD}}^{\max}}{\rho_{\text{A}}}\right)^{\frac{1}{\alpha_{\text{L}}}}}^{\sqrt{h^2+R_2^2}} \mathbb{P}_{\text{cov}}^{u,\text{L}}(P_{\text{AsD}}^{\max}|z) f_{\mathcal{Z}_A}(z)\mathrm{d}z \\
&+ \int_h^{\left(\frac{P_{\text{AsD}}^{\max}\eta_{\text{N}}}{\rho_{\text{A}}}\right)^{\frac{1}{\alpha_{\text{N}}}}} \mathbb{P}_{\text{cov}}^{u,\text{N}}\left(\frac{\rho_{\text{A}}}{\eta_{\text{N}}} z^{\alpha_{\text{N}}}|z\right) f_{\mathcal{Z}_A}(z)\mathrm{d}z + \int_{\left(\frac{P_{\text{AsD}}^{\max}}{\rho_{\text{A}}}\right)^{\frac{1}{\alpha_{\text{N}}}}}^{\sqrt{h^2+R_2^2}} \mathbb{P}_{\text{cov}}^{u,\text{N}}(P_{\text{AsD}}^{\max}|z) f_{\mathcal{Z}_A}(z)\mathrm{d}z. \qquad \text{(A.7)}
\end{aligned}$$

Appendix B

This appendix contains the proofs needed in Chapter 3.

B.1 Proof of Theorem 7

Following the definition of the Laplace transform, the Laplace transform of the aggregate received signal power distribution at the D2D user X_i is expressed as

$$\begin{aligned}\mathcal{L}_{P_i^n}(s) &= \mathbb{E}_P[\exp(-sP_i^n)] \\ &= \mathbb{E}_{\phi_{\text{active}}}\left[\exp\left(-s\sum_{X_j\in\phi_{\text{active}}} H_j\ell_j^{-\alpha_{\text{T}}}\right)\right] \\ &= \mathbb{E}_{\phi_{\text{active}}}\left[\prod_{X_j\in\phi_{\text{active}}} \exp\left(-sH_j\ell_j^{-\alpha_{\text{T}}}\right)\right]. \end{aligned} \tag{B.1}$$

Conditioned on the location of the D2D user X_i, there are two possible cases for $\mathcal{L}_{P_i^n}(s)$. When $X_i \leqslant R_C - R_D$, the Laplace transform of the aggregate received signal power distribution at the D2D user equals to

$$\mathcal{L}_{P_i^n}(s) = \exp\left(-\int_{-\pi}^{\pi}\int_0^{R_D} \mathbb{E}_H[1-\exp(-sH\ell^{-\alpha_{\text{T}}})]\lambda_i^n \ell \mathrm{d}\ell\mathrm{d}\theta\right) \tag{B.2a}$$

$$= \exp\left(-\pi\lambda_i^n R_D^2 \mathbb{E}_H\left[1-\exp\left(-\frac{sH}{R_D^{\alpha_{\text{T}}}}\right)\right] - \pi\lambda_i^n \mathbb{E}_H\left[\Gamma\left(1-\frac{2}{\alpha_{\text{T}}}, \frac{sH}{R_D^{\alpha_{\text{T}}}}\right)\right]\right) \tag{B.2b}$$

$$= \exp\left(-\pi\lambda_i^n R_D^2\left(1-\frac{2R_D^{\alpha_{\text{T}}}}{s(\alpha_{\text{T}}+2)}\,{}_2F_1\left(1,1+\frac{2}{\alpha_{\text{T}}};2+\frac{2}{\alpha_{\text{T}}};-\frac{R_D^{\alpha_{\text{T}}}}{s}\right)\right)\right), \tag{B.2c}$$

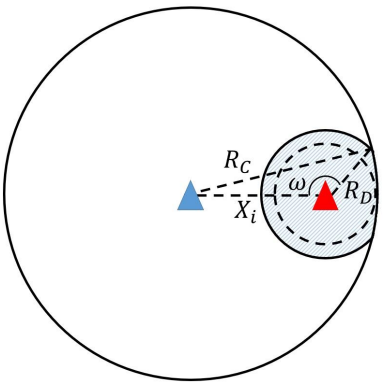

Figure B.1: Illustration of the bounded sensitivity region (shaded blue) of a D2D user (red triangle) located more than $R_C - R_D$ m away from the ground projection of the drone (blue triangle).

where (B.2a) follows the probability generating functional of PPP and $\Gamma(\cdot)$ in (B.2b) denotes the complete Gamma function. Using the fact that H follows an exponential distribution, (B.2c) can be worked out by taking the expectation over H. ${}_2F_1(\cdot,\cdot;\cdot;\cdot)$ is the Gaussian (or ordinary) hypergeometric function.

When $R_C - R_D < X_i \leqslant R_C$, the Laplace transform of the aggregate received signal power distribution at the D2D user is given as

$$\mathcal{L}_{P_i^n}(s) = \underbrace{\exp\left(-\int_0^{R_C-X_i}\int_{-\pi}^{\pi} \mathbb{E}_H[1-\exp(-sH\ell^{-\alpha_T})]\lambda_i^n \ell \mathrm{d}\theta \mathrm{d}\ell\right)}_{A_1}$$
$$\times \underbrace{\exp\left(-\int_{R_C-X_i}^{R_D}\int_{-\omega}^{\omega} \mathbb{E}_H[1-\exp(-sH\ell^{-\alpha_T})]\lambda_i^n \ell \mathrm{d}\theta \mathrm{d}\ell\right)}_{A_2}, \tag{B.3}$$

where the first term A_1 corresponds to the D2D active TXs falling at the ring with radius from 0 to $R_C - X_i$ and the second term A_2 corresponds to the D2D active TXs falling at the arc with angle 2ω and radius from $R_C - X_i$ to R_D as shown in Figure B.1. Using cosine rule, $\omega = \text{arcsec}\left(\frac{2\ell X_i}{\ell^2+X_i^2-R_C^2}\right)$. A_1 can be evaluated follow similar step as in (B.2c).

The second term A_2 is evaluated as

$$\begin{aligned} A_2 &= \exp\left(-\int_{R_C-X_i}^{R_D} 2\mathbb{E}_H[1-\exp(-sH\ell^{-\alpha_T})]\lambda_i^n \ell\omega \mathrm{d}\ell\right) \\ &= \exp\left(-\int_{R_C-X_i}^{R_D} \frac{2s\lambda_i^n \ell\omega}{\ell^{\alpha_T}+s}\mathrm{d}\ell\right), \end{aligned} \tag{B.4}$$

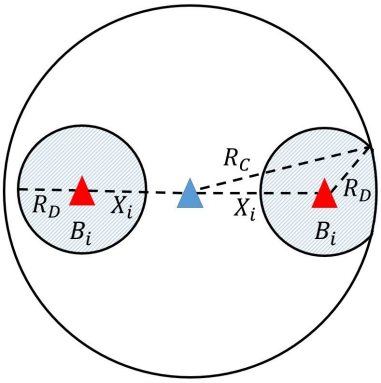

Figure B.2: Illustration of the bounded sensitivity regions of D2D user X_i.

where (B.4) comes from the fact that H follows exponential distribution with unit mean.

Combining (B.2c), (B.3) and (B.4), we can arrive at Theorem 7.

B.2 Proof of Lemma 8

Following the simplification assumption we made in Remark 3, the approximated link success probability for D2D user X_i at T_n for $n = 1, 2, 3...$ is expressed as

$$\widetilde{\mathbb{P}_s^n}(X_i) = 1 - \Pr(N(B_i) = 0) = 1 - \exp(-\lambda_i^n |B_i|), \tag{B.5}$$

where B_i is the bounded sensitivity region of D2D user X_i and $N(B_i)$ is a random counting measure that counts the number of points falling in B_i. For a homogeneous PPP, $N(B_i)$ has a special case as shown above. $|\cdot|$ is the Lebesgue measure, which is the area in a two-dimensional case.

Therefore, the key is to compute the area of the bounded sensitivity region of D2D user X_i, $|B_i|$. From Figure B.2, we can see that there are two different cases based on the location of the D2D user X_i. When $X_i \leqslant R_C - R_D$, the bounded sensitivity region B_i forms a circle with radius R_D. Hence, its area equals to

$$|B_i| = \pi R_D^2. \tag{B.6}$$

When $R_C - R_D < X_i \leqslant R_C$, the bounded sensitivity region B_i becomes an irregular ellipse. Using trigonometry, we can find that the area of B_i can be evaluated as

$$|B_i| = -R_D^2 \left(\arccos\left(\frac{R_C^2 - X_i^2 - R_D^2}{2X_i R_D} \right) - \pi \right) + R_C^2 \arccos\left(\frac{R_C^2 + X_i^2 - R_D^2}{2X_i R_C} \right) - \frac{1}{2}\sqrt{-R_C^4 - R_D^4 - X_i^4 + 2R_C^2 X_i^2 + 2R_D^2 X_i^2 + 2R_C^2 R_D^2}. \tag{B.7}$$

Substituting (B.6) and (B.7) into (B.5), we can arrive at Lemma 8.

Appendix C

This appendix contains the proofs needed in Chapter 4.

C.1 Proof of Proposition 4

Following the definition of MGF,

$$
\begin{aligned}
\mathcal{M}_{P_{\text{agg}}}(s) &= \mathbb{E}\left[\exp(-sP_{\text{agg}})\right] \\
&= \mathbb{E}[\exp(-sP\sum_{X_i\in\phi} G_i h_i PL(r_i))] \\
&= \mathbb{E}[\exp(-sP\sum_{0\leqslant r_i<1} G_i h_i PL(r_i))] \\
&\times \mathbb{E}[\exp(-sP\sum_{1\leqslant r_i<R_{\min}} G_i h_i PL(r_i))] \\
&\times \mathbb{E}[\exp(-sP\sum_{R_{\min}\leqslant r_i<R_{\max}} G_i h_i PL(r_i))] \\
&= \underbrace{\exp\left(-\int_{-\pi}^{\pi}\int_{0}^{1}\mathbb{E}_{h_i,G_i}[1-\exp(-sPG_ih_i)]\lambda r\mathrm{d}r\mathrm{d}\theta\right)}_{A_1} \\
&\times \underbrace{\exp\left(-\int_{-\pi}^{\pi}\int_{1}^{R_{\min}}\mathbb{E}_{h_i,G_i}[1-\exp(-sPG_ih_ir^{-\alpha_{\text{L}}})]\lambda r\mathrm{d}r\mathrm{d}\theta\right)}_{A_2} \\
&\times \underbrace{\exp\left(-\int_{-\pi}^{\pi}\int_{R_{\min}}^{R_{\max}}\mathbb{E}_{h_i,G_i}[1-\exp(-sPG_ih_i\beta r^{-\alpha_{\text{N}}})]\lambda r\mathrm{d}r\mathrm{d}\theta\right)}_{A_3},
\end{aligned}
\tag{C.1}
$$

where $\mathbb{E}_{h_i,G_i}$ represents the expectation with respect to h_i and G_i.

The first term A_1 is evaluated as follows:

$$\begin{aligned} A_1 &= \exp\left(-\pi\lambda\left(1-\mathbb{E}_{h_i,G_i}\left[\exp(-sPG_ih_i)\right]\right)\right) \\ &= \exp\left(-\pi\lambda\left(1-\mathbb{E}_{G_i}\left[\int_0^{\infty}\exp(-sPG_ih)f_{h_{\mathrm{L}}}(h)\mathrm{d}h\right]\right)\right) \\ &= \exp\left(-\pi\lambda+\pi\lambda m^m\mathbb{E}_{G_i}\left[(m+sPG_i)^{-m}\right]\right) \\ &= \exp\left(-\pi\lambda+\pi\lambda m^m\sum_{k=1}^{4}(m+sPG_k)^{-m}p_k\right), \end{aligned} \tag{C.2}$$

where we use the fact that the link in LOS state experiences Nakagami-m fading with $f_{h_{\mathrm{L}}}(h)=\frac{m^m h^{m-1}\exp(-mh)}{\Gamma(m)}$.

The second term A_2 is evaluated as follows:

$$\begin{aligned} A_2 &= \exp\Big(\pi\lambda\mathbb{E}_{h_i,G_i}\left[1-\exp(-sPG_ih_i)\right]-\pi\lambda R_{\min}^2\mathbb{E}_{h_i,G_i}\left[1-\exp(-sR_{\min}^{-\alpha_{\mathrm{L}}}PG_ih_i)\right] \\ &-\pi\lambda\mathbb{E}_{h_i,G_i}\Big[(sPG_ih_i)^{\delta_{\mathrm{L}}}\gamma(1-\delta_{\mathrm{L}},sPh_iG_i)\Big]+\pi\lambda\mathbb{E}_{h_i,G_i}\left[(sPG_ih_i)^{\delta_{\mathrm{L}}}\gamma\left(1-\delta_{\mathrm{L}},\frac{sPh_iG_i}{R_{\min}^{\alpha_{\mathrm{L}}}}\right)\right]\Big) \quad \text{(C.3a)} \\ &= \exp\Bigg(\pi\lambda-\pi\lambda p_k m^m\sum_{k=1}^{4}(m+sPG_k)^{-m}-\pi\lambda R_{\min}^2+\sum_{k=1}^{4}\pi\lambda R_{\min}^2p_km^m(m+sR_{\min}^{-\alpha_{\mathrm{L}}}PG_k)^{-m} \\ &+\pi\lambda\sum_{k=1}^{4}(sPG_k)^{\delta_{\mathrm{L}}}\frac{m^{m+1}(sPG_k)^{-\delta_{\mathrm{L}}-m}\alpha_{\mathrm{L}}}{(2+m\alpha_{\mathrm{L}})}\,{}_2F_1\left(1+m,m+\delta_{\mathrm{L}};1+m+\delta_{\mathrm{L}};-\frac{m}{sPG_k}\right)p_k \\ &-\pi\lambda\sum_{k=1}^{4}\frac{(sPG_k)^{\delta_{\mathrm{L}}}m^{m+1}\alpha_{\mathrm{L}}p_k}{(R_{\min}^{-\alpha_{\mathrm{L}}}sPG_k)^{\delta_{\mathrm{L}}+m}(2+m\alpha_{\mathrm{L}})}\,{}_2F_1\left(1+m,m+\delta_{\mathrm{L}};1+m+\delta_{\mathrm{L}};-\frac{R_{\min}^{\alpha_{\mathrm{L}}}m}{sPG_k}\right)\Bigg), \quad \text{(C.3b)} \end{aligned}$$

where (C.3a) follows from changing variables and integration by parts and (C.3b) is obtained after taking the expectation over h_{L} then G_i.

Similarly, the third term A_3 can be worked out by taking the expectation over h_{N}, which has a PDF as $f_{h_{\mathrm{N}}}(h)=\exp(-h)$. The details are omitted for sake of brevity. Finally, the MGF expression in Proposition 4 is obtained by substituting $A1$, $A2$ and $A3$ into (C.1).

C.2 Proof of Proposition 5

We cannot obtain the nth cumulant of P_{agg} by directly substituting (4.6) into (4.10), as the cumulant becomes incomputable at $s = 0$. Instead, we use the integration form of the MGF in (C.1) and substitute in (4.10) to obtain

$$\begin{aligned}\kappa_{P_{\text{agg}}}(n) = (-1)^{n+1}\Bigg(&\underbrace{\frac{d^n}{ds^n}\int_{-\pi}^{\pi}\int_{0}^{1}\mathbb{E}_{h_i,G_i}[1-\exp(-sPG_ih_i)]\lambda r\mathrm{d}r\mathrm{d}\theta\Big|_{s=0}}_{B_1}\\ &+\underbrace{\frac{d^n}{ds^n}\int_{-\pi}^{\pi}\int_{1}^{R_{\min}}\mathbb{E}_{h_i,G_i}[1-\exp(-sPG_ih_ir^{-\alpha_{\text{L}}})]\lambda r\mathrm{d}r\mathrm{d}\theta\Big|_{s=0}}_{B_2}\\ &+\underbrace{\frac{d^n}{ds^n}\int_{-\pi}^{\pi}\int_{R_{\min}}^{R_{\max}}\mathbb{E}_{h_i,G_i}[1-\exp(-sPG_ih_i\beta r^{-\alpha_{\text{N}}})]\lambda r\mathrm{d}r\mathrm{d}\theta\Big|_{s=0}}_{B_3}\Bigg),\end{aligned} \tag{C.4}$$

where the first term B_1 is evaluated as follows:

$$\begin{aligned}B_1 &= \int_{-\pi}^{\pi}\int_{0}^{1}\mathbb{E}_{h_i,G_i}\left[\frac{d^n 1-\exp(-sPG_ih_i)}{ds^n}\Big|_{s=0}\right]\lambda r\mathrm{d}r\mathrm{d}\theta\\ &= \int_{-\pi}^{\pi}\int_{0}^{1}\mathbb{E}_{h_i,G_i}\left[(-1)^{n+1}(PG_ih_i)^n\right]\lambda r\mathrm{d}r\mathrm{d}\theta\\ &= (-1)^{n+1}P^n\pi\lambda\mathbb{E}_{h_i}\left[h_i^n\right]\mathbb{E}_{G_i}\left[G_i^n\right]\\ &= (-1)^{n+1}P^n\pi\lambda m^{-n}m_{(n)}\sum_{k=1}^{4}G_k^n p_k.\end{aligned} \tag{C.5}$$

Similarly, the terms B_2 and B_3 can be derived by following similar steps as above. Substituting B_1, B_2 and B_3 into (C.4) gives the nth cumulant expression in Proposition 5.

Appendix D

This appendix contains the proof needed in Chapter 5.

D.1 Proof of Proposition 6

By substituting (5.15) into (5.16), we can express the conditional channel coverage probability as

$$\begin{aligned}
\mathbb{P}^{C}_{\text{cov}}(\gamma_{\text{TR}}) &= \Pr\left(\frac{P_{X_0} D_0 h_0 PL(d_0)}{\sum_{X_i \in \phi_{\text{active}}} P_{X_i} D_{i0} h_{i0} PL(X_i) + \sigma^2} > \gamma_{\text{TR}}\right) \\
&\approx \Pr\left(\frac{P_{X_0} D_0 h_0 PL(d_0)}{\sum_{n=0}^{N} \sum_{X_i \in \phi_t^n} P_t^n D_{i0} h_{i0} PL(X_i) + \sigma^2} > \gamma_{\text{TR}}\right) \qquad \text{(D.1a)} \\
&= \Pr\left(h_0 > \frac{\gamma_{\text{TR}}(I_X + \sigma^2)}{P_{X_0} D_0 PL(d_0)}\right) \\
&= \mathbb{E}_{P_{X_0}, I_X}\left[1 - F_{h_0}\left(\frac{\gamma_{\text{TR}}(I_X + \sigma^2)}{P_{X_0} D_0 PL(d_0)}\right)\right], \qquad \text{(D.1b)}
\end{aligned}$$

where approximation in (D.1a) comes from our power level discretization, $I_X = \sum_{n=0}^{N} \sum_{X_i \in \phi_t^n} P_t^n D_{i0} h_{i0} PL(X_i)$ and $F_{h_0}(\cdot)$ is the CDF of the fading power gain on the reference TX-RX link. Since the desired link is assumed to experience Nakagami-m fading with integer m, the CDF of h_0 has a nice form, which is $F_{h_0}(h) = 1 - \sum_{l=0}^{m-1} \frac{1}{l!}(mh)^l \exp(-mh)$.

Hence, we can re-write (D.1b) as

$$\mathbb{P}^{C}_{\text{cov}}(\gamma_{\text{TR}}) = \mathbb{E}_{P_{\text{X0}},I_X}\left[\sum_{l=0}^{m-1}\frac{1}{l!}\left(m\frac{\gamma_{\text{TR}}(I_X+\sigma^2)}{P_{\text{X}_0}D_0PL(d_0)}\right)^l \exp\left(-m\frac{\gamma_{\text{TR}}(I_X+\sigma^2)}{P_{\text{X}_0}D_0PL(d_0)}\right)\right]$$
$$=\sum_{n=0}^{N}\sum_{l=0}^{m-1}\frac{1}{l!}\mathbb{E}_{I_X}\left[\left(m\frac{\gamma_{\text{TR}}(I_X+\sigma^2)}{P_t^n D_0 PL(d_0)}\right)^l \exp\left(-m\frac{\gamma_{\text{TR}}(I_X+\sigma^2)}{P_t^n D_0 PL(d_0)}\right)\right]\frac{k_n}{\mathbb{P}^{P}_{\text{cov}}(\gamma_{\text{PT}})}, \quad \text{(D.2)}$$

where the PMF of P_{X_0} is $\Pr(P_{\text{X}_0} = P_t^n) = \frac{k_n}{\mathbb{P}^{P}_{\text{cov}}(\gamma_{\text{PT}})}$ in (D.2), as we assume that the desired TX is active.

The general form of the Laplace transform of $I_X + \sigma^2$ is

$$\mathcal{L}_{I_X+\sigma^2}(s) = \mathbb{E}_{I_X}[\exp(-s(I_X+\sigma^2))].$$

Taking lth derivative with respect to s, we achieve

$$\frac{dl}{ds^l}\mathcal{L}_{I_X+\sigma^2}(s) = \mathbb{E}_{I_X}\left[\frac{dl}{ds^l}\exp(-s(I_X+\sigma^2))\right]$$
$$=\mathbb{E}_{I_X}\left[(-I_X-\sigma^2)^l \exp(-s(I_X+\sigma^2))\right]. \quad \text{(D.3)}$$

Comparing (D.3) with the expectation term in (D.2), we have

$$\mathbb{P}^{C}_{\text{cov}}(\gamma_{\text{TR}}) = \sum_{n=0}^{N}\sum_{l=0}^{m-1}\frac{(-s)^l}{l!}\frac{dl}{ds^l}\mathcal{L}_{I_X+\sigma^2}(s)\frac{k_n}{\mathbb{P}^{P}_{\text{cov}}(\gamma_{\text{PT}})}, \quad \text{(D.4)}$$

where $s = \frac{m\gamma_{\text{TR}}}{P_t^n D_0 l(d_0)}$. Hence, we arrive the result in Proposition 6.

Bibliography

[1] A. Al-Hourani, S. Kandeepan, and S. Lardner, "Optimal LAP altitude for maximum coverage," *IEEE Wireless Commun. Lett.*, vol. 3, no. 6, pp. 569–572, Dec. 2014. (cited on pages xxiii, 8, and 33)

[2] I. Bor-Yaliniz, A. El-Keyi, and H. Yanikomeroglu, "Efficient 3-D placement of an aerial base station in next generation cellular networks," in *Proc. IEEE ICC*, May 2016. (cited on pages xxiii, 33, and 54)

[3] J. Gozalvez, "5G tests and demonstrations," *IEEE Trans. Veh. Commun.*, vol. 10, no. 2, pp. 16–25, Jun. 2015. (cited on page 1)

[4] K. David and H. Berndt, "6G vision and requirements: Is there any need for beyond 5G?" *IEEE Veh. Technol. Mag.*, vol. 13, no. 3, pp. 72–80, Sep. 2018. (cited on pages 1 and 2)

[5] M. Pätzold, "The final sprint of fifth-generation toward commercialization [mobile radio]," *IEEE Veh. Technol. Mag.*, vol. 13, no. 3, pp. 4–21, Sep. 2018. (cited on pages 1 and 2)

[6] M. Shafi, A. F. Molisch, P. J. Smith, T. Haustein, P. Zhu, P. D. Silva, F. Tufvesson, A. Benjebbour, and G. Wunder, "5G: A tutorial overview of standards, trials, challenges, deployment, and practice," *IEEE J. Sel. Areas Commun.*, vol. 35, no. 6, pp. 1201–1221, Jun. 2017. (cited on pages 1 and 2)

[7] "IEEE 5G and beyond technology roadmap," White Paper, IEEE 5G Initiative, Oct. 2017. [Online]. Available: https://futurenetworks.ieee.org/images/files/pdf/ieee-5g-roadmap-white-paper.pdf (cited on page 2)

[8] Y. Zeng, R. Zhang, and T. J. Lim, "Wireless communications with unmanned aerial vehicles: Opportunities and challenges," *IEEE Commun. Mag.*, vol. 54, no. 5, pp. 36–42, May 2016. (cited on pages 2 and 9)

[9] I. Bor-Yaliniz and H. Yanikomeroglu, "The new frontier in RAN heterogeneity: Multi-tier drone-cells," *IEEE Commun. Mag.*, vol. 54, no. 11, pp. 48–55, Nov. 2016. (cited on page 2)

[10] M. Mozaffari, W. Saad, M. Bennis, Y. N. Nam, and M. Debbah, "A tutorial on UAVs for wireless networks: Applications, challenges and open problems," to appear in *IEEE Commun. Surveys Tuts.*, Aug. 2019. (cited on page 2)

[11] Y. Zeng, Q. Wu, and R. Zhang, "Accessing from the sky: A tutorial on UAV communications for 5G and beyond," submitted to *Proc. IEEE*, Mar. 2019. [Online]. Available: https://arxiv.org/abs/1903.05289 (cited on pages 3 and 8)

[12] D. Marshall, S. Durrani, J. Guo, and N. Yang, "Performance comparison of device-to-device mode selection schemes," in *Proc. IEEE PIMRC*, Aug. 2015. (cited on page 5)

[13] X. Lu, P. Wang, D. Niyato, D. I. Kim, and Z. Han, "Wireless networks with RF energy harvesting: A contemporary survey," *IEEE Commun. Surveys Tuts.*, vol. 17, no. 2, pp. 757–789, Second-quarter 2015. (cited on pages 5, 6, 7, 11, 71, 74, and 91)

[14] A. A. Nasir, X. Zhou, S. Durrani, and R. A. Kennedy, "Relaying protocols for wireless energy harvesting and information processing," *IEEE Trans. Wireless Commun.*, vol. 12, no. 7, pp. 3622–3636, Jul. 2013. (cited on pages 6 and 10)

[15] S. Bi, C. K. Ho, and R. Zhang, "Wireless powered communication: Opportunities and challenges," *IEEE Commun. Mag.*, vol. 53, no. 4, pp. 117–125, Apr. 2015. (cited on page 6)

[16] R. Zhang and C. K. Ho, "MIMO broadcasting for simultaneous wireless information and power transfer," *IEEE Trans. Wireless Commun.*, vol. 12, no. 5, pp. 1989–2001, May 2013. (cited on page 6)

[17] X. Zhou, J. Guo, S. Durrani, and I. Krikidis, "Performance of maximum ratio transmission in ad hoc networks with SWIPT," *IEEE Wireless Commun. Lett.*, vol. 4, no. 5, pp. 529–532, Oct. 2015. (cited on page 6)

[18] (2017, Mar.) CES 2017 Innovation Awards. [Online]. Available: http://www.ces.tech/Events-Experiences/Innovation-Awards-Program/Honorees.aspx (cited on page 6)

[19] W. Khawaja, I. Guvenc, D. W. Matolak, U. C. Fiebig, and N. Schneckenberger, "A survey of air-to-ground propagation channel modeling for unmanned aerial vehicles," to appear in *IEEE Commun. Surveys Tuts.*, Aug. 2019. (cited on pages 8 and 21)

[20] R. Amorim, H. Nguyen, P. Mogensen, I. Z. Kovács, J. Wigard, and T. B. Sørensen, "Radio channel modeling for UAV communication over cellular networks," *IEEE Wireless Commun. Lett.*, vol. 6, no. 4, pp. 514–517, Aug. 2017. (cited on page 8)

[21] R. Amorim, P. Mogensen, T. Sorensen, I. Z. Kovacs, and J. Wigard, "Pathloss measurements and modeling for UAVs connected to cellular networks," in *Proc. IEEE VTC Spring*, Jun. 2017. (cited on page 8)

[22] A. Al-Hourani, S. Kandeepan, and A. Jamalipour, "Modeling air-to-ground path loss for low altitude platforms in urban environments," in *Proc. IEEE Globecom*, Dec. 2014. (cited on pages 8, 21, 33, 44, and 54)

[23] A. Fotouhi, M. Ding, and M. Hassan, "DroneCells: Improving 5G spectral efficiency using drone-mounted flying base stations," submitted to *IEEE Trans. Mobile Comput.*, Jul. 2017. [Online]. Available: https://arxiv.org/abs/1707.02041 (cited on pages 8 and 32)

[24] Y. Zeng, R. Zhang, and T. J. Lim, "Throughput maximization for UAV-enabled mobile relaying systems," *IEEE Trans. Commun.*, vol. 64, no. 12, pp. 4983–4996, Dec. 2016. (cited on page 8)

[25] M. Alzenad, A. El-Keyi, F. Lagum, and H. Yanikomeroglu, "3-D placement of an unmanned aerial vehicle base station (UAV-BS) for energy-efficient maximal coverage," *IEEE Wireless Commun. Lett.*, vol. 6, no. 4, pp. 434–437, Aug. 2017. (cited on pages 8 and 21)

[26] H. He, S. Zhang, Y. Zeng, and R. Zhang, "Joint altitude and beamwidth optimization for UAV-enabled multiuser communications," *IEEE Commun. Lett.*, vol. 22, no. 2, pp. 344–347, Feb. 2018. (cited on page 8)

[27] C. Zhang and W. Zhang, "Spectrum sharing for drone networks," *IEEE J. Sel. Areas Commun.*, vol. 35, no. 1, pp. 136–144, Jan. 2017. (cited on page 8)

[28] F. Lagum, I. Bor-Yaliniz, and H. Yanikomeroglu, "Strategic densification with UAV-BSs in cellular networks," *IEEE Wireless Commun. Lett.*, vol. 7, no. 3, pp. 384–387, Jun. 2018. (cited on page 8)

[29] Q. Wu, Y. Zeng, and R. Zhang, "Joint trajectory and communication design for multi-UAV enabled wireless networks," *IEEE Trans. Wireless Commun.*, vol. 17, no. 3, pp. 2109–2121, Mar. 2018. (cited on page 8)

[30] M. M. Azari, F. Rosas, A. Chiumento, A. Ligata, and S. Pollin, "Uplink performance analysis of a drone cell in a random field of ground interferers," in *Proc. IEEE WCNC*, Apr. 2018. (cited on page 8)

[31] M. Mozaffari, W. Saad, M. Bennis, and M. Debbah, "Unmanned aerial vehicle with underlaid device-to-device communications: Performance and tradeoffs," *IEEE Trans. Wireless Commun.*, vol. 15, no. 6, pp. 3949–3963, Jun. 2016. (cited on pages 8, 9, 21, and 44)

[32] V. V. Chetlur and H. S. Dhillon, "Downlink coverage analysis for a finite 3-D wireless network of unmanned aerial vehicles," *IEEE Trans. Commun.*, vol. 65, no. 10, pp. 4543–4558, Oct. 2017. (cited on pages 8 and 9)

[33] M. M. Azari, Y. Murillo, O. Amin, F. Rosas, M.-S. Alouini, and S. Pollin, "Coverage maximization for a poisson field of drone cells," in *Proc. IEEE PIMRC*, Oct. 2017. (cited on pages 8 and 9)

[34] B. Galkin, J. Kibilda, and L. A. DaSilva, "Coverage analysis for low-altitude UAV networks in urban environments," in *Proc. IEEE Globecom*, Dec. 2017. (cited on pages 8, 9, and 32)

[35] M. Alzenad and H. Yanikomeroglu, "Coverage and rate analysis for unmanned aerial vehicle base stations with LoS/NLoS propagation," in *Proc. IEEE Globecom Workshop*, Dec. 2018. (cited on pages 8 and 9)

[36] ABSOLUTE (Aerial Base Stations with Opportunistic Links for Unexpected and Temporary Events). [Online]. Available: https://cordis.europa.eu/project/rcn/106035_en.html (cited on page 9)

[37] N. Morozs, T. Clarke, and D. Grace, "Heuristically accelerated reinforcement learning for dynamic secondary spectrum sharing," *IEEE Access*, vol. 3, pp. 2771–2783, Dec. 2015. (cited on page 9)

[38] S. Koulali, E. Sabir, T. Taleb, and M. Azizi, "A green strategic activity scheduling for UAV networks: A sub-modular game perspective," *IEEE Commun. Mag.*, vol. 54, no. 5, pp. 58–64, May 2016. (cited on page 9)

[39] P. Yang, X. Cao, C. Yin, Z. Xiao, X. Xi, and D. Wu, "Proactive drone-cell deployment: Overload relief for a cellular network under flash crowd traffic," *IEEE Trans. Intell. Transp. Syst.*, vol. 18, no. 10, pp. 2877–2892, May 2017. (cited on pages 9, 20, and 44)

[40] N. Rupasinghe, Y. Yapici, I. Guvenc, and Y. Kakishima, "Non-orthogonal multiple access for mmWave drone networks with limited feedback," *IEEE Trans. Commun.*, vol. 67, no. 1, pp. 762–777, Jan. 2019. (cited on page 9)

[41] V. Sharma, I. You, and R. Kumar, "Energy efficient data dissemination in multi-UAV coordinated wireless sensor networks," *Mobile Inf. Syst.*, vol. 2016, pp. 1–13, May 2016. (cited on page 9)

[42] X. Fan, C. Huang, B. Fu, S. Wen, and X. Chen, "UAV-assisted data dissemination in delay-constrained VANETs," *Mobile Inf. Syst.*, vol. 2018, pp. 1–12, Oct. 2018. (cited on page 9)

[43] F. Zeng, R. Zhang, X. Cheng, and L. Yang, "UAV-assisted data dissemination scheduling in VANETs," in *Proc. IEEE ICC*, May 2018. (cited on page 10)

[44] Y. Xu, X. Li, and J. Zhang, "Device-to-device content delivery in cellular networks: Multicast or unicast," *IEEE Trans. Veh. Technol.*, vol. 67, no. 5, pp. 4401–4414, May 2018. (cited on page 10)

[45] H. Meshgi, D. Zhao, and R. Zheng, "Optimal resource allocation in multicast device-to-device communications underlaying lte networks," *IEEE Trans. Veh. Technol.*, vol. 66, no. 9, pp. 8357–8371, Sep. 2017. (cited on page 10)

[46] X. Lin, R. Ratasuk, A. Ghosh, and J. G. Andrews, "Modeling, analysis and optimization of multicast device-to-device transmissions," *IEEE Trans. Wireless Commun.*, vol. 13, no. 8, pp. 4346–4359, Aug. 2014. (cited on page 10)

[47] T. V. Santana, R. Combes, and M. Kobayashi. (2018) "Device-to-device aided multicasting". [Online]. Available: https://arxiv.org/abs/1801.05224 (cited on page 10)

[48] C. Liu and J. G. Andrews, "Multicast outage probability and transmission capacity of multihop wireless networks," *IEEE Trans. Inf. Theory*, vol. 57, no. 7, pp. 4344–4358, Jul. 2011. (cited on page 10)

[49] H. Tabassum, E. Hossain, A. Ogundipe, and D. I. Kim, "Wireless-powered cellular networks: Key challenges and solution techniques," *IEEE Commun. Mag.*, vol. 53, no. 6, pp. 63–71, Jun. 2015. (cited on page 11)

[50] Y. Zeng, B. Clerckx, and R. Zhang, "Communications and signals design for wireless power transmission," *IEEE Trans. Commun.*, vol. 65, no. 5, pp. 2264–2290, May 2017. (cited on page 11)

[51] Y. Deng, L. Wang, M. Elkashlan, M. D. Renzo, and J. Yuan, "Modeling and analysis of wireless power transfer in heterogeneous cellular networks," *IEEE Trans. Commun.*, vol. 64, no. 12, pp. 5290–5303, Dec. 2016. (cited on page 11)

[52] S. Akbar, Y. Deng, A. Nallanathan, M. Elkashlan, and A. H. Aghvami, "Simultaneous wireless information and power transfer in K-tier heterogeneous cellular networks," *IEEE Trans. Wireless Commun.*, vol. 15, no. 8, pp. 5804–5818, Aug. 2016. (cited on pages 11 and 86)

[53] K. Huang and V. K. N. Lau, "Enabling wireless power transfer in cellular networks: Architecture, modeling and deployment," *IEEE Trans. Wireless Commun.*, vol. 13, no. 2, pp. 902–912, Feb. 2014. (cited on pages 11 and 78)

[54] J. Guo, S. Durrani, X. Zhou, and H. Yanikomeroglu, "Outage probability of ad hoc networks with wireless information and power transfer," *IEEE Wireless Commun. Lett.*, vol. 4, no. 4, pp. 409–412, Aug. 2015. (cited on pages 11, 12, 67, and 87)

[55] D. Oliveira and R. Oliveira, "Characterization of energy availability in RF energy harvesting networks," *Math. Probl. Eng.*, vol. 2016, pp. 1–9, 2016. (cited on page 11)

[56] W. Liu, X. Zhou, S. Durrani, H. Mehrpouyan, and S. D. Blostein, "Energy harvesting wireless sensor networks: Delay analysis considering energy costs of sensing and transmission," *IEEE Trans. Wireless Commun.*, vol. 15, no. 7, pp. 4635–4650, Jul. 2016. (cited on page 11)

[57] A. H. Sakr and E. Hossain, "Cognitive and energy harvesting-based D2D communication in cellular networks: Stochastic geometry modeling and analysis," *IEEE Trans. Commun.*, vol. 63, no. 5, pp. 1867–1880, May 2015. (cited on pages 11 and 87)

[58] ——, "Analysis of K-tier uplink cellular networks with ambient RF energy harvesting," *IEEE J. Sel. Areas Commun.*, vol. 33, no. 10, pp. 2226–2238, Oct. 2015. (cited on pages 11 and 86)

[59] T. A. Khan, A. Alkhateeb, and R. W. Heath, "Millimeter wave energy harvesting," *IEEE Trans. Wireless Commun.*, vol. 15, no. 9, pp. 6048–6062, Sep. 2016. (cited on pages 11, 12, and 83)

[60] L. Wang, M. Elkashlan, R. W. Heath, M. D. Renzo, and K. K. Wong, "Millimeter wave power transfer and information transmission," in *Proc. IEEE GLOBECOM*, Dec. 2015. (cited on pages 11, 12, 78, and 86)

[61] Y. Ma, H. Chen, Z. Lin, Y. Li, and B. Vucetic, "Distributed and optimal resource allocation for power beacon-assisted wireless-powered communications," *IEEE Trans. Commun.*, vol. 63, no. 10, pp. 3569–3583, Oct. 2015. (cited on page 11)

[62] C. Zhong, X. Chen, Z. Zhang, and G. K. Karagiannidis, "Wireless-powered communications: Performance analysis and optimization," *IEEE Trans. Commun.*, vol. 63, no. 12, pp. 5178–5190, Dec. 2015. (cited on page 11)

[63] X. Jiang, C. Zhong, Z. Zhang, and G. K. Karagiannidis, "Power beacon assisted wiretap channels with jamming," *IEEE Trans. Wireless Commun.*, vol. 15, no. 12, pp. 8353–8367, Dec. 2016. (cited on page 11)

[64] S. Lee, R. Zhang, and K. Huang, "Opportunistic wireless energy harvesting in cognitive radio networks," *IEEE Trans. Wireless Commun.*, vol. 12, no. 9, pp. 4788–4799, Sep. 2013. (cited on page 11)

[65] Z. Wang, L. Duan, and R. Zhang, "Adaptively directional wireless power transfer for large-scale sensor networks," *IEEE J. Sel. Areas Commun.*, vol. 34, no. 5, pp. 1785–1800, May 2016. (cited on page 12)

[66] Y. Liu, L. Wang, S. A. R. Zaidi, M. Elkashlan, and T. Q. Duong, "Secure D2D communication in large-scale cognitive cellular networks: A wireless power

transfer model," *IEEE Trans. Commun.*, vol. 64, no. 1, pp. 329–342, Jan. 2016. (cited on page 12)

[67] T. S. Rappaport, S. Sun, R. Mayzus, H. Zhao, Y. Azar, K. Wang, G. N. Wong, J. K. Schulz, M. Samimi, and F. Gutierrez, "Millimeter wave mobile communications for 5G cellular: It will work!" *IEEE Access*, vol. 1, pp. 335–349, May 2013. (cited on page 12)

[68] J. G. Andrews, T. Bai, M. N. Kulkarni, A. Alkhateeb, A. K. Gupta, and R. W. Heath, "Modeling and analyzing millimeter wave cellular systems," *IEEE Trans. Commun.*, vol. 65, no. 1, pp. 403–430, Jan. 2017. (cited on pages 12, 64, 66, 71, 79, 80, and 91)

[69] M. D. Renzo, "Stochastic geometry modeling and analysis of multi-tier millimeter wave cellular networks," *IEEE Trans. Wireless Commun.*, vol. 14, no. 9, pp. 5038–5057, Sep. 2015. (cited on pages 12, 64, 66, 79, 80, and 91)

[70] K. Venugopal, M. C. Valenti, and R. W. Heath, "Device-to-device millimeter wave communications: Interference, coverage, rate, and finite topologies," *IEEE Trans. Wireless Commun.*, vol. 15, no. 9, pp. 6175–6188, Sep. 2016. (cited on pages 12, 66, 81, and 97)

[71] D. Maamari, N. Devroye, and D. Tuninetti, "Coverage in mmWave cellular networks with base station co-operation," *IEEE Trans. Wireless Commun.*, vol. 15, no. 4, pp. 2981–2994, Apr. 2016. (cited on page 12)

[72] X. Zhou, S. Durrani, J. Guo, and H. Yanikomeroglu, "Underlay drone cell for temporary events: Impact of drone height and aerial channel environments," *IEEE Internet Things J.*, vol. 6, no. 2, pp. 1704–1718, Apr. 2019. (cited on page 14)

[73] X. Zhou, S. Durrani, and J. Guo, "Drone-initiated D2D-aided multihop multicast networks for emergency information dissemination," submitted to *IEEE Access,* under major revision. (cited on page 15)

[74] ——, "Characterization of aggregate received power from power beacons in millimeter wave ad hoc networks," in *Proc. IEEE ICC*, May 2017. (cited on pages 15 and 87)

[75] X. Zhou, J. Guo, S. Durrani, and M. D. Renzo, "Power beacon-assisted millimeter wave ad hoc networks," *IEEE Trans. Commun.*, vol. 66, no. 2, pp. 830–844, Feb. 2018. (cited on page 17)

[76] J. Lyu, Y. Zeng, and R. Zhang, "UAV-aided offloading for cellular hotspot," *IEEE Trans. Wireless Commun.*, vol. 17, no. 6, pp. 3988–4001, Jun. 2018. (cited on pages 20 and 44)

[77] L. Song, Z. Han, and C. Xu, *Resource Management for Device-to-Device Underlay Communication*. New York, NY, USA: Springer, 2014. (cited on page 20)

[78] Z. Zhou, K. Ota, M. Dong, and C. Xu, "Energy-efficient matching for resource allocation in D2D enable cellular networks," *IEEE Trans. Veh. Technol.*, vol. 66, no. 6, pp. 5256–5268, Jun. 2017. (cited on page 20)

[79] T. D. Novlan, H. S. Dhillon, and J. G. Andrews, "Analytical modeling of uplink cellular networks," *IEEE Trans. Wireless Commun.*, vol. 12, no. 6, pp. 2669–2679, Jun. 2013. (cited on page 22)

[80] M. M. Azari, F. Rosas, A. Chiumento, and S. Pollin, "Coexistence of terrestrial and aerial users in cellular networks," in *Proc. IEEE Globecom Workshops*, Dec. 2017. (cited on page 32)

[81] 3GPP, "Study on enhanced LTE support for aerial vehicles," *TR 36.777*, Dec. 2017. (cited on page 34)

[82] S. Seong, I. Sohn, S. Choi, and K. B. Lee, "Distributed synchronization algorithm for infrastructure-less public safety networks," *J. Commun. Netw.*, vol. 20, no. 3, pp. 316–324, Jun. 2018. (cited on page 46)

[83] D. T. Roche, B. Champagne, I. Psaromiligkos, and B. Pelletier, "On the use of distributed synchronization in 5G device-to-device networks," in *Proc. IEEE ICC*, May 2017. (cited on page 46)

[84] W. Sun, M. R. Gholami, E. G. Strom, and F. Brannstrom, "Distributed clock synchronization with application of D2D communication without infrastructure," in *Proc. IEEE Globecom Workshop*, Dec. 2013. (cited on page 46)

[85] Y.-C. Ko, M.-S. Alouini, and M. K. Simon, "Outage probability of diversity systems over generalized fading channels," *IEEE Trans. Commun.*, vol. 48, no. 11, pp. 1783–1787, Nov. 2000. (cited on pages 49 and 83)

[86] J. Guo, S. Durrani, and X. Zhou, "Outage probability in arbitrarily-shaped finite wireless networks," *IEEE Trans. Commun.*, vol. 62, no. 2, pp. 699–712, Feb. 2014. (cited on pages 49, 83, 85, and 88)

[87] M. Mozaffari, W. Saad, M. Bennis, and M. Debbah, "Mobile unmanned aerial vehicles (UAVs) for energy-efficient internet of things communications," *IEEE Trans. Wireless Commun.*, vol. 16, no. 11, pp. 7574–7589, Nov. 2017. (cited on page 54)

[88] M. Xia and S. Aissa, "On the efficiency of far-field wireless power transfer," *IEEE Trans. Signal Process.*, vol. 63, no. 11, pp. 2835–2847, Jun. 2015. (cited on pages 64, 67, 75, 79, and 95)

[89] M. R. Akdeniz, Y. Liu, M. K. Samimi, S. Sun, S. Rangan, T. S. Rappaport, and E. Erkip, "Millimeter wave channel modeling and cellular capacity evaluation," *IEEE J. Sel. Areas Commun.*, vol. 32, no. 6, pp. 1164–1179, Jun. 2014. (cited on pages 65 and 79)

[90] X. Zhang and J. G. Andrews, "Downlink cellular network analysis with multi-slope path loss models," *IEEE Trans. Commun.*, vol. 63, no. 5, pp. 1881–1894, May 2015. (cited on pages 66 and 80)

[91] M. D. Renzo and P. Guan, "Stochastic geometry modeling of coverage and rate of cellular networks using the Gil-Pelaez inversion theorem," *IEEE Commun. Lett.*, vol. 18, no. 9, pp. 1575–1578, Sep. 2014. (cited on pages 67 and 83)

[92] A. Papoulis and S. U. Pillai, *Probability, Random Variables and Stochastic Processes*, 4th ed. McGraw-Hill, 2002. (cited on page 69)

[93] J. Guo, S. Durrani, and X. Zhou, "Characterization of aggregate interference in arbitrarily-shaped underlay cognitive networks," in *Proc. IEEE Globecom*, Dec. 2014. (cited on page 70)

[94] R. K. Ganti and M. Haenggi, "Interference in ad hoc networks with general motion-invariant node distributions," in *Proc. IEEE ISIT*, Jul. 2008. (cited on page 73)

[95] R. W. Heath, M. Kountouris, and T. Bai, "Modeling heterogeneous network interference using poisson point processes," *IEEE Trans. Signal Process.*, vol. 61, no. 16, pp. 4114–4126, Aug. 2013. (cited on page 73)

[96] H. Xia, B. Natarajan, and C. Liu, "Feasibility of simultaneous information and energy transfer in LTE-A small cell networks," in *Proc. IEEE CCNC*, Jan. 2014. (cited on page 74)

[97] A. Biason and M. Zorzi, "Joint transmission and energy transfer policies for energy harvesting devices with finite batteries," *IEEE J. Sel. Areas Commun.*, vol. 33, no. 12, pp. 2626–2640, Dec. 2015. (cited on page 78)

[98] A. Ghazanfari, H. Tabassum, and E. Hossain, "Ambient RF energy harvesting in ultra-dense small cell networks: Performance and trade-offs," *IEEE Wireless Commun.*, vol. 23, no. 2, pp. 38–45, Apr. 2016. (cited on page 78)

[99] E. Boshkovska, D. W. K. Ng, N. Zlatanov, and R. Schober, "Practical non-linear energy harvesting model and resource allocation for SWIPT systems," *IEEE Commun. Lett.*, vol. 19, no. 12, pp. 2082–2085, Dec. 2015. (cited on page 79)

[100] M. D. Renzo, W. Lu, and P. Guan, "The intensity matching approach: A tractable stochastic geometry approximation to system-level analysis of cellular networks," *IEEE Trans. Wireless Commun.*, vol. 15, no. 9, pp. 5963–5983, Sep. 2016. (cited on page 79)

[101] T. Bai and R. W. Heath, "Coverage and rate analysis for millimeter-wave cellular networks," *IEEE Trans. Wireless Commun.*, vol. 14, no. 2, pp. 1100–1114, Feb. 2015. (cited on pages 79 and 83)

[102] M. D. Renzo and W. Lu, "System-level analysis and optimization of cellular networks with simultaneous wireless information and power transfer: Stochastic geometry modeling," *IEEE Trans. Veh. Technol.*, vol. 66, no. 3, pp. 2251–2275, Mar. 2017. (cited on page 79)

[103] S. Al-Ahmadi and H. Yanikomeroglu, "On the approximation of the generalized-K distribution by a gamma distribution for modeling composite fading channels," *IEEE Trans. Wireless Commun.*, vol. 9, no. 2, pp. 706–713, Feb. 2010. (cited on page 80)

[104] G. Lee, Y. Sung, and J. Seo, "Randomly-directional beamforming in millimeter-wave multiuser MISO downlink," *IEEE Trans. Wireless Commun.*, vol. 15, no. 2, pp. 1086–1100, Feb. 2016. (cited on pages 80 and 81)

[105] M. Haenggi, *Stochastic Geometry for Wireless Networks*. Cambridge: Cambridge University Press, 2013. (cited on pages 82 and 83)

[106] A. Thornburg, T. Bai, and R. W. Heath, "Performance analysis of outdoor mmWave ad hoc networks," *IEEE Trans. Signal Process.*, vol. 64, no. 15, pp. 4065–4079, Aug. 2016. (cited on page 83)

[107] I. S. Gradshteyn and I. M. Ryzhik, *Table of Integrals, Series, and Products*, 7th ed. Academic Press, 2007. (cited on page 83)

[108] S. Singh, M. N. Kulkarni, A. Ghosh, and J. G. Andrews, "Tractable model for rate in self-backhauled millimeter wave cellular networks," *IEEE J. Sel. Areas Commun.*, vol. 33, no. 10, pp. 2196–2211, Oct. 2015. (cited on page 91)

[109] (2016, Dec.) Amazon Prime Air. [Online]. Available: https://www.amazon.com/Amazon-Prime-Air/b?ie=UTF8&node=8037720011 (cited on page 103)

[110] A. Fotouhi, H. Qiang, M. Ding, M. Hassan, L. G. Giordano, A. Garcia-Rodriguez, and J. Yuan, "Survey on UAV cellular communications: Practical aspects, standardization advancements, regulation, and security challenges," to appear in *IEEE Commun. Surveys Tuts.*, Aug. 2019. (cited on page 104)

[111] Z. Khalid and S. Durrani, "Distance distributions in regular polygons," *IEEE Trans. Veh. Technol.*, vol. 62, no. 5, pp. 2363–2368, Jun. 2013. (cited on page 107)

[112] R. Pure and S. Durrani, "Computing exact closed-form distance distributions in arbitrarily-shaped polygons with arbitrary reference point," *Mathematica J.*, vol. 17, Jun. 2015. (cited on page 107)